Control of Radon and Pollutants in Gas-based Directional Dark Matter Detectors Using Molecular Sieves

University of Sheffield

Robert Renz Marcelo Gregorio

Department of Physics & Astronomy
University of Sheffield

A thesis submitted in partial fulfilment for the degree of
Doctor of Philosophy

November 2022

I would like to dedicate this thesis to my Mummy, Anne and Carlos ...

Abstract

The most compelling explanation for the so-called Dark Matter of the Universe is the postulation of particles beyond the standard model, with Weakly Interacting Massive Particle (WIMP) dark matter being a well-motivated. While there are many different methods to search for WIMPs, the most sensitive dark matter experiments in the world employ liquid noble gas targets to detect WIMP-induced recoils. As the next generation of liquid noble detectors become more sensitive, they are confronted by an inevitable background of solar neutrinos, which inhibit the conclusive identification of dark matter in such searches. Directional dark matter detectors have the capability to distinguish against the otherwise irreducible solar neutrino background by adding information about the direction of the WIMP-induced recoil events.

Most directional detectors reconstruct recoil tracks using low-pressure gas Time Projection Chambers (TPC). In gas TPC operation, it is important to remove radon and common pollutants from the target gas. Radon contamination provides a source of unwanted background able to mimic WIMP-induced recoils, while common pollutants can significantly suppress the gain of the detector. SF_6 is an ideal target gas for directional dark matter searches, so the ability to remove radon and common pollutants from SF_6 during TPC operation is crucial. A method that also recycles SF_6 is required as it is a potent greenhouse gas.

This thesis describes work toward a gas recycling system that removes radon and common pollutants from target gases during TPC operation. The removal of radon from SF_6 gas was demonstrated for the first time using a 5Å type molecular sieve. A low radioactive 5Å type molecular sieve that intrinsically emanated 98.9% less radon per radon captured compared to commercial sieves was found. To effectively implement the molecular sieves with TPC detectors, a gas system utilising a modified Vacuum Swing Adsorption (VSA) technique with a gas recovery buffer was designed. The VSA technique minimises the required amount of molecular sieve for long-term filtration, and the gas recovery buffer maximises the amount of recycled gas. The design was built into a prototype and tested with a small-scale gas TPC detector. Performance testing with the gas system prototype resulted in the low radioactive 5Å type molecular sieve reducing the intrinsic radon contamination of the TPC detector setup within the background limits of the radon measurement apparatus (14.0±5.7 mBq). A TPC

detector run with the gas system employing 3Å and 4Å type molecular sieves significantly reduced the impact of common pollutants suppressing signal amplification, with the detector signal remaining until detector operation was terminated after 340 hours. Without the gas system, the TPC detector could only maintain this level of signal amplification for 50 hours. The results presented in this thesis successfully demonstrate the feasibility of a molecular sieve-based gas recycling system that simultaneously removes radon and common pollutants from SF_6-based directional dark matter detectors.

Author's Contributions

Chapter 3

The author designed and constructed the experimental setup to determine changes in collection efficiencies in electrostatic detectors due to different carrier gases. Data collection, analysis and interpretation of results were completed by the author. The author wrote the python code to simulate radon collection in the DURRIDGE RAD7 radon detector. The author implemented collection losses due to physical and chemical processes in the simulation code.

Chapter 4 (publication)[1]

Demonstration of radon removal from SF_6 using molecular sieves, (2017) JINST **12** P09025

The author conceptualised the use of molecular sieves to remove radon from SF_6 gas. For both the SF_6 absorption test and radon filtration test, the experimental setup was designed and constructed by the author. The author suggested improving the radon filtration rate by using a cold trap. Data collection, analysis and interpretation of results were completed by the author. Manuscript preparation was done by the author. Co-authors reviewed and commented on the manuscript.

Chapter 5 (publication)[2]

Test of low radioactive molecular sieves for radon filtration in SF_6 gas-based rare-event physics experiments, (2021) JINST **16** P06024

The method for molecular sieve radon filtration and radon emanation comparison was developed by the author. The low-radioactive Nihon-University molecular sieves sample was prepared by H. Ogawa. The radon emanation test was based on work by A. Scarff. The radon filtration test and experimental setup were designed and constructed by the author. The

[1] This chapter has been prepared in line with University of Sheffield guidelines regarding how to include work published by the author in peer-reviewed journals during the PhD. The paper is presented here as published followed by relevant updates to the work as conducted by the author .

[2] See footnote 1.

author suggested improving the radon filtration rate by turning the sieves into a powder. Data collection, analysis and interpretation of results were completed by the author. Manuscript preparation was done by the author. Co-authors reviewed and commented on the manuscript.

Chapter 6

The author conceptualised the use of molecular sieves in a gas system utilising a vacuum swing adsorption technique with a recovery buffer for gas-based experiments. The author designed the molecular sieve gas system and developed a method of operation. The author selected components and constructed a gas system prototype for use with a low-pressure gas-based detector. The author performed and optimised the demonstration of the gas system prototype's operation with a 100L vessel. As part of the group's collaborative efforts with Kobe University, Japan, the author conducted field tests at Kobe which are the subject of future work.

Chapter 7

Application and operation of the gas system prototype with a 100L ThGEM-based TPC were performed by the author. Stable ThGEM-based TPC operational voltage and pressure configuration in CF_4 were based on work by A. Scarff. The author designed and performed the radon reduction test. A suggestion on radon reduction analysis was provided by S.W. Sadler. The gas gain over time test was designed and performed by the author. Gas gain calibration and analysis were based on work by C. Eldridge. The author automated logging. Data collection, analysis and interpretation of results were completed by the author. The author is preparing a journal paper on this work.

Acknowledgements

I would like to acknowledge and give my thanks to my supervisor **Neil Spooner** for his guidance and support throughout my time in Sheffield. I am grateful for **Stephen Sadler** and **DURRIDGE** for providing me with the opportunity to undertake this PhD. Special thanks to my Sheffield undergraduate personal tutor **Julia Weinstein**, without your encouragement, I would not have come so far. I want to acknowledge the large amount of support provided by **CYGNUS group** at Sheffield, Japan and Italy, particularly by Anthony Ezeribe, Andrew Scarff, Warren Lynch, Callum Eldridge, Ali Mclean, Kentaro Miuchi and Hiroshi Ogawa.

I want to thank all my friends throughout my time in Sheffield. Big thanks to **Clint Ramos** and everyone involved in establishing the University of Sheffield **Filipino society**. To the Howard boyz (**Nathan Kaushik**, **James Edes** and **Jake Murray**) and **Richard Lozano**. Special thanks to Nathan for introducing me to boxing which has been paramount to balancing my PhD life. Shout out to **Brendan Warburton**, **Will Simpson** and everybody at the University of Sheffield **Boxing Club**.

I would like to thank **Charmaine Labto**, **Lucy Day**, **Jose San Antonio**, **Fatima Lugtu**, **Jeremae de los Santos**, **Eric Medina** and **Yoorisa Pde** for making my second stint in Sheffield so enjoyable. Special thanks to Charmaine for teaching me how to make amazing graphics/figures.

I would also like to thank my day-ones for their encouragement and for visiting me in Sheffield. **Eugene Njenga**, **Shaquille Harvey**, **Lorraine Bañares**, **Brandon Nichols**, **Richard Lawal**, **Mauro Saquitala** and **Alvin Enriquez**. Special appreciation for **Bernadette Iglesias**, your daily dose of support helped me get through the most difficult period of my PhD.

Finally, a very special thank you to my **family** here and in the Philippines. **Mummy**, without you, I would not have finished my PhD. Thank you for going above and beyond to help me get this far. This one's for you.

Contents

List of Figures

List of Tables

Chapter 1

Dark matter and the search for WIMPs

A general summary of dark matter is given in this chapter. Firstly, in Section 1.1 a historical overview of some of the earliest observations that revealed the existence of dark matter, followed by an overview of possible dark matter particle candidates in accordance with observations is given. The three main methods to experimentally search for dark matter are presented in Section 1.2. As the main focus of this thesis is on radon contamination and common pollutant control in directional dark matter detectors, an extended review and motivation for this type of experimental search is given in Section 1.3, followed by some conclusions in Section 1.4.

1.1 Dark matter

1.1.1 Evidence for dark matter

Motion of galaxies in galaxy clusters

The first significant evidence for the existence of so-called dark matter in the Universe came from a study of the motions of galaxies in the Coma cluster by Fritz Zwicky in 1933 [1]. In this study it was found that the mass required to explain the observed velocities of the galaxies cannot be accounted for by the luminous mass in the cluster. Zwicky deduced the mass of the coma cluster from the motions of the galaxies using the virial theorem [2]. Assuming the Coma system has mechanically reached a stationary state and the matter is distributed in the cluster uniformly, the virial theorem states the mean kinetic energy, $\langle E_{KE} \rangle$, and mean potential energy , $\langle E_{PE} \rangle$ of the cluster is given by

$$\langle E_{KE} \rangle = -\frac{1}{2} \langle E_{PE} \rangle. \tag{1.1}$$

The mean kinetic energy, $\langle E_{KE} \rangle$, is given by

$$\langle E_{KE} \rangle = \frac{1}{2} M \langle v^2 \rangle, \tag{1.2}$$

where the mass of the cluster is M, and the average square velocity of the cluster's galaxies is $\langle v^2 \rangle$. The mean potential energy,$\langle E_{PE} \rangle$, is given by the gravitational potential energy

$$\langle E_{PE} \rangle = -\frac{3}{5} \frac{GM^2}{R}, \tag{1.3}$$

where G is the gravitational constant and R is the radius of the cluster. Using the virial theorem and combining Equation 1.2 and Equation 1.3, the mass of the cluster, M, is given by

$$M = \frac{5R\langle v^2 \rangle}{3G}, \tag{1.4}$$

Zwicky obtained values for the velocities of galaxies using redshift measurements observed from the Coma cluster. From these measurements, the average square velocity of the cluster's galaxies $\langle v^2 \rangle$ was determined, and the mass of the cluster was calculated using Equation 1.4. The mass deduced from this method is

$$M \approx 4.5 \times 10^{13} M\odot \ . \tag{1.5}$$

Assuming that the luminosity of the average nebula is $8.5 \times 10^7 M\odot$, this equates to a mass to light ratio of

$$M/L = 500. \tag{1.6}$$

This was a surprising result as the mass to light ratio for the local Kapteyn stellar system is M/L = 3. Zwicky concluded that the large mass discrepancy was due to dark matter, or "dunkle matter" in the original paper. Although modern values of the Hubble constant show that the value used by Zwicky for his calculation of velocities from redshift measurements was a factor of 8 wrong, modern estimate of the Coma cluster M/L is $\sim$ 160 [3]. M/L has since been measured for many other galaxies giving rise to a general picture of high M/L values [4], pointing towards the existence of missing mass.

Galaxy rotation curves

A galaxy rotational curve is the relationship between objects' velocities as a function of distance from the galactic centre. A study of the Andromeda galaxy's rational curve by Rubin and Ford in 1970 found that the rotational speed flattens out at larger radii as opposed

to the expected decrease from the observed luminous matter [5]. The velocity of objects in the galaxy, such as gas clouds, can be deduced by considering the forces in a gravitationally bound system. Newtonian gravity states that the force between mass m encircling a mass $M(r)$ separated by radius r is given by

$$F = \frac{GmM(r)}{r^2}, \tag{1.7}$$

where G is the gravitational constant. For mass m to remain in rotational motion, the force is balanced by centripetal force given by

$$F = \frac{mv^2}{r}, \tag{1.8}$$

where v is velocity of the mass m and r is the distance from the orbits centre. Combining Equation 1.7 and Equation 1.8, the rotational velocity v is given by

$$v = \sqrt{\frac{GM(r)}{r}}. \tag{1.9}$$

Since Andromeda is a spiral galaxy with most of the luminous mass at the centre, the rotational curve is expected to follow Keplerian dynamics with the rotational velocity dropping off with increasing r given by relation $v \propto r^{-1/2}$. Instead, the rotational curve observed by Rubin and Ford, given in Figure 1.1, showed rotational velocities flattening, approaching a constant value with increasing distance r.

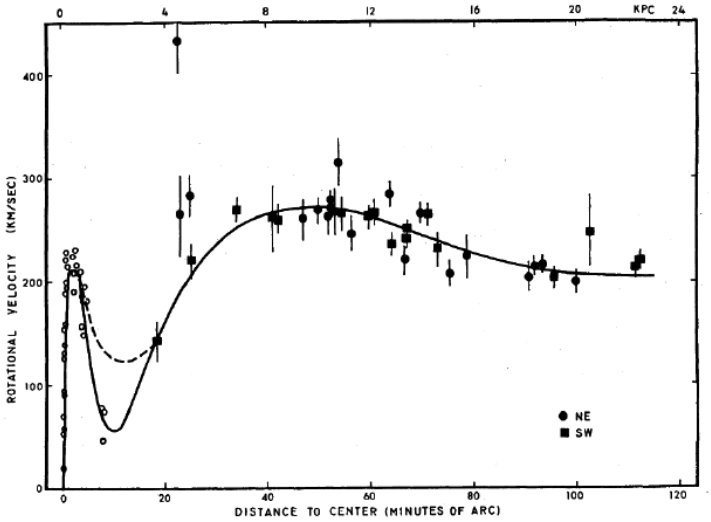

Figure 1.1 Rotational curves of objects in the Andromeda galaxy [5].

These results suggest that $M(r) \propto r$, implying that there is more gravitational mass than visible matter. Moreover, the unknown mass was distributed out to larger distances than the luminous matter, with non-interacting dark matter retaining it's original geometry and shape, and therefore usually modelled assuming that it is spherically symmetric to first order. Many galaxy rotation curves have since been measured with flat rotation curves routinely observed [6–8].

Gravitational lensing

Observation of gravitational lensing at large distances also now reveals copious amounts of dark matter. Gravitational lensing occurs when massive celestial bodies like galaxy clusters cause the curvature of spacetime resulting in the bending of light and acts as a lens. When there is a radiation emitting object beyond a lensing object, with respect to Earth, strong or weak gravitational lensing can occur depending on the alignment and size of the lensing object. Strong lensing can cause distortions observed as arcs and rings [9], whereas weak lensing causes smaller distortions such as magnification and shear [10]. The lensing effect can be used to determine the mass of the lensing object by measuring the distortions of the emitting object.

The study of the cluster merger 1E0657–558, famously known as the bullet cluster, is a particularly well-known instance in which gravitational lensing was utilised [11]. The bullet cluster consists of two galaxy clusters that passed through one another 0.1-0.2 Gyr ago. Figure 1.2 shows the mass profile of the gravitational mass as the blue overlay and the baryonic mass as the red overlay in the optical image of the bullet cluster.

Figure 1.2 The optical data of the Bullet cluster with the gravitational lensing map (blue) and X-ray data (red) superimposed [12].

The gravitational mass of the colliding clusters was determined using weak gravitational lensing techniques, and the mass profile of the baryonic mass was determined by measuring the x-ray emission from the bullet cluster. A discrepancy was found between the mass distribution of baryonic mass and gravitational mass in the colliding clusters. Since the distribution of baryonic matter does not match that of the gravitating matter, it is likely that a non-baryonic component, such as dark matter, is responsible for gravitational lensing. Additionally, the distinct separation of the mass profiles shows that the non-baryonic dark component had negligibly weaker interactions, if any, than the hot baryonic gas during the collision, which slowed down the merger.

Cosmic Background Radiation

Indications of the early structure of the universe can be found in the cosmic background radiation, which can be used to constrain various cosmological parameters, such as the density of total matter, where it was discovered that non-baryonic dark matter makes up the majority of the matter.

380,000 years after the big bang, the temperature of the universe cooled enough to $\sim$3000 K, decoupling photons from matter, which allowed the photons to travel unimpeded throughout the universe. The relic photons remain today, although they have been redshifted into the microwave spectrum, observed as a near uniform temperature of 2.726±0.010 K [13]. However, small fluctuations in the cosmic background radiation temperature have been observed. Figure 1.3 shows these fluctuation in a temperature power spectrum of the cosmic background radiation from the Plank collaboration [14], where the multipole moment, l, in the x axis corresponds to the angular separation.

The peaks in the spectrum arise from oscillations before photons were decoupled from matter. These oscillations were due to opposing gravitational force and radiative pressure on the plasma, which became encoded in the photons once they were decoupled from matter. Since non-baryonic dark matter does not experience radiative pressure, information about the densities of the overall matter, baryons, and non-baryonic dark matter at the point of photon decoupling can be extrapolated from the position and relative heights of the peaks. A ΛCDM cosmological model fit to the acoustic oscillation data provides density parameters for the total matter, $\Omega_m = 0.315\pm0.007$, and for baryonic component, $\Omega_b h^2 = 0.0224 \pm 0.0001$ [15]. Using $h = H_0/100$ km s^{-1}Mpc^{-1}, where H_0 is the Hubble constant (67.4±0.5 km s^{-1}Mpc^{-1}), these results imply that $\sim 84\%$ of the total matter in the universe is comprised of non-baryonic dark matter.

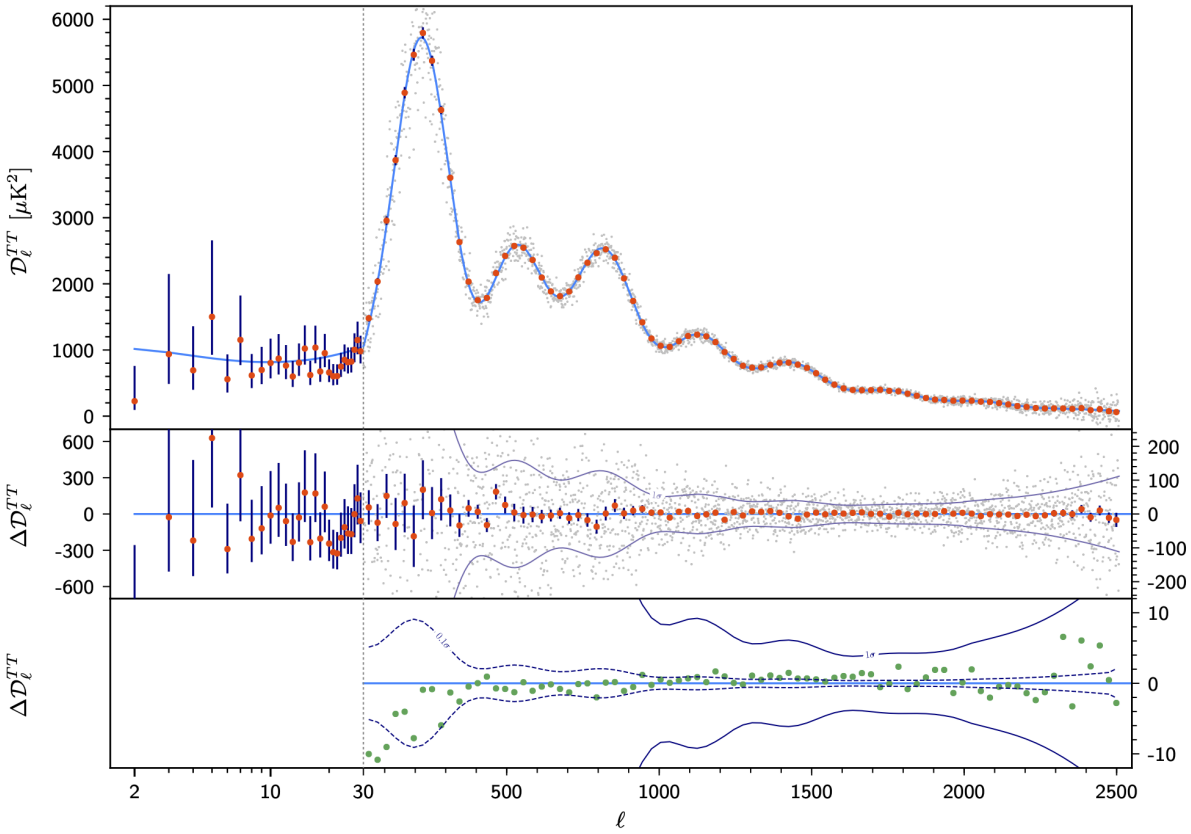

Figure 1.3 Power spectrum of temperature fluctuations in the cosmic background radiation [14].

Big Bang Nucleosynthesis (BBN)

An independent estimate of the fraction of baryonic matter in the universe may be obtained by studying the formation of light elements during the universe's early stages [16]. Big Bang Nucleosynthesis describes the production of light elements during the first three minutes of the Big Bang. In the first second, temperatures were high enough to maintain a thermal equilibrium in weak interaction as shown by

$$\mathrm{p} + \mathrm{e}^- \rightleftharpoons \mathrm{n} + \nu, \tag{1.10}$$

$$\mathrm{n} + \mathrm{e}^+ \rightleftharpoons \mathrm{p} + \overline{\nu}, \tag{1.11}$$

giving a 1/1 neutron to proton ratio. The slightly lower mass of the proton resulted in the equilibrium shifting towards the proton as the temperature decreased. At $\sim$ 1 second, the temperature has dropped to a critical temperature, resulting the neutron proton ratio to freeze

out to ∼1/6. Since free neutrons are unstable as shown by

$$\mathrm{n} \longrightarrow \mathrm{p} + \mathrm{e}^{-} + \overline{\nu}, \tag{1.12}$$

at ∼100 seconds their decay resulted in the neutron proton ratio of ∼1/7. After 100 seconds, the protons and neutrons began to fuse together to produce deuterium ^{2}H. Subsequent reactions resulted in the production of ^{3}H, ^{3}He and ^{4}He, until the temperature dropped sufficiently to stop nuclear fusion, and the relative abundances were fixed. The abundance of the light elements is dominated by ^{4}He, making up 25% of the primordial mass fraction. The remaining 75% consist of free protons and trace amount of light elements.

The relative abundance of the light elements produced in the Big Bang Nucleosynthesis depends on the rate of interaction, which is related to the baryon-to-photons ratio, η, given by

$$\eta = \frac{\eta_b}{\eta_\gamma}, \tag{1.13}$$

where η_b is the number density of baryons and η_γ is the number density of photons. Since the Big Bang Nucleosynthesis model is determined by a single parameter, η, it is possible to simulate the relative abundance of light elements as a function of η. The the density of baryons, Ω_b, can be calculated by fixing the value η_γ implied from cosmic background radiation measurement, and the theoretical predictions with astronomical measurements. Figure 1.4 shows the standard model Big Bang Nucleosynthesis predictions of abundance of light elements relative to H, as a function of baryon-to-photon ratio, η, and baryon density, $\Omega_b h^2$ [17].

The allowed regions from astronomical measurements are represented as yellow boxes. The observed abundance for elements lighter than ^{7}Li fits well with the BBN prediction and independent cosmic background radiation measurement. The discrepancy for the ^{7}Li case remains unresolved and known as the lithium problem [18]. Disregarding ^{7}Li , these results suggest a value for $\Omega_b < 0.052$, providing further evidence for that the majority of the universe is composed of non-baryonic dark matter.

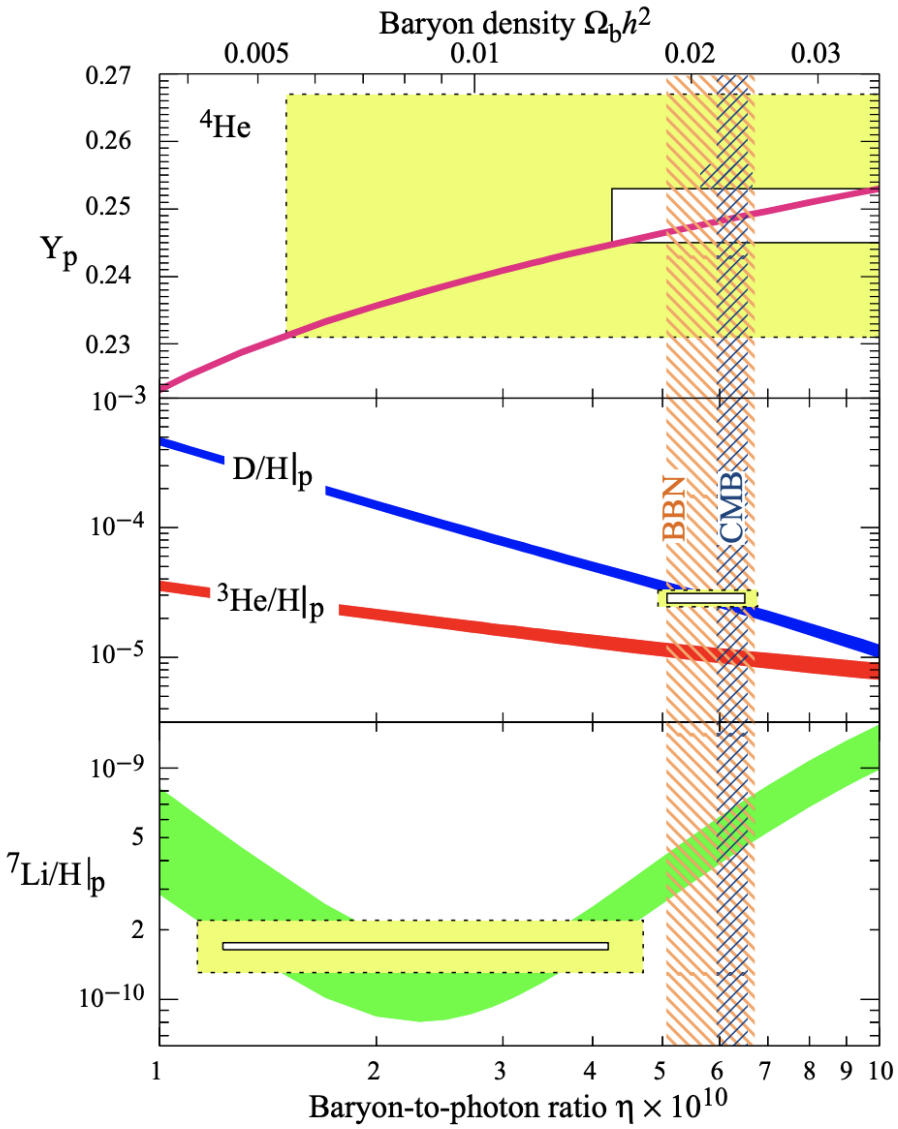

Figure 1.4 Plot shows primordial abundances of light elements as a function of Baryon-to-photon ration as predicted by Big Bang Nucleosynthesis. The allowed regions from astronomical measurements are represented as yellow boxes, blue vertical hatched band represent cosmic background radiation results [17].

1.1.2 Dark matter particles

Evidence presented in subsection 1.1.1 indicates that most of the contribution of matter in the universe is from a non-baryonic. Dark Matter is expected to have been non-relativistic at the epoch where it decoupled from photons, a requirement for the generation of large-scale structures in the universe [19]. Dark matter must also be stable, at least with a lifetime exceeding the age of the universe, so that it is still in existence today. Many models have proposed dark matter candidates beyond the standard model, but arguably the most favoured dark matter candidate is a family of particles called Weakly Interacting Massive Particle (WIMP), which are expected to be weakly interacting to allow for the required dark matter abundance at the time of decoupling [20]. The most popular non-WIMP candidates are sterile neutrinos and axions.

Non-WIMP candidates

Sterile neutrinos In the standard model of particle physics, there are three different neutrino types. Neutrino oscillations, which have been demonstrated to be a means by which neutrinos can change between the three types, require that they must have mass [21]. As a consequence of this requirement, it has been hypothesised that there are right-handed neutrinos which only interact gravitationally, known as 'sterile neutrinos'. The sterile neutrino would be heavier than the other types, providing a candidate for dark matter. In 2022, the Baksan Experiment on Sterile Transitions (BEST), an experiment investigating the 'gallium anomaly', found results that could be interpreted as evidence for oscillation between electron neutrinos and sterile neutrinos [22]. The gallium anomaly refers to the deficit of electron neutrinos observed in gallium-based radiochemical measurements with high-intensity neutrino sources. However, neutrino detectors, such as the MicroBoonNE experiment, have still not found any evidence of sterile neutrino [23]. There are current efforts to search for sterile neutrinos with greater sensitivity, with the Short-Baseline Neutrino (SBN) programme at Fermilab currently under construction which combines three neutrino detectors including SBND, Icarus and MicroBoonNE [24].

Axions The strong CP (charge-conjugation and parity) problem is absence of CP violation during strong interaction despite violation being permitted by the standard model. A proposed solution to this comes from the Peccei–Quinn theory, and a consequence of this solution is the Axion [25]. Since relic axions produced in the early universe can satisfy all the requirements of dark matter, it is considered as a possible dark matter candidate, with a DM mass range $\sim$1 μ to $\sim$1 meV. In the presence of a magnetic field, the axion has a non-zero probability

of converting into a photon, known as the Primakoff effect [26]. The Axion Dark Matter eXperiment (ADMX) is searching for axion via this mechanism, with their most result constraining the axion-photon coupling in 3.3–4.2 μeV mass range for the KSVZ model [27] and 2.7-3.3 μeV for the DFSZ model [28].

WIMP Candidates

WIMPs are hypothetical massive particles predicted to be neutral, non-relativistic, stable, and weakly interacting. WIMPs are expected to have been created thermally in the early universe with the other particles. When the universe was very hot, the production and annihilation of WIMPs were in equilibrium, resulting in large quantities of WIMPs being present with standard model particles. Interaction between standard model particles and WIMPs such that

$$\chi\overline{\chi} \rightleftharpoons q\overline{q}, \tag{1.14}$$

where χ denotes the WIMP, q is the SM particle, and the bar represents antiparticles. As the temperature fell below m_χ, the WIMP would be annihilated as production was suppressed, resulting in a cosmologically insignificant number of WIMPs. However, this is not the case as dark matter exists today. An explanation for this is that the Hubble expansion dilutes the number density of WIMPs, decreasing the chance of self-annihilation, eventually freezing out the number of WIMPs. The density at which freeze-out occurred is given by

$$\Omega_\chi \approx \frac{10^{-37} cm^3 s^{-1}}{\langle \sigma_a v \rangle}, \tag{1.15}$$

where $\langle \sigma_a v \rangle$ is the thermally averaged $\chi\overline{\chi}$ cross section multiplied by their relative velocity [20]. It was found that the annihilation cross section interaction required to generate the observed dark matter abundance is at the scale of the weak nuclear force. Figure 1.5 shows for a m_x=100 GeV correctly predicting the present day relic dark matter abundance. This suggested link between dark matter and the weak nuclear force has been dubbed the *WIMP miracle* leading to arguments that dark matter consists of particles in weak-scale masses. WIMP like particles are predicted by multiple theories that go beyond the standard model, such as the Minimal Supersymmetric Standard Model (MSSM) and the Universal Extra Dimensions Theory.

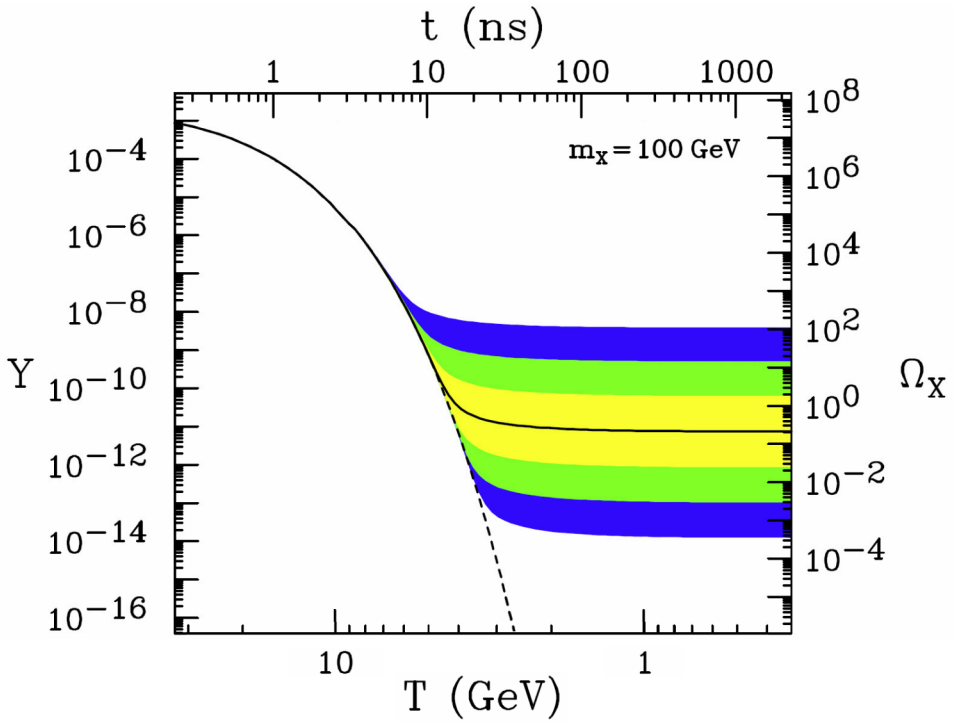

Figure 1.5 The comoving number density and as a function of temperature, time and density of the universe. The solid line corresponds to an annihilation cross section that yields the correct relic density, dashed lined corresponds to no freeze out [29].

Minimal Supersymmetric Standard Model A WIMP candidate called the neurtalino is predicted by the Minimal Supersymmetric Standard Model. The model was theorised to solve the gauge hierarchy problem but, as a byproduct, predicted a WIMP like particle, making it a popular model for the prediction for WIMPs. MSSM is a super symmetric extension to the standard model that requires the least number of new particles [30]. Figure 1.6, shows the standard model particles with their predicted supersymmetric partners. A key part of MSSM is R-parity, P_R, defined by

$$P_R = (-1)^{3B+L+2S}, \tag{1.16}$$

where baryon (B), lepton (L) and spin (S) the quantum numbers. The R-parity for a supersymmetric particle is -1 and for a standard model particle is +1. As a consequence of R-parity conservation, the Lightest Supersymmetric Particle (LSP) cannot decay into standard model particles. The neutralino is the LSP in MSSM, with a predicted mass of 10 - 1000 GeV [30]. This makes the neutralino a suitable WIMP candidate since it is stable and neutral with a mass within the expected range for WIMPs.

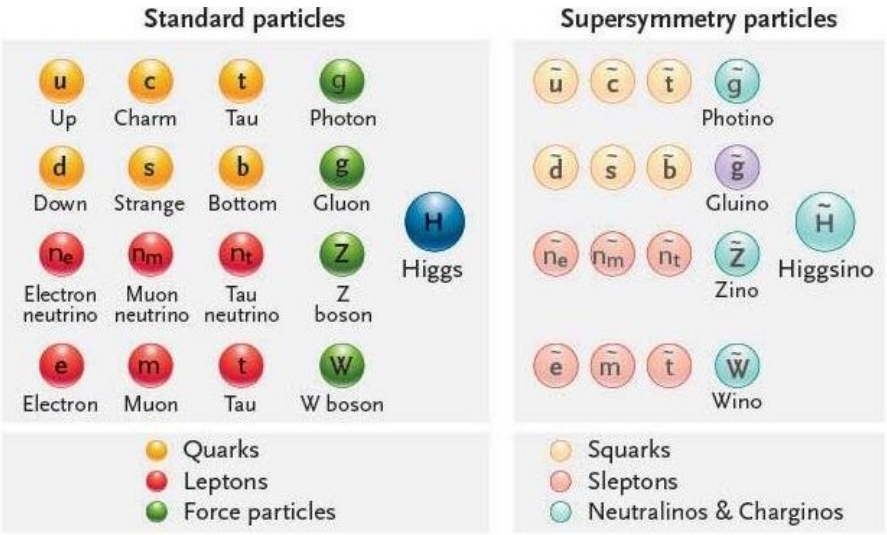

Figure 1.6 Table of particles in the minimal supersymmetric standard model [31].

Universal Extra Dimensions Theory Another WIMP candidate comes from the theory of Universal Extra Dimensions (UED). The UED model envisages a flat, small, compactified fifth dimension within which all the SM particles are allowed to propagate [32]. In this model there is KK-Parity, P_{KK}, define by

$$P_{KK} = (-1)^n, \tag{1.17}$$

which is analogous to R-parity in MSSM. Where n represents the KK level and is related to the mass of the KK particle. SM particles are assumed to be at KK level zero. The conservation of KK-parity results in the lightest Kaluza-Klein excitation of neutral electroweak gauge bosons, which is a stable and weakly interacting massive particle. Moreover, UED predicts the mass of the lightest Kaluza-Klein particle to be >950 GeV, making it a suitable WIMP candidate [32].

1.2 Experimental searches for WIMPs

There are three main methods to experimentally detect WIMP dark matter particles, illustrated in Figure 1.7. Collider search involves the production of DM particles from energetic collisions in particle collider experiments. Indirect detection refers to the detection of SM particles due to DM annihilation. Direct detection aims to detect the scattering of SM particles following a rare DM-SM interaction. Since direct detection is the most relevant detection technique for this thesis, the other approaches will only be covered briefly.

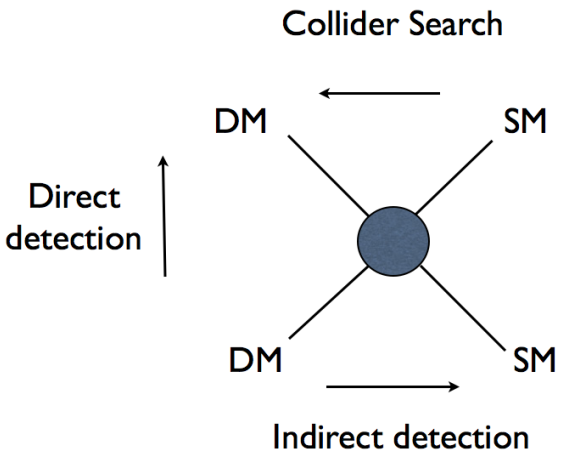

Figure 1.7 Schematic illustrating three experimental channels for dark matter detection.

1.2.1 Collider searches and indirect detection

Through the mechanism of inverse DM annihilation, collider searches seek to produce DM particles in high energy proton-proton collisions in colliders like the Large Hadron Collider (LHC) [33]. If produced, DM particles will not interact with any detectors in the LHC, but instead they will only be observed through missing transverse energy (MET). WIMP or other supersymmetric particles have yet to be detected in LHC collider searches [34].

Indirect detection aims to observe DM-DM annihilation and DM decay, resulting in detectable SM particles. Although these events are extremely rare, by observing regions with an expected higher dark matter density, these events can be inferred from an excess in SM background. High energy γ-rays, neutrinos, and charged cosmic rays coming from the Galactic Center, the Sun, or other massive objects are the main excesses that are being searched for. Some examples are the IceCube experiment [35], which is searching for dark matter annihilation to neutrinos in the sun, and the Fermi Large Area Telescope satellite experiment [36], searching for γ-ray emissions originating from the Galactic centre. For indirect searches, accounting for all possible backgrounds is the main challenge. The backgrounds are often considerable and difficult to quantify. In addition, interpretation of observed signal excess has proven to be difficult because astrophysical processes can produce similar signatures.

1.2.2 Direct detection

Direct detection experiments aim to observe the scattering of SM particles following a rare DM-SM interaction. In most cases, since the WIMP is electrically neutral, it will not interact with atomic electrons; instead, it will elastically scatter from the atomic nucleus, with the

transfer of momentum causing a nuclear recoil. Experimentally, the recoil of a target nuclei is detected via the production of light, heat, or ionisation in target material. The following subsection covers the detection principles for popular detector types used in direct detection experiments, the current status of searches, and the ultimate background for this method.

Cryogenic crystal detectors

A schematic of detection with crystalline cryogenic detectors is shown in Figure 1.8. These detectors measure the temperature increase due to particle interaction within a crystal. Temperature and heat capacity affect the sensitivity of these detectors. Therefore, to optimise sensitivity, detectors are kept at temperatures close to absolute zero and low heat-capacity crystals like Ge and Si are employed. Temperature changes are determined by the corresponding change in resistivity of a connected bolometer. These detectors often utilise a simultaneous measurement of ionisation to allow for signal background discrimination.

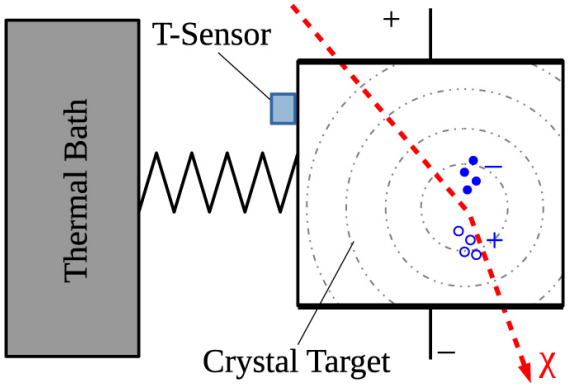

Figure 1.8 Principle of operation for cryogenic crystal detectors [37]

Examples of Cryogenic Crystal Detectors are: CRESST (Cryogenic Rare Event Search with Superconducting Thermometers) [38] running in Nazionali del Gran Sasso (LNGS), EDELWEISS (Expérience pour DEtector Les WIMPs En Site Souterrain) [39] experiment located at Modane underground laboratory (LSM) and CDMS (Cryogenic Dark Matter Search) [40] located at Soudan Underground Laboratory(SUL). While CDMS and EDELWEISS utilise semiconductor targets and can therefore access the ionisation channel, CRESST employs alternative crystalline materials, notably $CaWO_4$. These experiments were among the first to search for WIMPs, but they have proven difficult to scale up, so in recent years they have focused more on searching for WIMPs with lower masses.

Scintillating crystal detectors

Scintillator crystal detectors are another crystal-based detector but have a much simpler design, shown in Figure 1.9. They consist of high purity scintillator crystals, mainly NaI(Tl), coupled with a photomultiplier. Due to the high intrinsic background level of scintillator crystals, event-by-event detection of WIMPs is not possible. Instead, experiments based on this technology search for an annual modulation in the dark matter signal above a constant contribution from non-modulating backgrounds. The basis for this concept is illustrated in

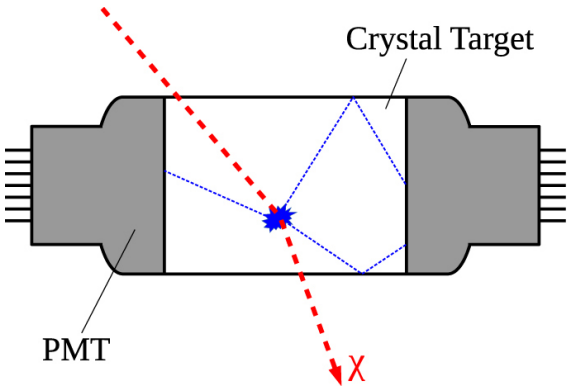

Figure 1.9 Working principle of scintillating crystals searching for an annually modulating signals [37].

Figure 1.10, the motion of the solar system causes a *WIMP wind* with an incoming direction towards the Cygnus constellation along the galactic plane. In the Earth's frame of reference, the velocity of the WIMP wind modulates as the Earth's velocity becomes parallel to it and opposes it in the months of December and June, respectively. This means that there is a modulation in the energy spectrum of nuclear recoils which, because the detectors have a fixed energy threshold, is expected to result in a modulation of the recorded event rate.

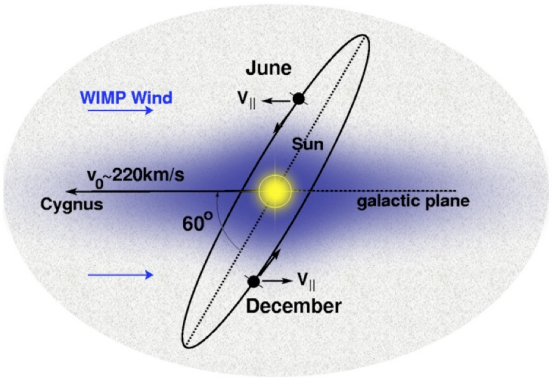

Figure 1.10 Depiction of the WIMP wind [41].

The DAMA/LIBRA experiment in LNGS has been running for over two decades, recently reporting an annual modulation at a 13.7 σ confidence level [42], shown in Figure 1.11. Many experiments disagree with this claim as exclusion limits on the WIMP-Nucleon Cross-Section has been set that excludes the DAMA/LIBRA result. However, almost all these experiments have achieved their sensitivity by means other than annual modulation and by using targets other than NaI. Recently a few new experiments have been developed in an attempt to directly confirm or refute the DAMA result by using NaI and annual modulation, notable COSINE-100 [43] and ANAIS (Annual modulation with NaI Scintillators) [44]. A possible explanation for the annual modulation observed by the DAMA/LIBRA experiment is from the analysis method they adopted. In 2022, this analysis was applied to COSINE-100 data, and a significant annual modulation was observed, indicating that the signal could be a statistical artefact [45].

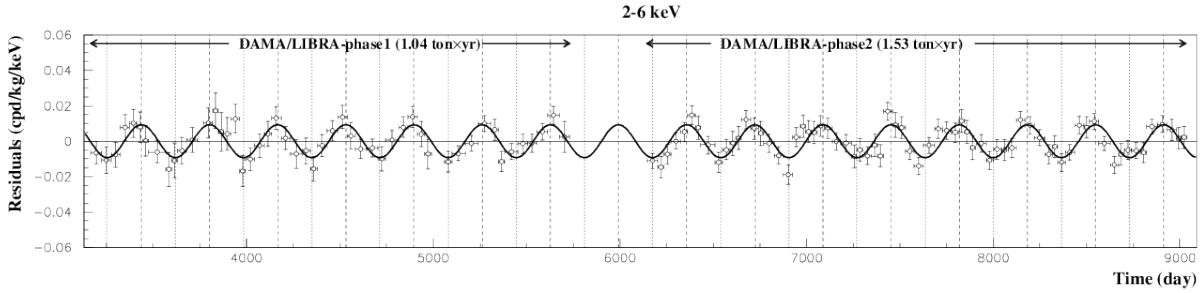

Figure 1.11 The annual modulation observed by the DAMA/LIBRA experiment [42].

Dual phase noble liquid detectors

Noble gases, specifically argon and xenon, have become popular for WIMP dark matter searches. Not only can they produce both scintillation light and ionisation in response to nuclear recoils but also have proved possible to build at the largest target masses of any WIMP detector type. Whilst single phase liquid experiments are feasible, for instance as built by the DEAP collaboration using liquid argon[46], so-called dual phase experiments have dominated the field so far. Such experiments use a liquid target phase and a gas phase, as shown in Figure 1.12. When an interaction occurs in the liquid target, it causes a primary scintillation signal (S1) and ionisation. The electrons produced during ionisation are drifted by the electric field towards the gas phase. The electrons produce a secondary scintillation signal (S2) when they collide with the gas atoms. Photosensors above and below the target measure the signals. the ratio of the total energies deposited in the S1 and S2 signals provides a powerful tool to discriminate between electron recoil backgrounds and nuclear recoils.

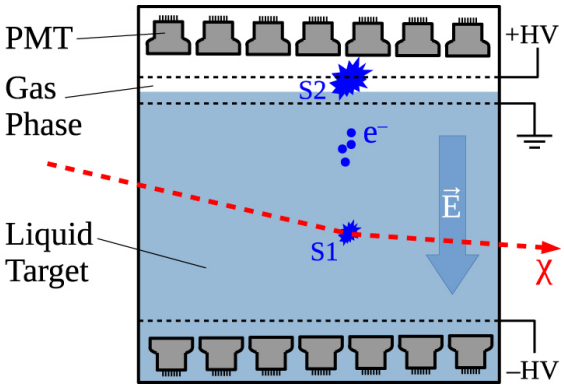

Figure 1.12 Working principle of dual-phase noble liquid detectors [37].

Noble gases Xe or Ar are used as they can be ionised easily and produce scintillation. Xe-based detectors have the advantage of high atomic mass, providing a large WIMP target and efficient self-shielding capabilities. Moreover, Xe does not require wavelength shifters to see scintillation. The advantages of Ar-based detectors is that Ar is readily available, making it significantly cheaper. In addition, Ar allows for better pulse shape discrimination. Examples of Xe-based dual phase noble liquid detectors are: XENON1T [47] located at LNGS, LUX-ZEPLIN (LZ) [48] located at the Sanford Underground Research Facility (SURF), and PandaX-II [49] located at China's Jinping Underground Laboratory (CJPL). The LZ experiment has the world-leading exclusion limits for WIMP mass above 9 GeV, with the most stringent limit set at 30 GeV [50]. An example of Ar-based dual phase noble liquid detectors is DarkSide-50, located at LNGS, which has the world-leading sensitivity in the mass range 1.8-3.5 GeV [51].

Current status and the neutrino floor

Figure 1.13 shows the current experimental exclusion limits for spin-independent WIMP-nucleon cross sections. Exclusion limits represent the area of the WIMP mass/cross-section parameter space to which each experiment was sensitive but did not report a detection. They are shown by coloured curves labelled with the name of each experiment. An exception is the crystal scintillation detector DAMA/LIBRA experiment, where their observed annual modulation is shown as contours. The current leading constraints are from dual phase noble liquid detectors, with LZ having the best sensitivity to WIMPs at the time of writing.[1]

The *neutrino floor*, shown with a dashed orange line in Figure 1.13, is a theoretical lower limit in the parameter space for direct detection WIMP searches due to the irreducible

[1]Note that the most recent LUX-ZEPLIN experiment results at time of writing, are not included in Figure 1.13 but can be found here [50].

background of neutrinos [52]. The neutrino background is due to coherent neutrino-nucleus scattering (CEνNS), mainly from solar, atmospheric, and DSNB (Diffuse Supernova Neutrino Background) neutrinos. The CEνNS process was recently demonstrated by the COHERENT collaboration using a neutrino beam [53]. The target that the experiment uses will determine where the neutrino floor is located since the CEνNS cross-section is dependent on the target nuclei and scales with the square of the target's atomic mass number. The neutrino floor shown in Figure 1.13 is for a Ge target.

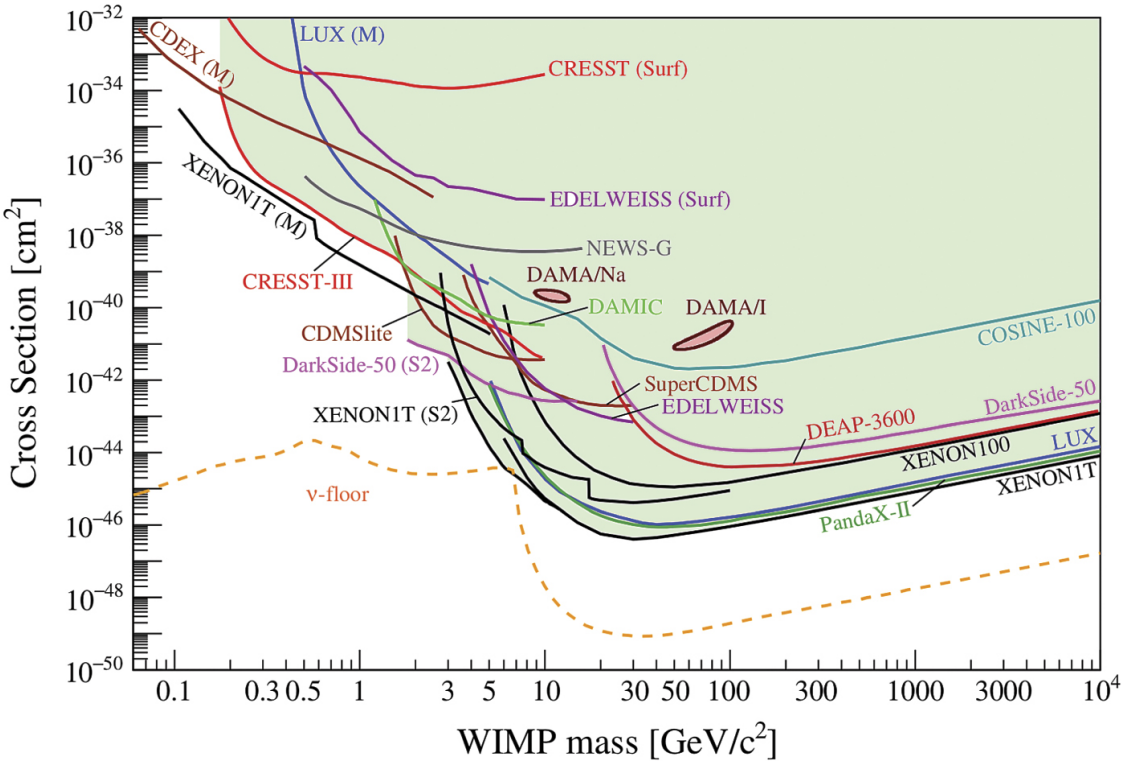

Figure 1.13 Current status of searches for spin-independent elastic WIMP-scattering [54].

Figure 1.14 shows a plot of projected sensitivity for next-generation DM experiments, with the neutrino floor for different targets shown in orange. The DARWIN (DARk matter WImp search with liquid xenoN) experiment is projected to be the most sensitive of the next generation of experiments, able to explore the entire WIMP parameter space until the background is dominated by CEνNS [55]. In the event that no WIMP signals are detected, this will lead to an ultimate discovery limit for these experiments. Using the WIMP wind and anticipated direction of incoming neutrinos, the experimental method of direct detection with directional information offers a way to probe lower cross sections below the neutrino floor. This concept is explored in the following section, Section 1.3.

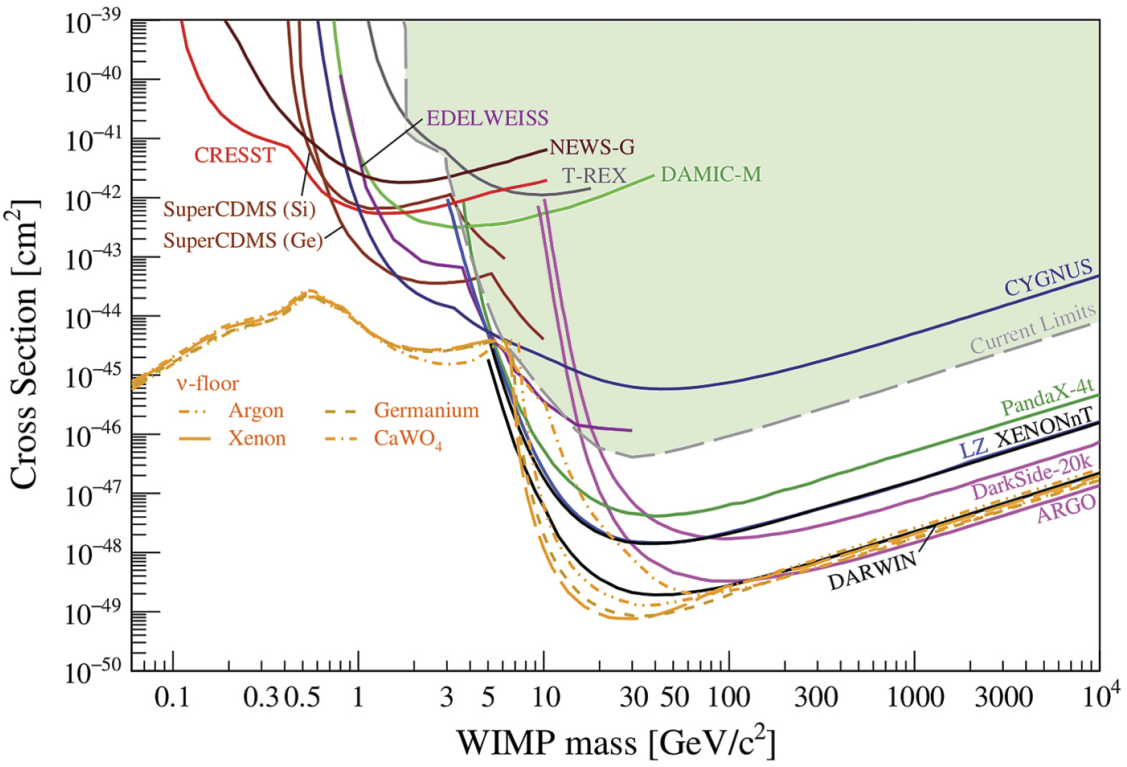

Figure 1.14 Next-generation experiment's sensitivity projections for spin-independent elastic WIMP-scattering searches [54].

1.3 Directional searches for WIMPs

Directional detectors have the capability of distinguishing against the otherwise irreducible neutrino background by adding information about the direction of the nuclear recoils induced by events. As the distribution of these directions for WIMP-induced interactions is expected to be very different from those induced by neutrinos or other backgrounds, direction detectors open the possibility of providing an unambiguous signal for dark matter that cannot be mimicked by any cosmic or terrestrial background. Given in this section are brief details of the origin of the dark matter directional signals and how this relates to the development of gas time projection chamber technology and use of SF_6 as relevant to the work of this thesis.

1.3.1 Directional signal

The directional signal arises from the relative motion of the solar system with respect to the Milky Way's DM halo. The motion of the solar system causes a WIMP wind with an incoming direction towards the Cygnus constellation along the galactic plane, resulting in a non-isotropic directional WIMP signal [56]. Figure 1.15a shows a plot of directional event

rates as a function of galactic coordinates with the WIMP signal highlighted in blue. Notice that solar neutrino signals in red, always originate from the elliptical plane. For a detector at a fixed location, the direction of these signals will appear to modulate over the day due to the Earth's rotation, as illustrated in Figure 1.15b. Although both directional signals from WIMP and solar neutrinos will oscillate, they will remain separate as recoils from WIMPs will be oriented in the direction of the WIMP wind, while those from solar neutrinos will be oriented away from the direction of the Sun. There are other astrophysical sources of neutrinos that can result in CEνNS such as atmospheric neutrinos and diffuse supernova neutrino background (DSNB). However, these background events can readily be rejected as they are approximately isotropic and will not oscillate [57], appearing with the same distribution in Figure 1.15c for both scenarios (1) and (2).

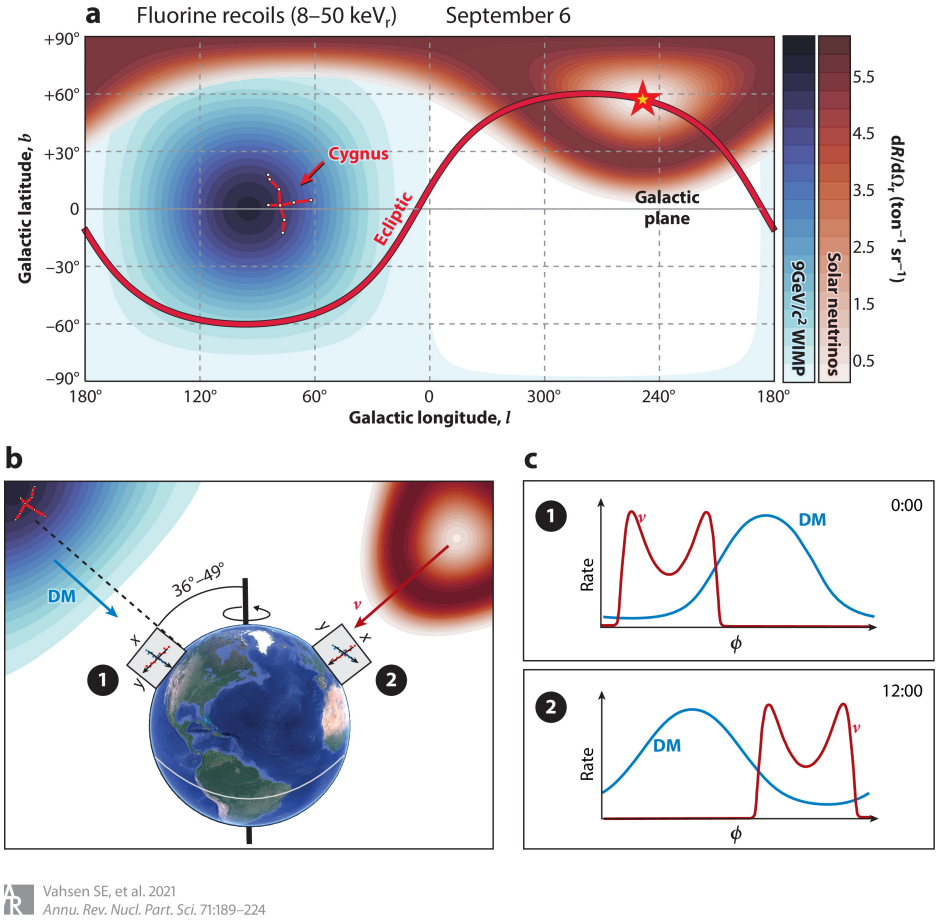

Vahsen SE, et al. 2021
Annu. Rev. Nucl. Part. Sci. 71:189–224

Figure 1.15 (a) shows the directional event rates from DM and solar neutrinos displayed in galactic coordinates. (b) depicts direction modulation over the day due to the Earth's rotation. (c) Shows event rate modulation over the day [56].

Directional information

The directional information from elastic scattering of a WIMP or neutrino is extracted from the recoil track produced by the target nuclei. Figure 1.16 shows the levels of directional information that can be extracted from reconstruction of the recoil track. Axial corresponds to information corresponding to the x, y, and z planes. For example, the orientation of nuclear recoil with respect to the WIMP wind. Head-Tail corresponds to information about the vector direction. For instance, if the nuclear recoil is towards or away from the Cygnus constellation.

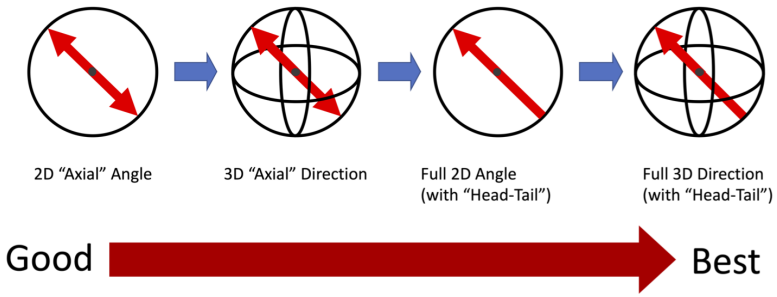

Figure 1.16 The different levels of directional information that can extracted from a single recoil event [58].

The level of directional information extracted from track reconstruction has statistical significance for the number of events required to reject an isotropic distribution of recoil directions [59]. A directional detector that can provide Head-Tail information, for example, only needs events $\mathcal{O}(10)$, whereas a detector that can only provide axial information needs events $\mathcal{O}(100)$, thus highlighting the importance of sensitivity to Head-Tail information.

1.3.2 Gas-based directional detectors

There are several approaches for directional detectors for instance use of film emulsions, as in the NEWSdm prototype experiments [60] and the possibility of using anisotropic scintillation crystals [61]. However, gas-based directional detectors are the most widely used method. Low pressure gas targets are used in directional detectors because they produce significantly longer nuclear recoil tracks than higher density target medium. The extended track allows more directional information to be extracted from the nuclear recoil. The principle for directional detection with a gas Time Projection Chamber (TPC) is shown in Figure 1.17. A recoiling nucleus ionises the target gas, leaving a charge trail, which is drifted by an electric field in the gas TPC towards the readout element. As only a small amount of charge is

produced during ionisation, the charge is first drifted to an amplification stage before the track readout element. For TPCs it is the quality and sophistication of the charge readout plane used that determines the level of directional information extracted as depicted in Figure 1.16.

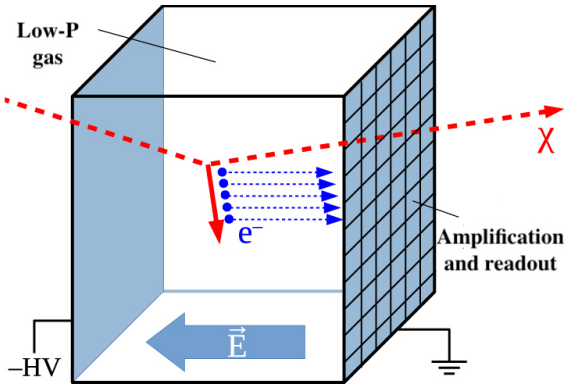

Figure 1.17 The principle for directional detection with a gas TPC [37].

There are only three directional detector experiments that have set WIMP exclusion limits. The DRIFT (Directional Recoil Identification From Tracks) detector, located at the Boulby underground laboratory; the NEWAGE (New generation WIMP search with an Advanced Gaseous tracking device Experiment) detector, located in the Kamioka underground laboratory; and The DMTPC (Dark Matter-Time-Projection Chamber) detector, located in the Waste Isolation Pilot Plant underground laboratory. Other gas-based directional detectors exist, but acts as development platforms for technologies that will eventually be applied to larger directional detectors such as CYGNO [62], CYGNUS-HD/D^3 [63] and MIMAC [64]. Most the world's activity in gas-based directional detectors have now joined forces in the CYGNUS proto-collaboration. This includes new efforts in Australia (at the new Stawell underground site), as well as USA, Japan, Italy and UK.

The DRIFT detector, shown in Figure 1.18a, uses a multi-wire proportional chamber (MWPC) readout in a TPC. The target gas mixture consists of CS_2, CF_4 and O_2, and has a detector target mass of 140 g. DRIFT is the most sensitive directional dark matter detector and has set limits on SD WIMP-proton cross section of 2.8 $\times 10^{-37}$ cm^2 for a WIMP mass of 100 GeV [65]. The NEWAGE detector, shown in Figure 1.18b, uses a micro-pixel (μ-PIC), a type of Micro-Pattern Gas Detector (MPGD), TPC in a target gas of CF_4 and has a detector target mass of 10 g. NEWAGE has set limits on SD WIMP-proton cross section of 5.0 $\times 10^{-35}$ cm^2 for a WIMP mass of 100 GeV [66]. The DMTPC detector, shown Figure 1.18c, uses a Charge-Coupled Device (CCD) camera optical readout to capture scintillation light generated in the amplification region. DMTPC uses a target gas of CF_4 and has a detector target mass of 3.3g. DMTPC has set limits on SD WIMP-proton cross section of 2 $\times 10^{-33}$ cm^2 for a WIMP mass of 115 GeV [67].

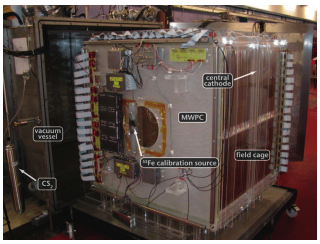

(a) DRIFT detector [68].

(b) NEWAGE detector [69].

(c) DMTPC detector [64].

Figure 1.18 Photos of the gas-based directional dark matter detectors that have set WIMP exclusion limits.

The nature of low-density targets means all detectors suffer from a small target mass. To observe WIMPs at the not yet excluded cross-sections, these detectors must scale to significantly larger volumes. The CYGNUS collaboration was formed to address this, with the goal of constructing a multi-site array of gas TPC directional detectors of a total mass scale of $\sim$ 1 tonne [70, 71]. The CYGNUS collaboration includes the majority of directional dark matter detection groups in the world, performing R&D to determine the optimum configuration for large-scale detectors. The main overall thrust is to develop the optimum affordable readout technology that can achieve high level of directional information with low threshold and low intrinsic background. Figure 1.19 shows the R&D work at proposed detector sites, analysing different detectors, readout technology and target gases. The work described in this thesis is part of the CYGNUS collaboration's target gas R&D.

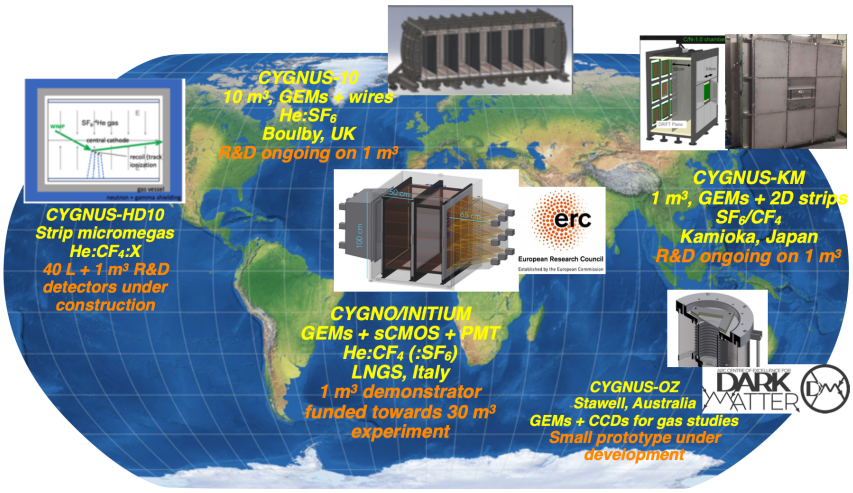

Figure 1.19 CYGNUS collaboration proposed detector sites and R&D detector configuration [72].

1.3.3 The case for SF_6-based gas directional detectors

One of the advantages of using gas-based detectors is the possibility of utilising a large variety of target nuclei. This includes the use of ^{19}F which allows good sensitivity to spin-dependent (SD) WIMP-nucleon interactions. CF_4 is a common drift gas and is used by DRIFT, NEWAGE and DMTPC experiments. While all the mentioned detectors used CF_4, DRIFT also adds CS_2 and O_2 to the mixture. The addition of these gases enables negative ion drift and fiducialisation with minority carriers.

In conventional gas TPCs, electrons are directly drifted to the readout, whereas in negative ion drift, anions are drifted. Negative ion drift is made possible by using an electronegative species in the target gas, which is achieved in DRIFT by CS_2. The electronegative species capture electrons produced along the ionisation track and generate negative ions. By drifting negative ions instead of electrons, diffusion during the drift process is reduced, providing better track resolution in the detector.

When using negative ion gases, it is possible that multiple negative ion species will be produced. If the other negative ions generated have different mobilities than the primary ion, the arrival times at the TPC readout will be delayed, resulting in a main peak and minority peaks. This enables the determination of the absolute position of interaction in the z-dimension, perpendicular to the readout, allowing for 3D fiducialisation and the potential for zero-background operation. In DRIFT minority peaks are achieved by the addition of O_2 to the target gas mixture [73]. Figure 1.20 shows an example of minority peaks in DRIFT detector signal with target mixture CS_2:CF_4:O_2.

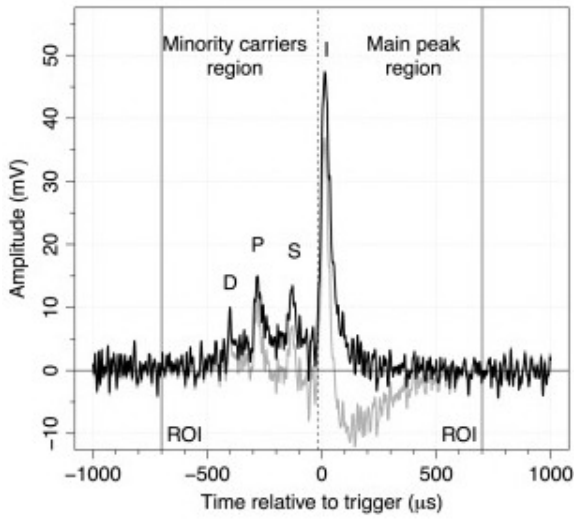

Figure 1.20 Minority peaks in DRIFT due to multiple negative ion species [74].

Although operation with CS_2 has been highly successful it does have particular issues, notably of toxicity and low gain. For these reasons alternative negative ion gases have be developed in recent years, most notably SF_6. SF_6 is an electronegative gas and has demonstrated the properties of negative ion drift and z-fiducialisation [75]. SF_6 also has a high ^{19}F content required for SD WIMP-nucleon interactions. The gas SF_6 can achieve the behaviour of target mixture CF_4 CS_2 and O_2, without the need of (non-SD) gases, increasing the total SD target. Another benefit of using SF_6 is that it is non-toxic, making it safer and simpler to handle than CS_2. These properties make SF_6 an ideal target gas for directional dark matter detectors.

Many significant advances have been made in recent years to show the feasibility of using SF_6 for large scale directional dark matter detectors. This includes demonstration of use with micromegas readout [58], use with optical techniques [76] and with hybrid wire-GEM readouts [77]. However, a significant issue for future SF_6-based large scale directional detectors is that SF_6 is a potent greenhouse gas and use of this gas is heavily regulated [78]. It is necessary to make efforts to stop the atmospheric emission of the greenhouse gas. One of the goals of this thesis, as covered in Chapter 6, is to determine how to minimise the amount of SF_6 used in such detectors, for instance by implementing gas recirculation systems.

1.4 Conclusions

The evidence described in this chapter has highlighted the case for the existence of dark matter constituting the majority of the universe's mass. Weakly interacting massive particles (WIMPs) are well-motivated dark matter candidates. Several experimental methods for searching for WIMPs by directly detecting rare baryonic-WIMP interactions were presented, but as next-generation experiments become more sensitive, they approach an irreducible neutrino background. The method of directional detection to overcome this problem, particularly directional detectors using low-pressure gas Time Projection Chambers (TPCs), was discussed. This thesis focuses on two separate issues affecting the performance of such detectors: (i) radon contamination from material emanation and (ii) gain-harming common pollutants from continuous outgassing. The importance and relevance of these topics are discussed, next in Chapter 2. As the novel properties of SF_6 has made it an ideal target gas for future large scale directional searches, development on addressing the issues above will be aimed specifically for SF_6-based gas TPC detectors in this thesis.

Chapter 2

Radon contamination and common pollutants in gas TPCs

The previous chapter discussed the motivation for using gas TPCs for directional dark matter searches. In this chapter, two independent problems with gas TPC operation for such searches are considered, issues with radon contamination and common pollutants. Although they are very different problems, they are linked by the possibility, explored in this thesis, that they can both be solved by the use of a new gas recirculation and purification system. An introduction to radon is provided in Section 2.1, followed by a review of radon contamination in dark matter experiments in Section 2.2. Finally, the effect of common pollutants in gas TPCs is discussed in Section 2.3.

2.1 Introduction to radon

Radon is a naturally occurring chemically inert gas with 39 known isotopes [79]. They are environmentally present in soil, bedrock, and water from the radioactive decay of radium. Radium isotopes are part of the uranium and thorium decay series, which are primordial elements of the earth's crust. The most abundant radon isotopes are ^{222}Rn and ^{220}Rn formed from the ^{238}U and ^{232}Th decay chains, respectively. Figure 2.1 shows the corresponding decay chains where the left side of the figure shows ^{238}U decay chain to form ^{222}Rn, and the right side shows ^{232}Th decay chain to form ^{220}Rn. The symbol in each bubble relates to the chemical element, while the numbers from top to bottom correspond to the atomic number, proton number, and radioactive half life of the element. Next to each arrow is the corresponding decay mode.

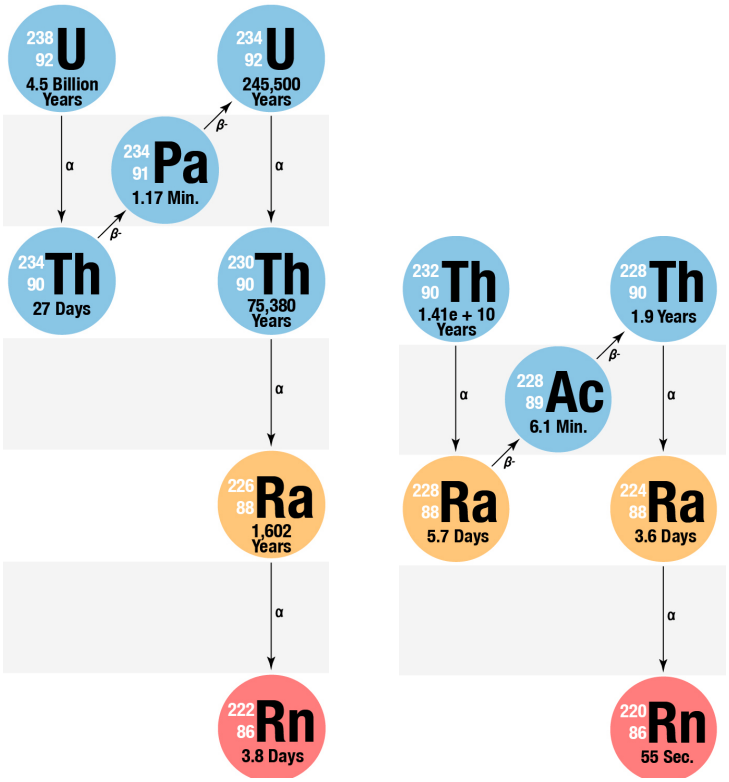

Figure 2.1 Left shows the ^{238}U decay chain to form ^{222}Rn, and right shows ^{232}Th decay chain to form ^{220}Rn.

The fact that radon is a noble gas is one of the main characteristics that make it more radiologically significant than earlier members of the uranium and thorium decay chains. As such, once it is formed in radium-bearing material, a radon atom can emanate from the material either by recoil or diffusion. Figure 2.2a shows recoil driven emanation, it occurs when the decay of radium, in this case ^{226}Ra, results in the recoil ejecting ^{222}Rn from the material. Figure 2.2b shows diffusion driven emanation, it occurs when the resulting recoil endpoint is still within the material, but there is a sufficient path for the radon atom, in this case ^{222}Rn, to escape the material. The rate of emanation for both mechanisms depends on the chemical structure and the volume to surface area ratio of the material, while diffusion driven emanation is also a function of temperature and carrier media [80, 81]. Once radon emanates, macroscopic transport is possible until it decays.

The radon isotope ^{222}Rn has the longest half-life of 3.8 days of all radon isotopes. This means it has ample time to emanate from its source before decaying. In contrast, the radon isotope ^{220}Rn has a half-life of 55 seconds, so relatively little emanates before decaying. As a result, the main isotope of concern with radon contamination in rare-event physics

experiments is ^{222}Rn. Note that from here, any reference to radon corresponds to the isotope ^{222}Rn unless stated otherwise.

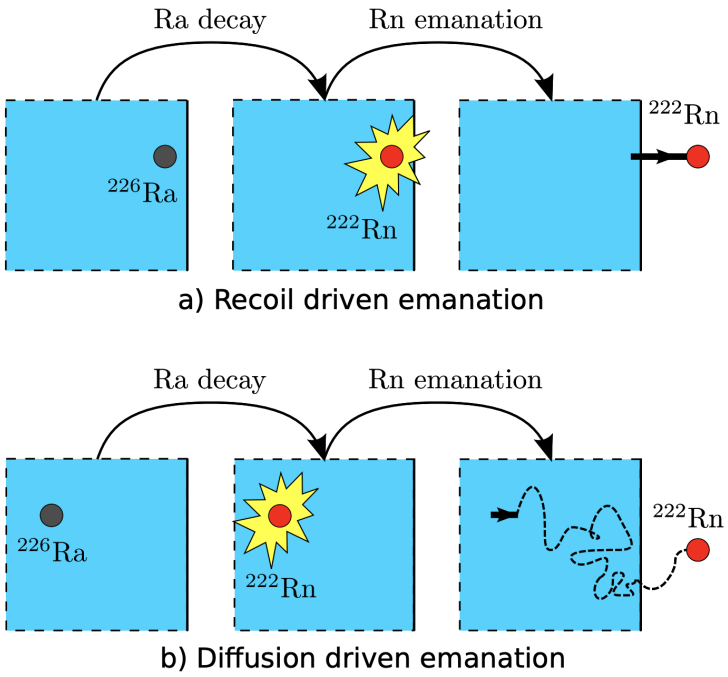

Figure 2.2 Schematic of radon emanation mechanisms via (a) recoil and (b) diffusion from radium-bearing material [82].

2.1.1 Radon progeny

The fact that radon decays into a number of short-lived radioactive products is an additional characteristic that makes it more radiologically significant than the earlier members of its decay chain. Figure 2.3 shows these *short lived* radon progeny, which all have half-lives of less than 27 minutes. Also shown in the figure are *long lived* radon progeny which are separated from the short lived progeny by the long half life of ^{210}Po. Both types of progeny are relevant to radon contamination in dark matter experiments, which will be discussed in Section 2.2 later. These radioactive radon progeny can emit either an alpha particle, beta particle or gamma-ray when they decay, as specified by symbols next to the arrow in Figure 2.3. The final decay product in this chain is ^{206}Pb which is chemically stable.

Early radon research was motivated by an understanding of the risk of radon on human health. Exposure to elevated levels of radon can result in the inhalation of its airborne

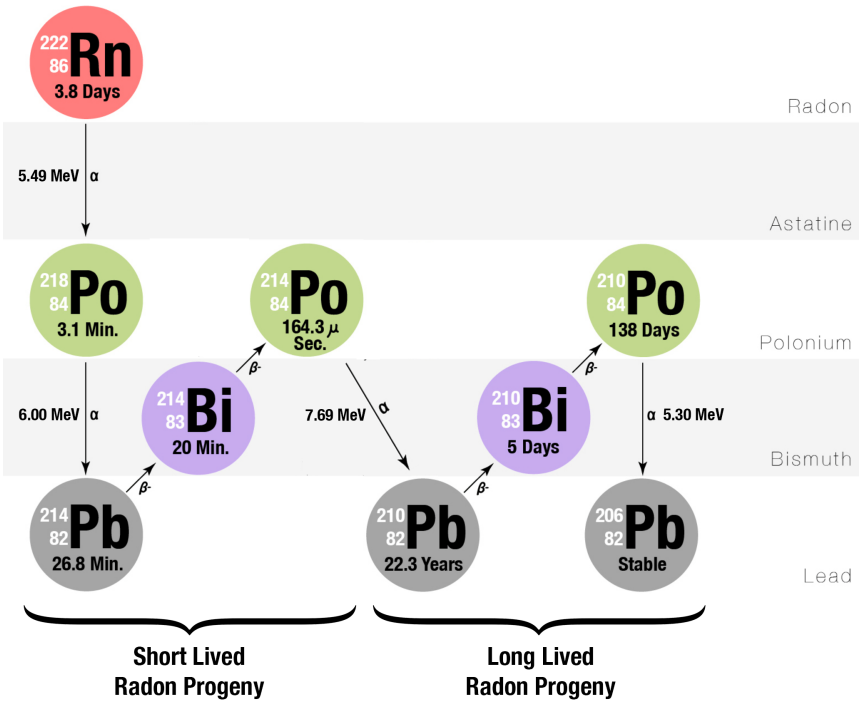

Figure 2.3 ^{222}Rn decay chain to stable ^{206}Pb, with *short lived* and *long lived* progeny shown by the curly brackets.

progeny, which can deposit onto lung tissue and alpha decay, significantly increasing the chances of developing lung cancer [83]. The process of progeny depositing onto macro surfaces is commonly known as *plate out*. The average radon level in UK homes is 20 Bq m^{-3} and makes up 48% of the average UK yearly dose [84]. However, radon levels can wildly differ depending on the location and building structure. For example, structures with sufficient ventilation can average levels comparable to open air $\sim$ 5 Bq m^{-3} [85]. Whereas, well-sealed structures like mines have been measured to > MBq m^{-3} [86]. Public Health England has considered that an indoor radon concentration of 200 Bq m^{-3} or greater is a significant health risk [84].

For rare-event physics experiments such as dark matter searches, the radon levels of concern are significantly lower than those for human health. For instance, in order for the LUX-ZEPLIN (LZ) experiment to reach its science goals, the radon concentration must not exceed 20 mBq in the 10 tonnes of xenon, which corresponds to 2 μBq kg^{-1} [87]. As a result, the source of radon in these experiments becomes any material involved in the experiment. Most manufactured materials will contain trace amounts of ^{238}U due to inevitable material contamination facilitated by its extremely long half life.

2.1.2 Radon measurement methods

An increased understanding of the risks of radon to human health prompted the development of radon instrumentation. These devices were later developed for application in different scientific fields. In the field of rare-event physics experiments, appropriate radon instrumentation is required to monitor ambient radon in the laboratory, screen detector materials, and measure the intrinsic radon level in detectors. An overview of passive and active radon measurement methods is given in this subsection, along with their application to the field of rare-event physics experiments.

Passive methods

Passive detection techniques involve a two-step process of radon collection followed by off-site analysis. Therefore, the passive method is unsuitable for continuous monitoring and is typically used for one-off radon measurements. Commercial examples of such devices are ion chambers [88], etched-tracked detectors [89], and activated charcoal adsorption [90]. In the field of rare-event physics experiments, the passive detection technique is used to measure very low radon concentrations. For example, low radon levels in large volumes can be concentrated onto activated charcoal [91] or organic scintillators with high radon solubility [92], resulting in a method with an extremely low minimum detectable activity $\sim$ 100 μBq. However, the minimum detectable activity achieved is also dependent on the active device used for the subsequent analysis.

Active methods

Active detection techniques utilises the method of direct radon collection and detection of radon and progeny decays. Therefore, these methods are employed commercially to produce all-in-one devices that provide collection, detection, and analysis. Active detection devices can provide continuous radon measurements, which is ideal for monitoring ambient radon levels in laboratories. Furthermore, these devices can be coupled with passive techniques to measure extremely low radon activity. They can also be used in different carrier gases to mimic target gases used in experiments. Three of the most common active detection techniques are Lucas scintillation cell, proportional counter and electrostatic collection. The mechanism for radon collection of each technique is outlined here using commercially available examples.

A Lucas scintillation cell is a scintillator counter for radon developed by H. Lucas in 1957 [93]. Figure 2.4a shows a Lucas scintillation cell device, which consists of a vessel with

its internal surface coated with scintillator ZnS(Ag). When an alpha particle is produced within the vessel and interacts with the scintillator, it results in a pulse of light. The flash of light is recorded and amplified by a photomultiplier tube and associated electronics which are optically sealed with the glass window. The gas enters the cell via a filter to stop radon progeny from entering the cell. Therefore, only the decay of radon and radon progeny produced in the vessel produces scintillation. Radon concentration is determined by the production of three observable alpha decays in the cell ^{222}Rn, ^{218}Po and ^{214}Po. PYLON is a good commercially available example utilising this method [94]. The sensitivity of Lucas scintillation cells is limited to about 0.5 Bq m^{-3} due to high background rates, unsuitable for levels required for rare-event physics experiments [95].

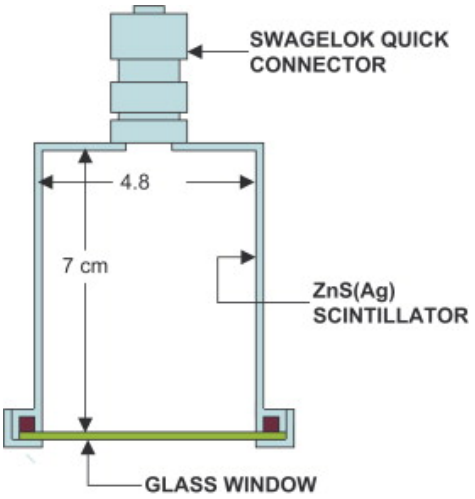

(a) Lucas scintillation cell [96].

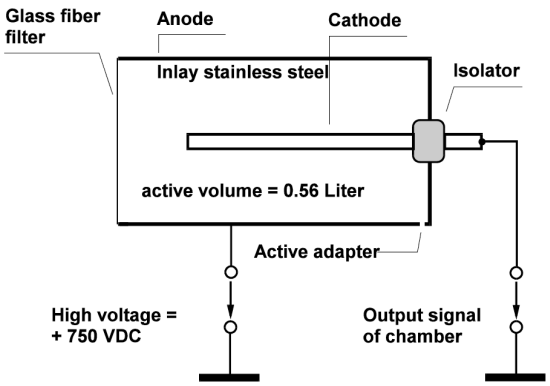

(b) Proportional counter [97].

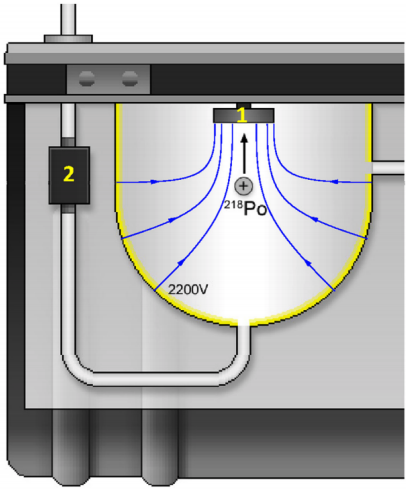

(c) Electrostatic collection [98].

Figure 2.4 Commercial examples of radon measurement devices utilising different methods

The proportional counter method uses an applied electric field in a chamber to collect ions produced by radon and radon progeny decays to measure radon concentration [99]. AlphaGuard is a good commercially available example utilising this method, as shown in Figure 2.4b [97]. The device consists of a cylindrical chamber with a metallic interior at an elevated voltage and a central electrode at 0V. The difference in voltage creates an electric field that causes radon-induced air ions to drift towards the central electrode. A glass fibre filter stops radon progeny from entering the chamber. Therefore, only radon decays and its progeny decays in the chamber produces the measured ions. A custom proportional counter device, originally developed for the GALLEX solar neutrino experiment, has been demonstrated to achieve a minimum detectable activity of 100 μBq when coupled with the activated charcoal method for radon emanation measurements [91].

The electrostatic collection method uses an electric field to collect charged radon progeny. It detects subsequent alpha decay from the collected radon progeny to measure radon concentration. An example of a commercial device that uses this method is the DURRIDGE RAD7 [98], shown Figure 2.4c. The device consists of a dome at an elevated voltage and a solid-state alpha silicon detector at 0V. Gas samples are pumped in via a filter to stop radon progeny from entering the dome. Therefore, only radon that has decayed in the sample volume is measured. Once radon decays inside the dome, the electric field causes charged radon progeny to drift and implant onto the silicon detector. Since the radon progeny is implanted, greater alpha decay energy resolution is achieved. In fact, the alpha decay for a specific radon progeny can be identified, as shown in Figure 2.5.

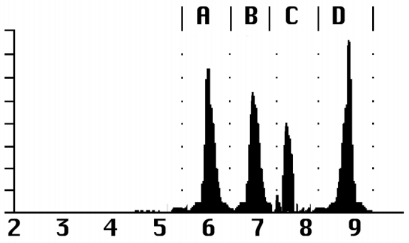

Figure 2.5 Alpha spectrum from RAD7. Peaks correspond to the collected radon progeny alpha decay. $^{218}Po^{+}$ (window A), ^{214}Po (window C), $^{218}Po^{+}$ (window B), and ^{212}Po (window D) [98].

The electrostatic method's ability to identify the specific radon progeny from its alpha decay energy makes it possible to distinguish between radon isotopes ^{222}Rn and ^{220}Rn. For instance, referring to Figure 2.5, ^{222}Rn progeny decays are collected in windows A and C. Whereas for ^{220}Rn they are collected in windows B and D. Moreover, unlike all the other active methods, contamination from long-term progeny background ^{210}Pb can be discarded.

The electrostatic collection method is the most commonly used radon measurement technique in the rare-event physics field, with custom devices, achieving sensitivities $\sim$ 1 mBq m^{-3}[100].

2.2 Radon contamination in DM experiments

While radon poses problems for other rare-event physics experiments, such as neutrinoless double beta decay searches [101, 102], this work focuses on radon contamination in dark matter searches. This section gives an overview of radon-induced backgrounds, sources of radon in experiments, and radon suppression strategies, with a focus on radon mitigation.

2.2.1 Radon-induced backgrounds

When considering detector backgrounds relating to radon, the primary decay is not normally an issue because, as the isotope is a gas, the alpha particle released is likely to deposit high energy within the fiducial volume, typically all or most of 5.49 MeV in the case of ^{222}Rn. It is instead the resulting progeny where the problems begin. Unlike ^{222}Rn, ^{218}Po is solid at room temperature and pressure, and the generated polonium specie from the radon decay is positively charged 88% of the time [103], consequently the ^{218}Po can readily plate out onto the detector walls. There are three mechanisms that can produce unwanted backgrounds from plated out polonium, as depicted in Figure 2.6: nuclear recoil, neutron emission, and electron recoil. It should be noted that these mechanisms could arise from plated out polonium from both short lived and long lived progeny, therefore isotopes are not specified in the figure.

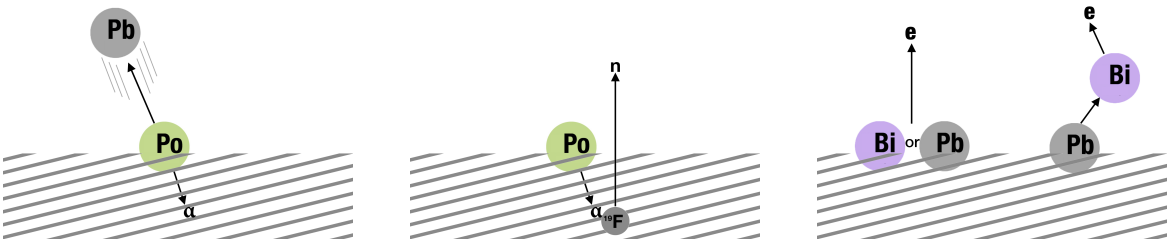

(a) Nuclear recoil (b) Neutron emission (c) Electron recoil

Figure 2.6 Mechanism for radon-induced backgrounds. Lined grey area corresponds to the detector wall, and white area directly above is the target volume.

A lead nucleus and an energetic alpha are produced when polonium decays. Figure 2.6a shows the case where the plated out polonium alpha decays into the detector walls, resulting in the lead nucleus recoiling into the detector volume. This slowly recoiling lead nucleus

can interact with the target medium, resulting in a nuclear recoil signal similar to that of a WIMP. The energy of the lead recoil is dependent on the implantation depth of the plated out polonium. This background is the most relevant for gas TPCs and was a significant background in the DRIFT experiment [104].

An alpha decay into the detector walls can also produce a neutron from an (α, n) reaction occurring with nuclei in the wall material. This process will depend on the composition of the detector wall. For instance, polytetrafluoroethylene (PTFE) is commonly used in the walls of liquid noble gas detectors and has a high (α, n) yield due to its high fluorine content. Figure 2.6b illustrates how the alpha decay of the plated out polonium can interact with fluorine in the PTFE detector material, producing a neutron emission into the target volume. In some cases the neutron will escape the fiducial volume and not cause a problem, however, there is the possibility that the neutron will interact with target nuclei to produce a low energy nuclear recoil similar to that expected from WIMP interactions.

Electron recoil background arises from the beta decay of bismuth or lead, as illustrated in Figure 2.6c. The beta decay of bismuth or lead can produce electron backgrounds near the walls or in the detector volume. A single scatter electron recoil event in the WIMP region of interest occurs when ^{214}Pb decays into the ground state of ^{214}Bi without any accompanying γ-emission, known as a naked-β decay. This background accounts for 66% of the projected electron recoil background in the LZ experiment [105].

2.2.2 Sources of radon in experiments

Radon-related backgrounds in dark matter experiments arises mainly from two factors. Firstly, intrinsic contamination of detector materials with radon via the ^{238}U chain, and secondly, due to progeny plate out on detector material from *ambient radon* during manufacture and assembly, before detector runs. To combat this, most experiment collaborations undertake extensive measurements of the radon content of all detector components used. Methods to measure the intrinsic radon contamination of materials will be discussed in subsection 2.2.3.

Contamination from ambient radon occurs when radon from the surrounding environment plates out onto the detector material surfaces and remains there until the detector is operational. The construction of these experiments can take many years and involves the transport, storage, and handling of detector components. During this time, the components are exposed to radon from the atmosphere and the ambient radon at the detector site. Due to the long timescales between component production and detector operation, the resulting radon-induced backgrounds arise from long-lived progeny.

The average radon concentration in the atmosphere is ~ 5 Bq m^{-3}, whereas the ambient radon at detector sites can reach much higher levels. Experiments are located in deep

underground laboratories to reduce the impact of cosmic ray muons, as highlighted by Figure 2.7. Unfortunately, underground laboratories provide a perfect environment for the accumulation of radon, as they are well-sealed and surrounded by bedrock. Many underground laboratories use infrastructure from active or unused mines. For instance, the Kamioka Observatory underground laboratory is located in the Mozumi mine, where radon levels in the mine tunnels have been measured to exceed 2000 Bq m^{-3} [106]. To mitigate this, underground labs use atmospheric air to ventilate the lab environment. However, even with ventilation, the typical radon concentration in underground laboratories is $\sim$ 100 Bq m^{-3} [107].

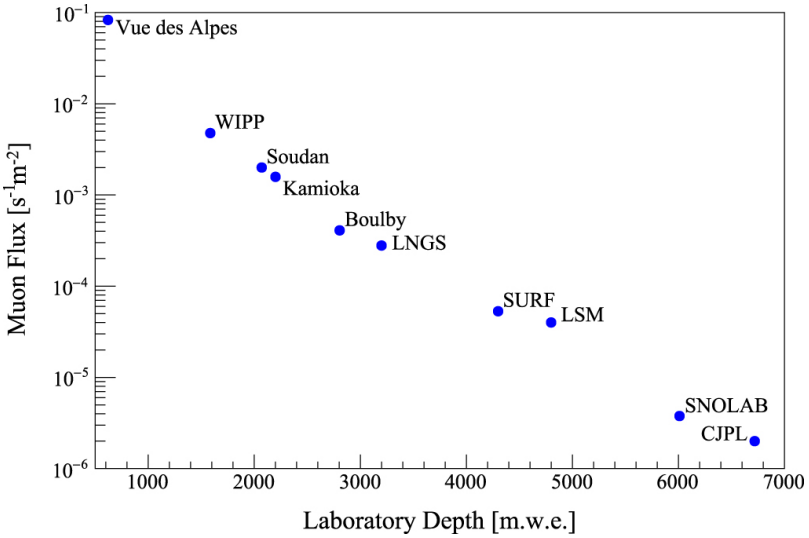

Figure 2.7 Muon flux as a function of depth in meter water equivalent for various deep underground laboratories [108].

2.2.3 Radon suppression strategies

There are two strategies to suppress the effects of radon-induced backgrounds: signal discrimination and radon mitigation. Signal discrimination concerns the rejection of events suspected to be induced by radon. Identifying coincident alpha decays or the source of background events allows for event tagging and detector fiducialization, respectively. Radon mitigation corresponds to managing the amount of radon introduced to the detector through prevention or active removal. This section focuses on the latter technique, as it is most relevant to the work conducted in this thesis.

Screening material for radon emanation

The effects of radon can be effectively managed by material selection. Screening of candidate materials is typically done by directly measuring radon emanation from the material of interest. The emanation of radon is measured by placing the material of interest into a hermetically sealed chamber. The chamber is evacuated to remove any trapped radon and is filled with low-radon carrier gas. Once sealed, radon emanates from the material of interest and accumulates according to

$$C(t) = C_s \times (1 - \exp(-t/\tau)), \tag{2.1}$$

where C is the radon concentration, C_s is the radon concentration at secular equilibrium, t is the emanation time, and τ is the lifetime of ^{222}Rn. An emanation time $\sim$ 30 days, allows the chamber to approximately reach secular equilibrium, which can be considered to be the maximum concentration of radon emanating from the material of interest. It is common for measurements to use shorter emanation times, which is corrected for in the analysis. After a set emanation time, the gas in the chamber is extracted, and the radon emanated from the sample is measured. Radon measurements can be made directly from the chamber gas using an active device or in a two-step passive technique involving radon enrichment followed by analysis (see also subsection 2.1.2 above) . To achieve high-sensitivity emanation measurement, it is crucial to minimise the background activity of the carrier gas and measurement apparatus.

Figure 2.8 shows an example of a radon emanation setup using the enrichment process with an activated charcoal *Rn trap*. Samples of interest are placed in either the 20 L or 80 L emanation chambers and are filled with low-radon helium. After a set emanation time, the accumulated radon is transferred by the helium carrier gas to the activated charcoal trap. The trap with captured radon is afterwards disconnected and attached to a radon detector, in this example a proportional counter. This setup achieves an absolute sensitivity of 40 μBq with a minimum detectable activity of 100 μBq [91].

As mentioned in Section 2.1, radon emanation from materials is driven either by recoil or diffusion, where the rate of diffusion is a function of temperature. Due to this dependence uncertainties in interpolation can occur when radon emanation results are applied to experiments operating at low temperatures. Radon emanation measurements must be taken in conditions that mimic experimental operation to account for this. To the authors knowledge only one cryogenic radon emanation facility exists, called the Cold Radon Emanation Facility (CREF), which is located in the Rutherford Appleton Laboratory (RAL) [109].

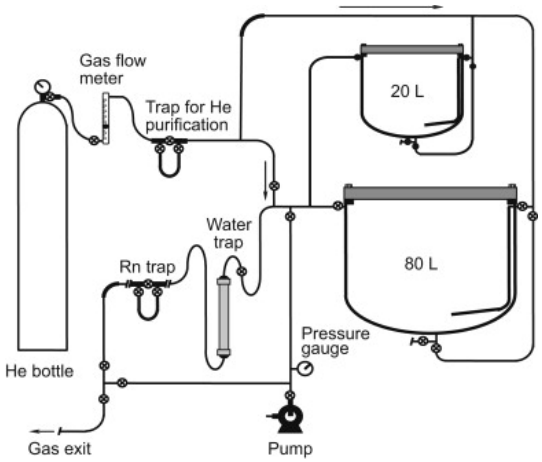

Figure 2.8 Schematic of radon emanation setup using the passive enrichment process with an activated charcoal trap [91].

Mitigation against ambient radon

The effect of radon progeny plate out can be measured using surface α-counters, such as the XIA UltraLo-1800. This device measures surface α by detecting the ionisation it causes in an argon filled UltraLo-1800 chamber. Such a device can reach a surface ^{210}Po sensitivity of < 0.1 mBq/m^2 [110]. Plated out radon progeny can be removed from material surfaces by using techniques such as acid etching and electropolishing [111]. However, prevention of initial plate out to these surfaces from ambient radon remains the best solution.

The impact of ambient radon can be suppressed during transport and storage by sealing materials in radon barrier bags with low radon gas ~ 0.1 mBq m^{-3} [112]. However, to prevent plate out during detector fabrication, assembly, and commissioning, low-radon clean rooms are required. Radon-reduced environments are achieved by actively removing radon from the ambient air, typically by the technique of radon adsorption on activated charcoal. ATEKO manufactures a Radon Abatement System (RAS) that utilises this technique, which is used by a number of underground laboratories such as LNGS, SURF, LSM, Y2L and CJPL [113]. Figure 2.9 shows a schematic of the ATEKO RAS system.

The ambient air is pressurised to 10 bar, where it is flowed through a dryer to remove humidity. This allows the purified air to be cooled down to -60 °C, improving the activated charcoal radon capturing efficiency. The cooled air is then filtered through two large activated charcoal columns to remove radon. Before the radon-reduced air is introduced to the clean room, the air passes through a HEPA (High Efficiency Particulate Air) filter to remove dust and is heated to room temperature. The lowest radon concentration delivered by this system is 1 mBq m^{-3}, from an initial ambient radon concentration of 70 Bq m^{-3} at the Laboratorio Subterráneo de Canfranc (LSC) [115].

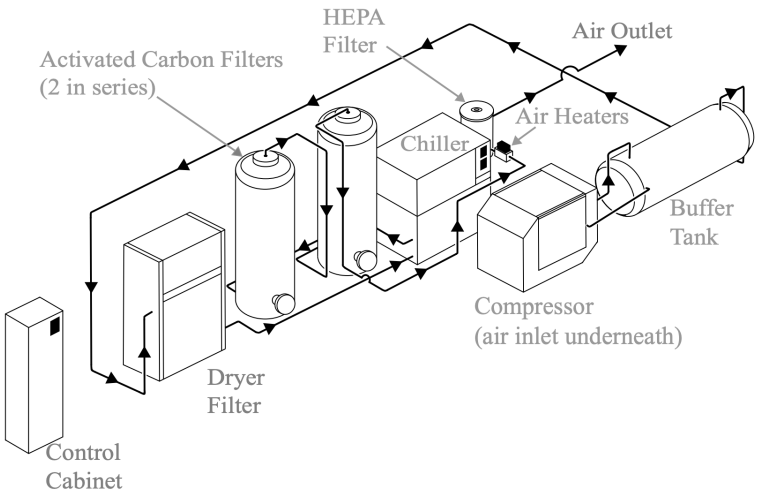

Figure 2.9 Diagram of the ATEKO Radon Abatement System [114].

The ATEKO RAS system is an example of a continuous flowthrough filtration technique. The time it takes for activated charcoal to become saturated is called the *breakthrough time*. When the breakthrough time is reached, the columns will need to be replaced. The ATEKO system improves breakthrough time by using large columns and operating at a low temperature. An alternative filtration technique is Vacuum Swing Adsorption (VSA), which enables on site regeneration of the activated charcoal, allowing continuous long-term operation. This method has the potential to outperform a continuous flowthrough system at a lower cost [116]. A notable example of a Vacuum Swing Adsorption system is used in ultra-low radon clean room commissioned at the South Dakota of Mines and Technology (SDMST) [117]. The VSA system consists of dual columns in parallel, as shown in Figure 2.10. The dual column parallel configuration enables one filter to remove radon while the other is being vacuum regenerated. After a calibrated filtration time, before the breakthrough time, the columns are *swing*-ed from vacuum regeneration and radon filtration and vice versa. The radon concentration delivered by this system is 100 mBq m^{-3}, from an ambient radon concentration of 60 Bq m^{-3}.

Many factors can account for the differences in the performance of ATEK and VSA systems, including operational temperature, flow rate, and the size of filtration columns. The VSA system operated at 16°C, while the ATEKO system operated at -60 °C. In addition, the VSA system used 125 kg of activated charcoal during filtration, whereas the ATEKO system used $\sim$ 1000 kg.[1] Considering that operational temperature and column size significantly

[1]Estimated from an activated charcoal density of $\sim$ 500 kg m^{-3} [118] and the stated ATEKO total tank volume of 2m^3 [114]

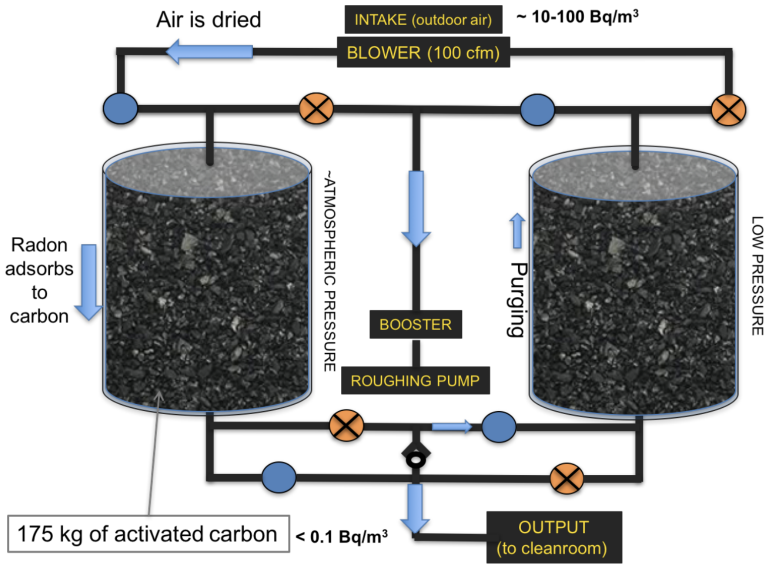

Figure 2.10 Schematic of Vacuum Swing Adsorption System from SDMST [117].

favour the ATEK RAS, a VSA system of comparable size operating at a lower temperature may produce even lower radon concentrations. In Chapter 6, the VSA technique will be used to design a gas system.

Active removal from target material

Once an experiment has been built, the intrinsic radon background from the detector materials is fixed. The only way to reduce this background is by actively removing radon from the target material. Radon is constantly generated inside the detector volume due to the emanation from the walls and any materials exposed to the detector volume. As previously mentioned, in a closed system, the radon concentration accumulates according to Equation 2.1 until a maximum radon concentration at secular equilibrium is reached. In the case of liquid and gas targets, one way to deal with this is to prevent the accumulation of radon by maintaining a constant flow of *fresh* target material. For instance, DRIFT employs this technique by constantly flowing fresh gas into the detector volume, using the gas system shown in Figure 2.11.

The DRIFT gas system consists of a mixing station coupled to a supply chamber, which inputs into the detector vessel. A pressure gradient between the supply chamber and the detector vessel drives the flow of fresh gas, effectively purging any radon in detector volume as a result of detector material emanation. The flow of fresh target gas is set to replace one

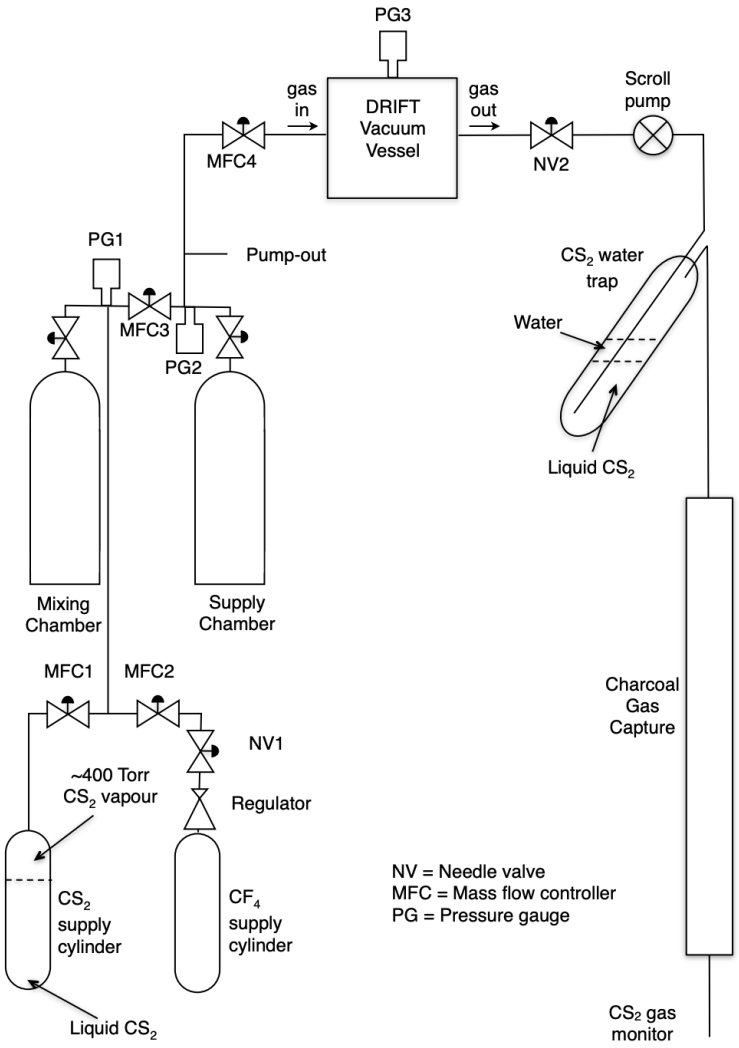

Figure 2.11 Diagram of the DRIFT detector continuous flow gas system consisting of a mixing and supply chamber, which feeds into the detector vessel, and outputs to a charcoal gas capture system for disposal [119].

detector volume daily. According to Equation 2.1, this limits the accumulation of radon to $\sim$ 17% of the maximum concentration at secular equilibrium.

For experiments using expensive or difficult-to-dispose target materials, the method of continuous flow is unsuitable. Instead, inline radon removal systems are employed; such systems counteract the emanation of radon by actively removing radon from the target material. Since the radon removal system is in a close loop with the detector, radon emanation will reach the maximum concentration at secular equilibrium. However, this concentration is suppressed by the active radon removal, resulting in a new equilibrium at a lower radon concentration.

Inline systems are the only option for active radon removal for xenon experiments because the target material is expensive and must be recycled. However, since both radon and xenon are noble gases, their chemical properties are very similar, making separation difficult. Techniques for separation include preferential adsorption to activated charcoal [120] and cryogenic distillation [121]. Figure 2.12 shows an example of an inline radon removal system, used as part of the xenon recirculation in LZ [87]. The radon removal line uses a cold activated charcoal trap to remove radon from gaseous xenon. In this system, only the xenon gas from low flow regions is filtered since the flow rates necessary for activated charcoal adsorption make it impractical for the full system.

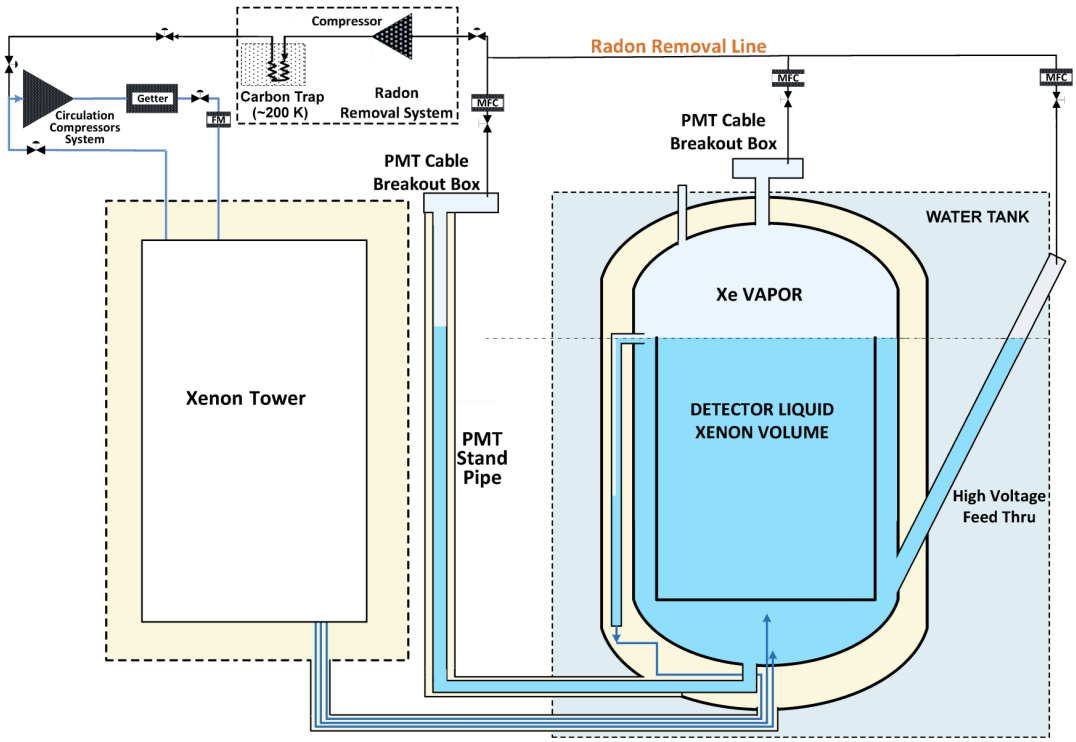

Figure 2.12 A schematic of xenon recirculation in LZ showing the radon removal system on the top left [87].

As mentioned in Chapter 1, SF_6 is an ideal target gas candidate for future directional dark matter experiments. Since SF_6 is a potent greenhouse gas, the continuous flow method to remove radon is unsuitable. Instead, an inline radon removal system is required to prevent the release of greenhouse gas. Activated charcoal has been extensively used in the removal of radon [116, 118, 120], which can potentially be applied to a carrier gas of SF_6. However, activated charcoal is also known to absorb this gas. Other adsorbents exist, such as Molecular Sieves (MS) which have the potential to remove radon with better selectivity

without absorbing the target gas. An investigation into using MS filters to remove radon from SF_6 is conducted with the results reported in Section 4.2.

2.3 Common pollutants in gas TPCs

Although gas TPC detectors are designed to be leak-tight, miniature leaks and outgassing will introduce common pollutants (O_2, N_2 and H_2O) into the detector volume. The presence of such pollutants influences the detector's gas amplification performance. The mechanism for electron amplification in gas TPCs is described in this section, which is then followed by a discussion of the effects of pollutants and possible solutions. The problems associated with radon contamination, regarding background events as covered in Section 2.2, are not directly related to common pollutants discussed here. However, a link does exist, and forms a major topic for this thesis, in the potential idea that both can be tackled by using the same mitigation strategies involving molecular sieve filters.

2.3.1 Electron amplification

The principle of detection with gas TPCs was previously described in Chapter 1. The amplification of electrons before the readout element is a crucial stage in gas TPC detectors. Gas electron amplification can be generated by a variety of different devices, which all operate using a region of a high electric field to induce an electron avalanche. An example of such a device, which will be used in tests described later in the thesis, is the so-called Gaseous Electron Multiplier (GEM) [122, 123]. GEMs are a type of Micro-Pattern Gaseous Detector (MPGD) consisting of two conductive layers separated by a dielectric layer, with a regular grid of holes, as shown in Figure 2.13. A high electric field is generated within each hole when a potential difference is applied to the conductive layers. When an electron in the detector gas drifts into the structure, an electron avalanche occurs, resulting in a large number of additional electrons. The ratio between the electrons arriving at the amplification device and the electrons collected is one of the key operating parameters for electron amplification devices, known as *gain*. An important note regarding negative ion drift gases such as SF_6 is that since anions are being drifted instead of electrons, the electrons must be stripped from the anion before they can be amplified. Therefore, higher avalanche fields are required compared to conventional electron drift gases, as the electric field must strip electrons with sufficient energy to cause additional ionisation and prevent re-attachment.

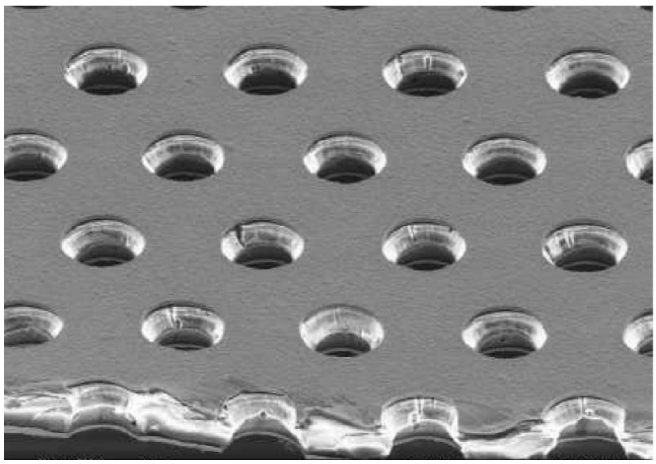

Figure 2.13 Magnified image of the GEM structure [124].

2.3.2 Effect of common pollutants in gas TPCs

In gas TPC operation, there are two types of electrons: primary electrons, which are produced by ionisation from interactions in the gas, and avalanche electrons, which are additional electrons generated by the amplification stage. Common pollutants (O_2, N_2 and H_2O) have high electron affinities, which can readily capture these electrons, resulting in a suppression of gain. This effect has been extensively investigated by many groups. R. Guida et al. conducted a study demonstrating the suppression of gain due to O_2 and N_2 [125]. They controlled the introduction of pollutants O_2 and N_2 in Triple-GEM-based TPC detector containing a target gas mixture of Ar:CO_2:CF_4, and monitored the detector gain. A Triple-GEM detector consist of three GEMs arranged sequentially such that electrons from the drift region passes through and is amplified in each stage, resulting in significantly higher gains. An ^{55}Fe calibration source was used to provide constant ionisation in the gas. The primary electrons generated are amplified by the GEMs and produces a constant detector signal. If no electrons are captured during this process, a constant detector gain is achieved.

Figure 2.14 and Figure 2.15 shows their results in terms of normalised gain as a function of O_2 and N_2 contamination, respectively. It can be seen that deterioration in detector gain was caused by contamination of both pollutants. However, O_2 resulted in 50% gain decrease at a concentration of $\sim 10^3$ ppm, while N_2 only achieved this at a concentration above 10^4 ppm. This may be due to the higher electron affinity of O_2. The non linearity with gain deterioration can be attributed to the complex mechanism by which primary and avalanche electrons are captured. Although a thorough investigation of H_2O contamination in GEM detectors has not yet been conducted, its introduction is expected to capture electrons due to its high electron affinity, suppressing gain with a similar trend as O_2 and N_2.

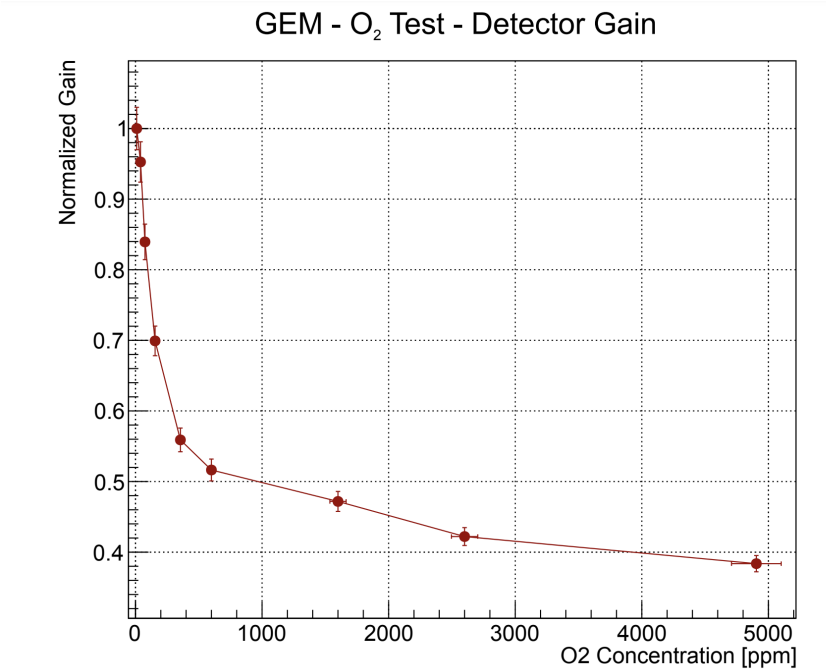

Figure 2.14 Normalised gain as a function of O_2 contamination [125].

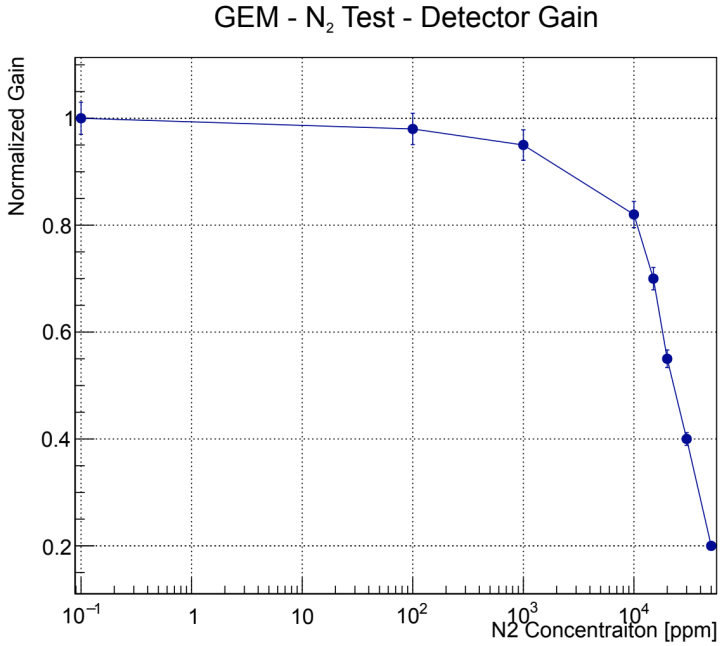

Figure 2.15 Normalised gain as a function of N_2 contamination [125].

2.3.3 Gas purification

The impact of gain deterioration due to common pollutants can be mitigated by the removal of such pollutants. This is typically achieved by the continuous flow of fresh gas or by placing an inline purifying filter in a loop with the gas TPC. Corbetta et al. conducted a demonstration of the removal of common pollutants resulting in the recovery of gain [126]. Figure 2.16 shows a schematic of the setup used, consisting of a GEM detector with associated electronics and DAQ connected in a loop with a purifier module containing molecular sieves. Also on the right of the figure is a supply of fresh target gas mixture used in the experiment Ar, CO_2, and CF_4.

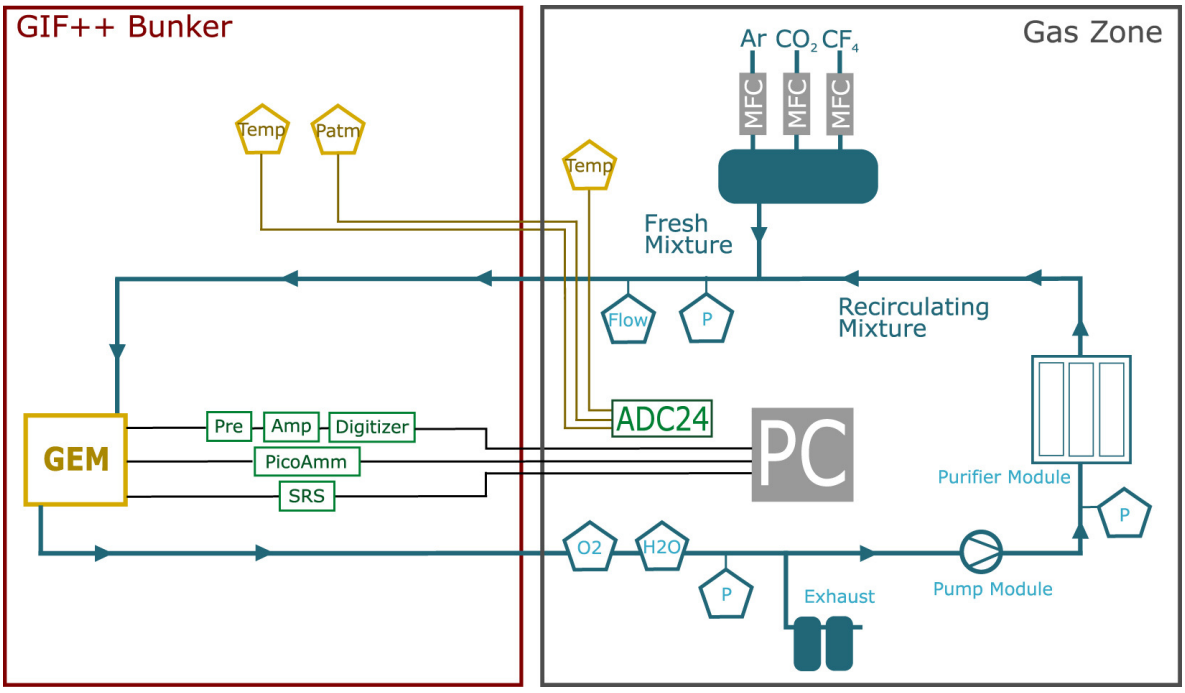

Figure 2.16 Schematic of the experimental setup used to demonstrate gain recovery. The setup consists of a GEM detector with associated electronics and DAQ, connected in a loop with a purifier module containing molecular sieves. On the right of the figure, the supply of fresh target gas mixture is shown, which is controlled by Mass Flow Controllers (MFC) [127].

Figure 2.17 shows the detector's gain during the continuous flow of fresh gas mixture, indicated as open mode, and recirculation at different levels without purifiers and with purifiers. The technique of continuous flow of fresh target gas during open mode purges any common pollutants introduced into the detector setup, resulting in a steady gain level. However, without the introduction of fresh gas and without the purifier engaged, common pollutants start to accumulate, indicated by the increase of O_2 concentration. This results in

a significant decrease in gain. Once the purifier was engaged, O_2 concentration decreased and the gain returned to levels similar to open mode operation.

Many gas-based experiments utilise standard purifier modules containing molecular sieve filters to capture common pollutants [128–130]. Before using these modules, the detector's target gas used must be considered as it may get absorbed by the filters. To determine if molecular sieve filters are applicable to an SF_6-based gas detector, the absorption of SF_6 with all molecular sieve sizes commercially available is tested and described in Section 4.4.

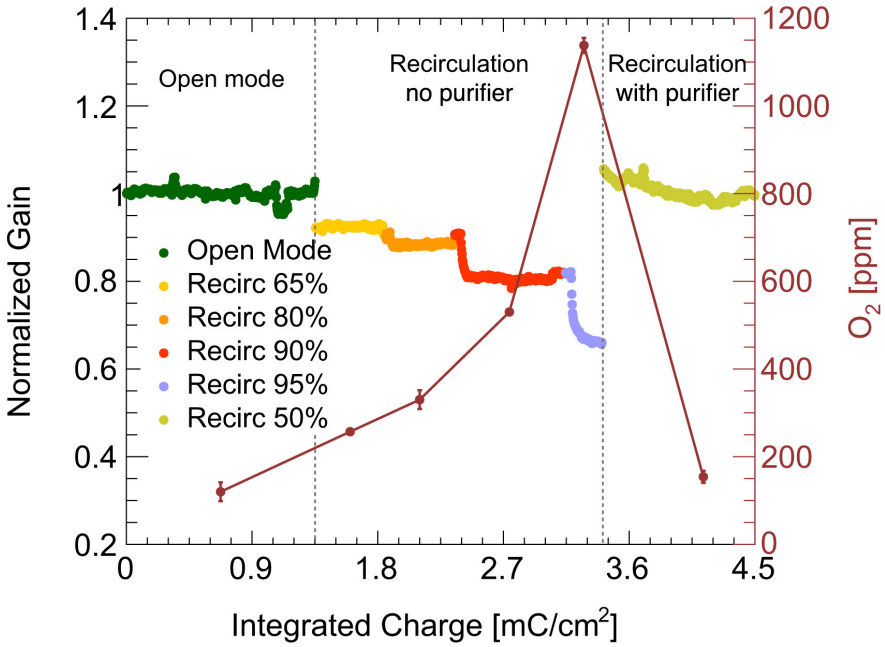

Figure 2.17 Normalised gain as a function of integrated charge during operation and O_2 concentration. *Open* mode corresponds to continuous flow of fresh gas, while *Recirc* percentage corresponds to the amount of gas recirculated [127].

2.4 Conclusions

This chapter explored the effects of radon contamination in dark matter experiments and the impact of common pollutants on gas TPCs operation. Radon contamination provides a source of unwanted background that can mimic genuine signals, which is dealt with through active radon mitigation and signal discrimination. The presence of common pollutants impacts the gain amplification of signals, which is addressed by the removal of such pollutants through gas purification. A solution that is regularly used to address both radon contamination and common pollutants in gas TPCs is the continuous flow of fresh target gas. However, large amounts of target gas are released into the atmosphere as a result of this. As mentioned

in Chapter 1, the novel properties of SF_6 gas have made it an ideal candidate for future directional dark matter experiments. Considering that SF_6 is the most potent gas, an approach that recycles SF_6 and prevents the need for regular gas replacement is required.

A major theme of this thesis is not only to investigate the removal of radon from SF_6 but to investigate the possibility of a system that can simultaneously tackle the issue of common pollutants as well. Although there are readily available filters known to remove common pollutants, filters that actively remove radon from SF_6 have not yet been identified. Therefore, an investigation into using molecular sieve filters to remove radon from SF_6 is the topic of Chapter 4.

As discussed in subsection 2.1.2, electrostatic collection is a popular method to measure radon in the field of rare-event physics. To ensure accurate measurements for radon studies involving different gases including SF_6, it is important to consider the electrostatic collection method's response in different carrier gases. Consequently, the subject of Chapter 3 is a study of electrostatic collection response in different carrier gases.

Chapter 3

Electrostatic radon collection in different gases

In the field of rare-event physics experiments, electrostatic collection (as discussed in Section 2.1) is the most popular method for radon measurements because it can achieve high sensitivities, identify different progeny, and provide continuous measurements. In addition, this method is in principle open to adaptation for use with different carrier gases, making it ideal for R&D work involving the target mixtures used in gas-based experiments. However, the performance of electrostatic collection is influenced by the carrier gas used. Covered in this chapter is preliminary new work aimed at improving the understanding of radon measurements in electrostatic devices when used with non-standard gases. The prime focus here is on operation with the commercially available DURRIDGE RAD7, this is because it is a device used for R&D by many groups involved in rare-event physics experiments [131–133].

In Section 3.1, the effects of different carrier gases on the physics of transport and chemical processes during electrostatic collection are discussed. Section 3.2 contains a description of the work performed to correct the collection efficiency of the DURRIDGE RAD7 when using SF_6, CF_4 and He carrier gases. These gases were selected because they are the most relevant target gases for the directional dark matter collaboration CYGNUS [70].

Since information about the collection efficiency of other carrier gases with the RAD7 would be useful for research and industry purposes, the feasibility of a Monte Carlo simulation of the electrostatic collection method was explored, this is described in Section 3.3. The simulation attempts to model electrostatic collection, transport physics, and chemical processes for different carrier gases.

3.1 Effect of carrier gas on radon collection efficiency

In measurements of radon using the method of electrostatic collection, it is important to realise that detection relies on transport not of the radon itself but of the charged progeny, usually ^{218}Po, through the internal gas, normally air, to a silicon alpha particle detector. It is reasonable to expect that the properties of the internal gas can influence the physics of the transport mechanism and hence potentially the efficiency of radon detection. There are implications from this issue for commercial applications in non-standard gases, such as natural resource exploration where radon tests in hydrocarbons are of interest [134]. However, the focus here is on gases relevant to potential new gas-based directional dark matter experiments, namely SF_6, CF_4 and He. Therefore, the potential impact of these carrier gases on the physics of transport and chemical neutralisation processes during electrostatic collection is discussed in this section.

3.1.1 Physics of charge progeny transport

Figure 3.1 shows a schematic of a typical electrostatic detector chamber used for radon measurements. An electric field is induced by an applied high negative voltage on the chamber walls and the grounded Passivated Implanted Planar Silicon (PIPS) Detector. To successfully measure a radon atom, the radon progeny must travel from the point of generation inside the electrostatic chamber to the active detector surface, depicted by the black line in the figure. However, there are physical mechanisms that can prevent progeny from reaching the active detector surface, in particular, recoil and drift trajectory losses, which are functions of the carrier gas.

Loses in recoil corresponds to events where the radon progeny recoil stopping range after generation is within reach of surfaces that are not the active detector window, such as chamber walls. When ^{222} Rn decays to ^{218}Po, it releases Q value of 5.59 MeV [135]. The alpha particle produced has energy 5.49 MeV leaving ^{218} Po with 0.101 MeV. This kinetic energy causes ^{218}Po to recoil with a range that depends on the carrier gas.

The recoil stopping range for a ^{218}Po atom with an energy of 0.101 MeV in N_2, SF_6, CF_4, and He at normal temperature and pressure is shown in Table 3.1 [136]. The recoil range in N_2, SF_6 and CF_4 are within recoil variation of each other. Whereas, He recoil range is approximately a factor of four longer than the other carrier gases, due to its low density. Therefore, losses due to recoil are expected to be the most significant in He, and at similar lower levels in N_2, SF_6 and CF_4.

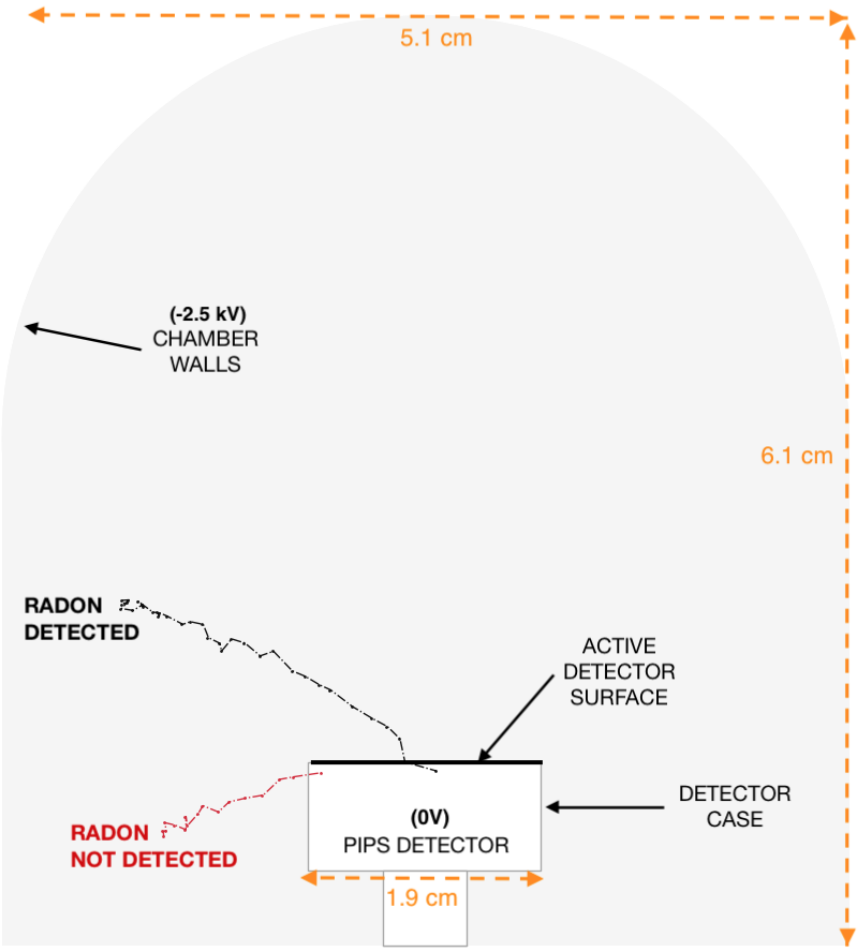

Figure 3.1 Depiction of the electrostatic collection mechanism in a hemispherical cylinder chamber with the dimensions of the chamber and detector shown in orange. The chamber walls are at an applied voltage of -2.5 kV, and the PIPS detector is grounded. The red trajectory represents a radon atom that is not being detected, whereas the black trajectory represents successful collection.

Carrier Gas	Range ($\times 10^{-4}$cm)	Variation ($\times 10^{-4}$cm)
N_2	73	11
SF_6	86	17
CF_4	80	13
He	445	33

Table 3.1 The recoil stopping range for a ^{218}Po atom with an energy of 0.101 MeV. Calculated using SRIM software [136].

Losses in drift trajectory correspond to events where the radon progeny ends at a point that is not on the active detector window, depicted by the red line in Figure 3.1. Radon atoms are randomly distributed in the sample chamber because they are uncharged and not affected by the applied electric field. Therefore, the starting point of the generated radon progeny can be assumed as randomly distributed. For a fixed chamber geometry and constant electric field, the drift trajectory towards the detector will be dictated by the radon progeny ion mobility.

Ion mobility is the ability of an ion to move through a medium in response to an electric field and is unique for the ion-carrier gas combination. The mobility of the ions, μ, is given by

$$\mu = \frac{q}{k_B T} D, \tag{3.1}$$

where q is the charge of the ion, T is the gas temperature, k_B is the Boltzmann constant and D is the diffusion coefficient of the ion in the medium. The diffusion coefficient is given by

$$D = \frac{1}{2} \lambda \nu, \tag{3.2}$$

where the diffusion coefficient, D, is a function of the mean free path, λ, and the root mean square (RMS) velocity of the ion ν. The RMS velocity of an ion is given by

$$\nu = \sqrt{\frac{3 k_B T}{m_{ion}}}, \tag{3.3}$$

where k_B is the Boltzmann constant, T is the gas temperature, and m_{ion} is the mass of the drifting ion. The mean free path, λ, is the average distance two particles travel between collisions and is given by

$$\lambda = \frac{1}{\sigma N}, \tag{3.4}$$

where σ is their collision cross section and N is the number density of the carrier gas. The collision cross section, σ, is defined by

$$\sigma = \pi(r_{ion} + r_{gas})^2, \tag{3.5}$$

here r_{ion} and r_{gas} are the kinetic radius of the ion and the carrier gas atom, respectively. The kinetic radius is defined as the size of the sphere of influence that can lead to a collision. It is unlike atomic radii, which are defined by the size of the electric shell of the atom. The number density of carrier gas, N, is given by

$$N = \frac{\rho N_A}{M_{gas}}, \tag{3.6}$$

where N_A is Avogadro constant, ρ is density of carrier gas and M_{gas} is the carrier gas molar mass. Combining equations above, the ion mobility μ, for a specific ion and carrier gas combination can be calculated using

$$\mu = \frac{qM_{gas}}{2N_A\rho\pi(r_{ion} + r_{gas})^2}\sqrt{\frac{3}{m_{ion}k_BT}}. \tag{3.7}$$

To calculate the mobility, μ, for $^{218}Po^+$ in a specific carrier gas, information about the kinetic radii for both the $^{218}Po^+$, r_{Po}, and carrier gas, r_{gas}, are required. There are published values for the kinetic radii for common gases such as N_2, SF_6, CF_4, and He [137]. However, none for the charged progeny $^{218}Po^+$, which may be due to its rarity and radioactive nature.

The mobility of $^{218}Po^+$ in carrier gas N_2 has been experimentally determined by Chu and Hopke [103]. This measurement can be used to calculate a value for the kinetic radii of $^{218}Po^+$ by using the relationship in Equation 3.7. The experimentally determined mobility of $^{218}Po^+$ ions in carrier gas N_2 at Normal Temperature and Pressure (NTP) conditions (293K, 101325 Pa) is μ =1.87 $cm^2V^{-1}s^{-1}$, which equates to a kinetic radii value of r_{po} =314 pm. This kinetic radius is relatively large compared to single atoms, which can be attributed to its positive charge significantly increasing its sphere of influence.

Using the calculated r_{po} and Equation 3.7, the mobilities for $^{218}Po^+$ in carrier gases N_2, SF_6, CF_4 and He at NTP conditions is shown Table 3.2. These values suggest that in response to an electric field $^{218}Po^+$ moves most efficiently through the carrier gas He, followed by N_2, CF_4, and then SF_6. Electrostatic collection efficiency is anticipated to follow this order, as $^{218}Po^+$ mobility is expected to play a significant role in the collection process.

Carrier Gas	Mobility of $^{218}Po^{+}$ ($cm^2V^{-1}s^{-1}$)
N_2	1.87 [103]
SF_6	1.33
CF_4	1.52
He	2.33

Table 3.2 Extrapolated $^{218}Po^{+}$ mobility in different carrier gases.

3.1.2 Chemical neutralisation processes

There are chemical processes that can neutralise the charged radon progeny during its transport to the detector, resulting in the progeny no longer responding to the electric field. These chemical processes are complicated and depend on the composition of the carrier gas and the presence of any trace gases. There are numerous possible chemical neutralisation mechanisms. However, the most significant, discussed here, are expected to be *small ion recombination*, *electron scavenging*, and *charge transfer*.

Small ion recombination occurs when negative ions and electrons neutralise charge radon progeny. When radon alpha decays it can ionise the carrier gas, generating electrons and positive ion pairs. Depending on the carrier gas, the neutral gas can gain an electron forming negative ions. Negative ion formation is complicated and may include many processes. However, the concentration of negative ions is postulated to be proportional to the radon concentration [138]. The average energy required to create an ion pair in a gas is called the W-value. This parameter may provide an insight into the chemical neutralisation due small ion recombination in different carrier gases. The W-Value for carrier gases N_2, SF_6, CF_4 and He is shown in Table 3.3. He requires the most energy to create an ion pair, followed by N_2, then SF_6, CF_4 have comparable values. Therefore, the impact of small ion recombination is expected to be the most severe with SF_6 and CF_4, and the least with He from the carrier gases considered.

Carrier Gas	W-Values (eV)
N_2	36.6
SF_6	34.0
CF_4	34.4
He	42.7

Table 3.3 The mean energy required to create an ion-pair in the carrier gases considered. W-Values from [139].

The presence of trace gas molecules in the atmosphere, such as H_2O and NO_2, can contaminate the carrier gas. These trace molecules can produce negative radicals as a result of the $^{218}Po^+$ decay. For example, water radiolysis can occur where H_2O molecules to split into reactive free radicals $H\cdot$ and $\cdot OH^-$, as shown by

$$\begin{aligned} H_2O &\rightarrow H\cdot + \cdot OH, \\ \cdot H + e^- &\rightarrow \cdot OH^-, \\ \cdot OH^- + Po^+ &\rightarrow Po + \cdot OH. \end{aligned} \tag{3.8}$$

The positively charged ^{218}Po can scavenge electrons from the negative hydroxyl radical, neutralising the ^{218}Po ion. The electron scavenging chemical process makes the method of electrostatic collection susceptible to humidity. However, if the carrier gases are kept to low humidity this effect should be negligible. In fact commercial devices typically come with dehumidifiers to suppress this effect [98].

$^{218}Po^+$ may become neutralised during a collision with a neutral molecule via a charge transfer process. For this to occur, the colliding molecule must have a lower ionisation potential than the polonium atom. Since polonium has a much lower ionisation potential (8.43 eV) than common carrier gases (12.06 eV for O_2 and 15.58 eV for N_2), this process typically poses no problems. Only in the presence of trace gases such as Volatile Organic Compounds (VOCs) is charge transfer a concern. VOCs are notorious for reducing the collection efficiency of electrostatic detectors when present, as many hydrocarbons have an ionisation potential that is even lower than that of polonium [140]. Table 3.4 shows the ionisation potential for N_2, SF_6, CF_4, and He carrier gases. Since they are all above polonium's ionisation potential (8.43 eV), the charge transfer effect can be disregarded, assuming a pure carrier gas is used.

Carrier Gas	**Ionisation Potential (eV)**
N_2	12.06
SF_6	15.30
CF_4	15.56
He	24.58

Table 3.4 Ionisation Potential for the carrier gases considered. Data from [141].

From the chemical neutralisation processes considered, small ion recombination is likely the most severe. Consequently, the suppression of small ions due to chemical neutralisation during collection is expected to be greatest for SF_6 and CF_4, and the least with He among the carrier gases considered.

3.2 Experimentally measuring radon in different gases

As discussed in Section 3.1, electrostatic collection in different carrier gases consists of complex mechanisms, making it difficult to predict accurate collection efficiencies corrections for specific carrier gases. Therefore, an experimental method was developed to empirically determine the radon collection efficiencies in different carrier gases. The electrostatic detector used for the measurements is the commercially available DURRIDGE RAD7.

3.2.1 Experimental setup and method

The experimental setup shown in Figure 3.2 was constructed to measure electrostatic collection efficiencies in different carrier gases. The setup consists of a 35L gas reservoir that is connected to a contamination loop and a measurement loop, indicated by the red and green arrows, respectively.

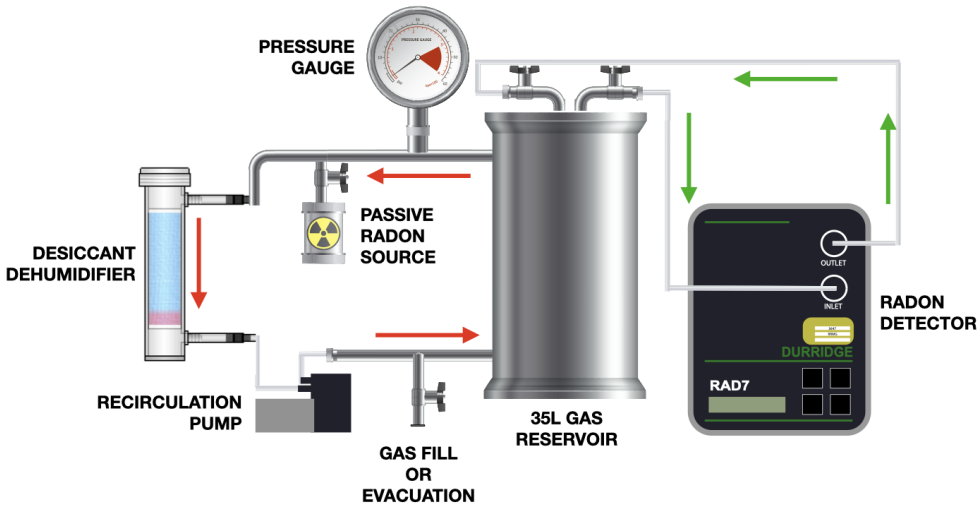

Figure 3.2 Schematic of the experimental setup used to measure radon in different carrier gases.

In the contamination loop, a passive radon source is used to contaminates the gas reservoir with radon, and a desiccant dehumidifier removes any water in the carrier gas that can affect collection efficiency. The gas is driven by a KNF recirculation pump with a gas flow of 3 LPM. In the measurement loop, an electrostatic radon detector measures the activity in the contaminated gas reservoir. The RAD7 was used to measure radon, which has a 1 L electrostatic sample chamber and an internal pump with a nominal flow of 1 LPM.

Before the radon activity in the gas reservoir can be measured, the passive radon source must be given ample time to output a stable activity. The radon source consists of a piece

of ^{226}Ra enclosed in a metal container. For the source to produce a constant radon activity, the generation and decay of ^{222}Rn must reach a steady state, termed secular equilibrium. 99% of the activity at secular equilibrium is reached, after an emanation time of 25 days. Consequently, the gas reservoir was only measured after five weeks of contamination loop operation. To ensure steady state activity was reached, radon in the gas reservoir was monitored for five days with the DURRIDGE RAD7 radon detector.

Measurements of the contaminated gas reservoir were performed in N_2, CF_4, SF_6 and He. The gas replacement was completed by first evacuating the gas reservoir with a vacuum scroll pump for an hour, then the reservoir and RAD7 were purged with air until radon levels returned to ambient levels. After a day, the reservoir was again evacuated with a vacuum scroll pump and was filled with the gas of interest to a pressure of 1.1 bar. The volume of the DURRIDGE RAD7 chamber is not suitable for low pressures, instead of evacuation the RAD7 was purged with the gas of interest for 10 minutes.

3.2.2 Data analysis

Collection efficiency corrections for CF_4, SF_6 and He carrier gases are calculated by comparing their steady state radon activity with the N_2 measurement. The DURRIDGE RAD7 radon detector is calibrated by default in a carrier gas of air, since air is mostly N_2, the measured activity in N_2 is approximated as the true value.

The RAD7 radon detector outputs radon concentration in units of activity per unit volume. An example of RAD7 output using DURRIDGE CAPTURE software is shown in Figure 3.3 [98]. The software is programmed to apply a correction for lost counts due to water neutralisation if the relative humidity is greater than 15% [98]. No correction was required since the humidity in the setup was kept below 3% by the desiccant humidifier.

At high radon concentrations, the RAD7 is limited by its memory so a short measurement cycle time of 15 minutes was used. This short sample time has exacerbated the fluctuation due to the random nature of nuclear decay, resulting in large uncertainties in each data point. Therefore, the 15-minute cycles time were down-sampled to 6 hours cycles, which also provided ample time for the growth of progeny in response to any changes in concentration. Nevertheless, over the 5 days measurement, all data points were within errors of each other, indicating a steady state activity. The average during the last 5 days of measurement is used as the radon concentration at secular equilibrium. To convert radon concentration to activity, this value was multiplied by the total setup volume (36 L).

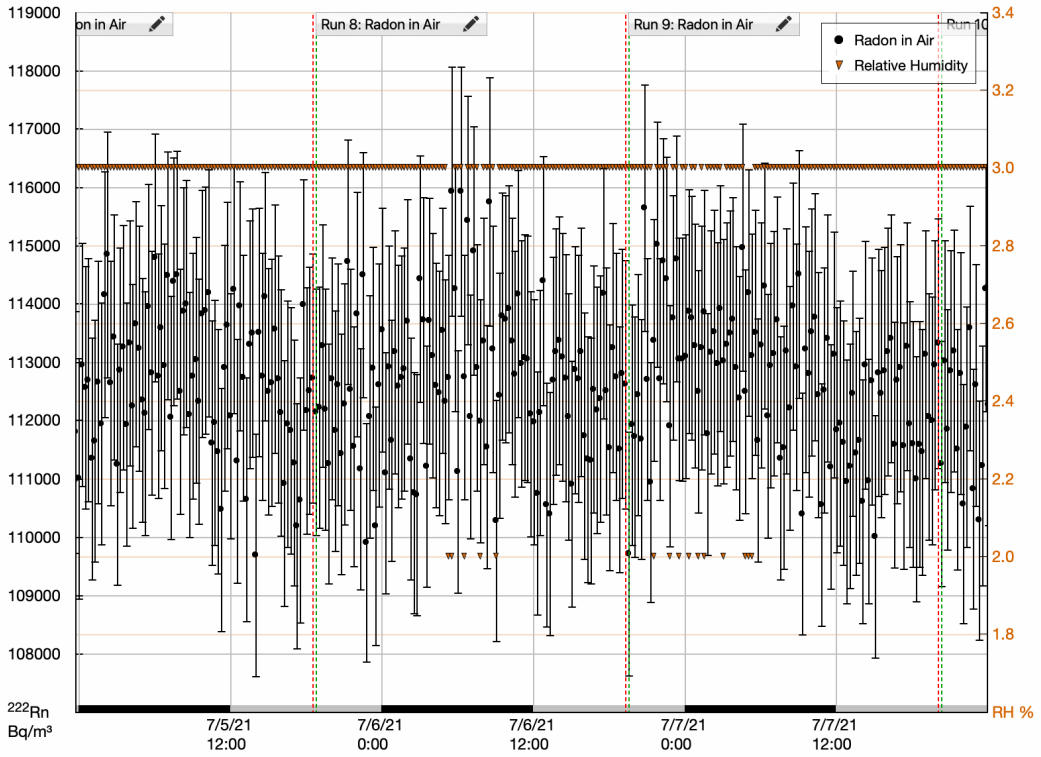

Figure 3.3 An example of a RAD7 measurement data output using the DURRIDGE CAPTURE software, where the black and brown data points correspond to radon concentration and humidity, respectively.

3.2.3 Results and discussion

The radon activity measurement after five weeks of contamination loop operation for N_2, CF_4, SF_6, and He are shown in Figure 3.4. The measurement in N_2 was repeated to ensure the experimental setup was providing repeatable radon activity. The standard deviation of the mean radon activity during the five-day measurement period for each carrier gas did not exceed 0.2%, indicating a steady-state activity was reached.

The secular activity results for N_2, CF_4, SF_6, and He carrier gases is shown in Table 3.5. Since the RAD7 response with N_2 carrier gas is assumed to be the true value, the response of other carrier gases is provided relative to the average of N_2 measurements. Here, the average N_2 value was calculated by summing the results and dividing by the number of repeats, resulting in 4136 ± 4 Bq. The results imply that electrostatic collection with the RAD7 is most efficient with He, 17% more sensitive than standard carrier gas N_2, while CF_4 and SF_6 carrier gases suppress electrostatic collection by 69% compared to N_2. The considered impact of $^{218}Po^+$ mobility and small ion recombination correctly predicted the

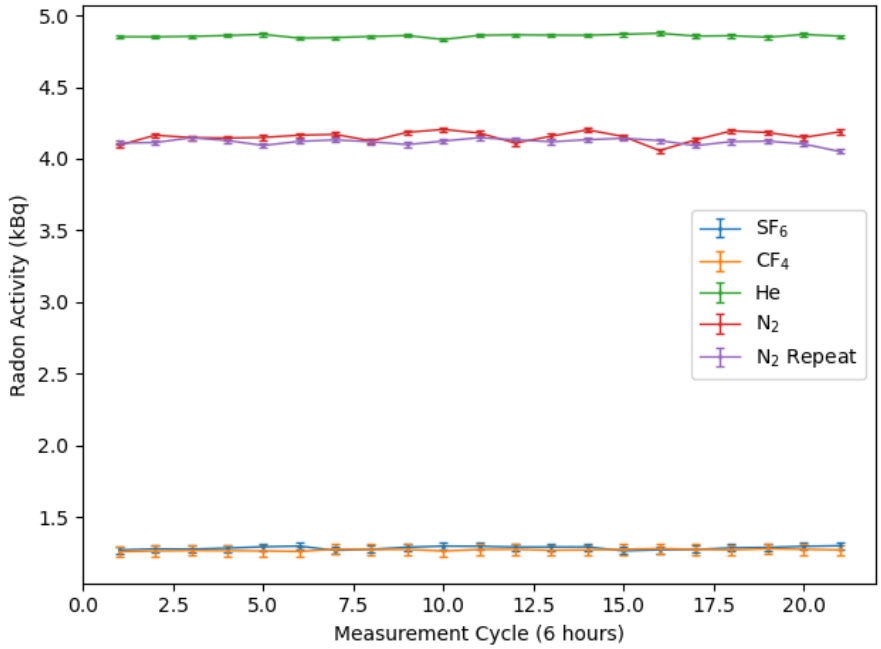

Figure 3.4 Plot of radon activity measurements after five weeks of contamination loop operation.

trend of relative collection efficiency being in the order of He, N_2, SF_6, and CF_4 from most efficient to least efficient. However, the effect of recoil range predicted He to be the most affected, indicating that recoil losses are less significant than the impact of the other mechanisms considered. Any experimental measurements in CF_4, SF_6, and He carrier gases with a standard calibrated RAD7 must be corrected by multiplying the RAD7 output with correctional factors in Table 3.6.

Carrier Gas	**Average Activity (Bq)**	**Relative to N_2 Average**
N_2	4154 ± 8	-
N_2 Repeat	4117 ± 5	-
SF_6	1284 ± 2	0.311 ± 0.001
CF_4	1270 ± 1	0.307 ± 0.001
He	4856 ± 2	1.174 ± 0.001

Table 3.5 Average radon activity during the radon measurement in carrier gases N_2, SF_6, CF_4, and He shown in Figure 3.4. The relative to N_2 average was calculated using 4136 ± 4 Bq.

Carrier Gas	Correctional Factor
SF_6	3.33
CF_4	3.26
He	0.85

Table 3.6 Correction factors to be multiplied to the RAD7 output when measuring in SF_6, CF_4, and He carrier gases.

3.3 Monte Carlo simulation of radon collection in different gases

Information about the collection efficiency in other carrier gases would be useful for research and industry purposes. The experiment carried out in Section 3.2 could be repeated to produce collection efficiency corrections for gases of interest. However, this will require access to different gases and 6 weeks of measurement for each carrier gas. An alternative method is to develop a Monte Carlo simulation of electrostatic collection to determine the detector's response in different carrier gases. There have been simulations of electrostatic collection in the past [142–145], but none have specifically modelled the widely used DURRIDGE RAD7. In addition, many simulations do not account for chemical neutralisation processes, which are known to have a significant impact on collection.

Building in the work covered in Section 3.1 and Section 3.2, this section describes the simulation process used to predict the DURRIDGE RAD7's electrostatic collection response in different carrier gases. The electrostatic collection mechanism inside the RAD7 chamber is discussed in subsection 3.3.1. The electrostatic chamber geometry and electric field were modelled using ANSYS Mechanical v16.1 [146] , detailed in subsection 3.3.2. Code was developed to simulate $^{218}Po^{+}$ transport in the ANSYS field map using Python 3 [147], which incorporating losses during transport and chemical processes, as described in subsection 3.3.3 and subsection 3.3.4, respectively.

3.3.1 Electrostatic collection mechanism

The electrostatic collection with the RAD7 start by sampling the gas of interest into the detector chamber. The gas enters the chamber via a filter to remove any radon progeny already in the sample so that only ^{222}Rn that decays in the chamber is collected. When ^{222}Rn atoms enter the detector chamber, they distribute randomly because they are neutral so are not responsive to the electric field. Once ^{222}Rn alpha decays, it produces a ^{218}Po atom with an energy of 0.101 MeV causing ^{218}Po atom to recoil in a random direction. If the recoil

range is within reach of the detector chamber walls the ^{218}Po is counted as lost. Only 88% of the ^{218}Po atoms produced from ^{222}Rn decay results in a charged $^{218}Po^{+}$. The neutral ^{218}Po species will be counted as lost as they are not responsive to the electric field. A fraction of the positive $^{218}Po^{+}$ ions is subject to neutralisation processes. The fraction affected depends on the composition of the carrier gas and condition such as gas temperature and pressure, as discussed in Section 3.1. The principal neutralisation mechanism in the absence of humidity and trace gases is small ion recombination (see subsection 3.1.2).

If $^{218}Po^{+}$ remains unneutralised, it will continue its trajectory towards the PIPS detector due to the electric field. $^{218}Po^{+}$ is subject to collisions with the carrier gas particle during its flight. The collision causes a small deviation in the $^{218}Po^{+}$'s path toward the PIPS detector.

Finally, if the $^{218}Po^{+}$ lands on the PIPS detector's active surface it is counted as a successful flight. Otherwise, if it lands on the PIPS detector case or the chamber walls it is counted as lost. Note that the actual signal measured by the RAD7 is the alpha decay of the collected ^{218}Po, which has a 50% chance of decaying into the PIPS active surface.

3.3.2 Modelling electrostatic collection chamber E-Field

The electrostatic chamber and PIPS detector inside the RAD7 is shown in Figure 3.5, these were modelled in ANSYS using manufacturer dimensions. The chamber consists of a hemisphere on top of a cylinder. The cylinder has a height of 6.1 cm, and the radius of the cylinder and hemisphere is 5.1 cm. The PIPS detector is placed along the cylinder axis on the flat side and has an active surface area of $\pi(0.973\text{ cm})^2$. The cylindrical symmetry of the electric field chamber can be exploited to simplify the ANSYS electric field calculation from 3D to 2D by using cylindrical coordinates. Therefore, the coordinate system used is the height along the cylindrical axial, h, and the radial distance, r.

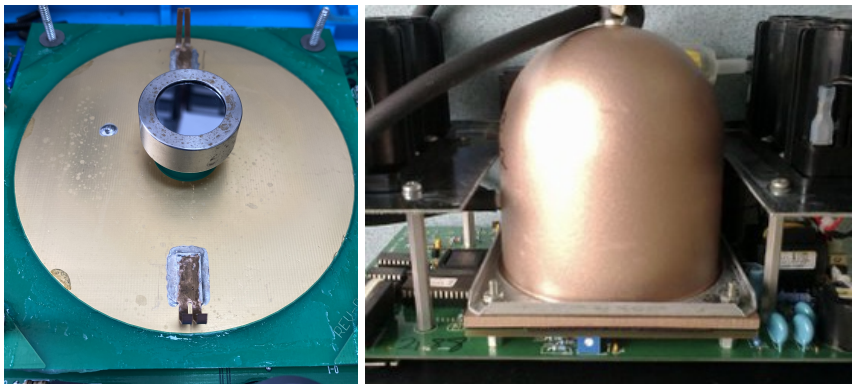

Figure 3.5 Photos of the PIPS detector (left) and the internal chamber (right) in the RAD7.

ANSYS was used to simulate this geometry, which includes input parameters for material attributes and voltages. The walls and PIPS detector were modelled as metal, while the volume inside the chamber was modelled as gas. The chamber walls were set to a high voltage of 2500V, while the PIPS detector was set to 0V. Figure 3.6 shows ANSYS electric field solution, on the left is a contour plot of in units of V/cm, and on the right is a vector direction plot with the uniform arrow lengths. ANSYS generates an output file containing information about the magnitude and direction of the electric field for a mesh of nodes in the chamber. The electric field nodal map will be utilised in the simulation of $^{218}Po^{+}$ drift.

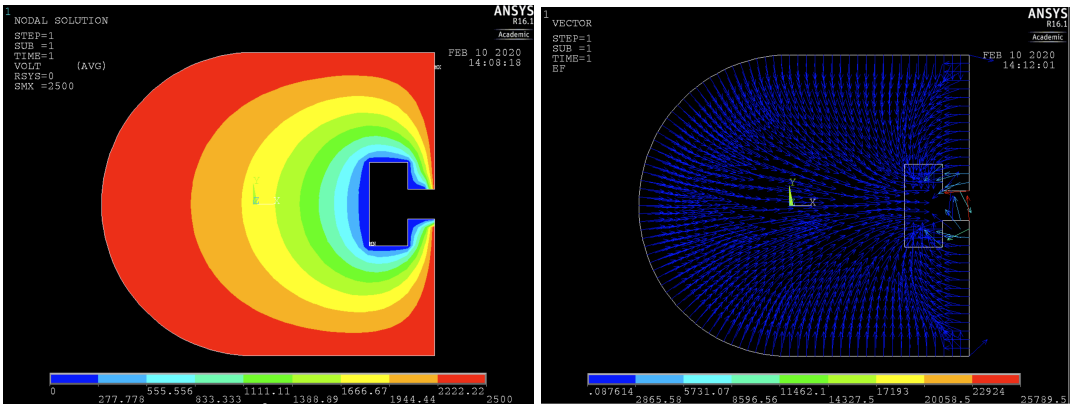

Figure 3.6 Contour plot (left) and vector plot (right) of the ANSYS electric field solution for the RAD7 chamber.

3.3.3 Simulating ^{222}Rn generation and $^{218}Po^{+}$ transport

Now that the RAD7 electric field chamber has been modelled, radon generation inside the chamber and particle tracking of the ^{218}Po ion are simulated using the Python modules *numpy* [148] and *SciPy* [149]. Recoil loses are modelled using the calculated ^{218}Po ion ranges from the SRIM (Stopping and Range of Ions in Matter) simulation package [136].

The simulation starts with the generation of radon position in the chamber. Since radon is uncharged, it is invisible to the electric field in the chamber, therefore will distribute randomly in the chamber volume. To simulate this, the *numpy.random* package is used to generate a random position in the h and r coordinates inside the chamber. However, due to simplifying the 3D volume to 2D cylindrical coordinates, two corrections are made to the generation of random r coordinates. The first is that the r coordinate is a function of h, and is limited as the height of the hemisphere is approached. The second is that the probability density function for generated r must grow with increasing r. This is because a larger r results in a bigger chamber volume, allowing for more possible points in the r coordinate.

Figure 3.7 shows an example of 5000 radon positions generated in the chamber using the radon position generation function developed. In the cylindrical coordinates, radon position generation closer to the cylindrical axis is less likely. However, this is a byproduct of the chosen coordinate system. In fact, in the r-plane (xy-plane in cartesian coordinates), the distribution appears to be random, with equal probability everywhere in the chamber. Furthermore, as the height of the hemisphere is reached, the frequency of positions generated along h also decreases, as expected.

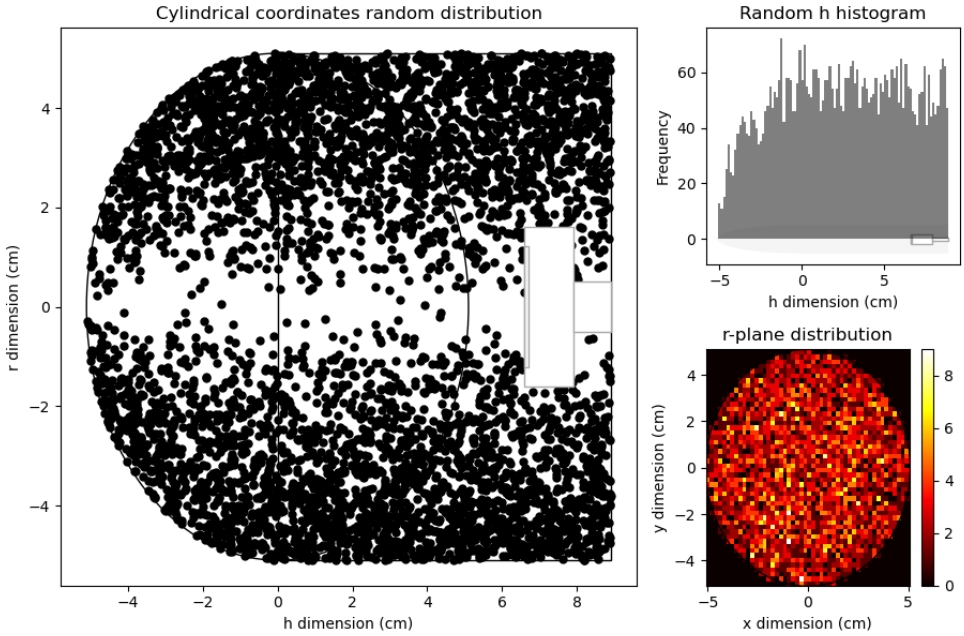

Figure 3.7 Distribution of radon position randomly generated in the electrostatic chamber.

The simulation then models recoil loses during radon decay. Once ^{222}Rn atom is generated in the chamber, it can alpha decay causing the ^{218}Po atom to recoil in a random direction. The recoil range of ^{218}Po depends on the carrier gas species, temperature and pressure, which can be calculated using the SRIM (Stopping and Range of Ions in Matter). Figure 3.8 shows a SRIM simulation for ^{218}Po atom with an energy of 0.101 MeV in He gas at standard temperature and pressure. The SRIM calculation resulted in recoil range of 44.5 $\times 10^{-4}$ cm with a straggle (variance) of 3.3 $\times 10^{-3}$ cm. The recoil range magnitude can be modelled to be normally distributed using the calculated SRIM parameters. A recoil event is simulated by randomly generating a recoil range from this distribution and a random recoil direction in 3-dimensional space. The recoil range magnitude and direction are then converted to r and h components. This change in position is applied to the initial radon position generated. If

the updated position of the produced ^{218}Po is within reach of the detector chamber walls or detector case, it is counted as lost.

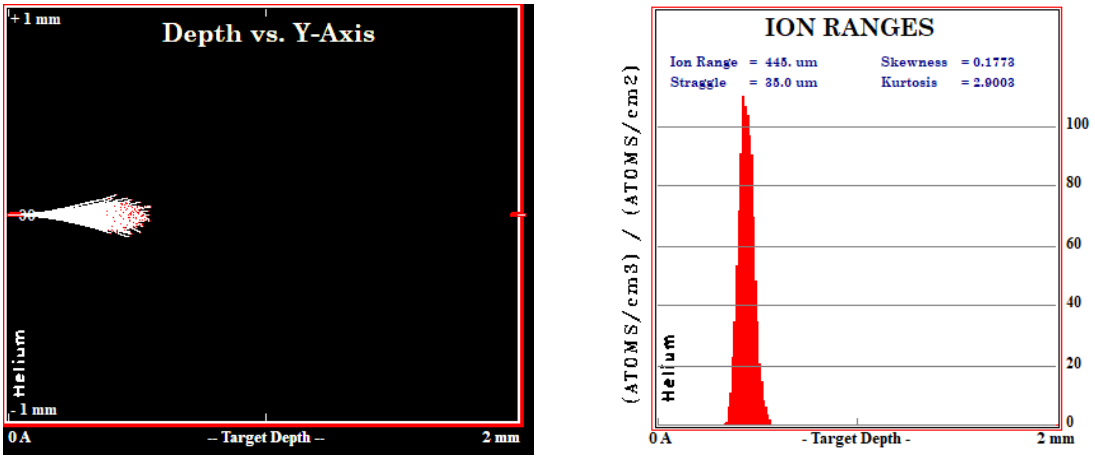

Figure 3.8 SRIM range simulation: left shows ^{218}Po ion traversing He and right shows ion ranges histogram.

A positively charged ^{218}Po atom produced from ^{222}Rn decay will drift towards the PIPS detector due to the electric field in the chamber. However, ^{222}Rn decay only results in 88% of ^{218}Po atoms to be positively charged. Since neutral ^{218}Po atoms are unresponsive to the electric field, they will not be collected. To simulate this, ^{222}Rn decay is defined with a function that has 12% probability of producing a neutral ^{218}Po atom.

If a positively charged ^{218}Po ion is produced, its drift trajectory is simulated by calculating the drift velocity, $v(r,h)$, due to the electric field, $\vec{E}(r,h)$, using

$$v(r,h) = \mu \vec{E}(r,h), \tag{3.9}$$

where μ is the mobility of the ^{218}Po ion for a specific carrier gas. This mobility can be calculated using Equation 3.1, derived in Section 3.1. This is applied to the simulation as follows: when a positive ^{218}Po ion is generated, there will be a corresponding electric field solution to its position, P(r,h). Figure 3.9 demonstrates how the nearest electric field node solution from ANSYS is determined using the *SciPy.Spatial* module. The black dots represents to the nodal electric field solutions, the red dot represents to the current particle position and the blue dot represents to the calculated nearest nodal solution. During a simulation time step dt, the position of a ^{218}Po ion will change due to the drift velocity gained from the local electric field. Updates to the position of ^{218}Po ion due to the velocity gain from the nearest electric field node solution are repeated until an endpoint is reached.

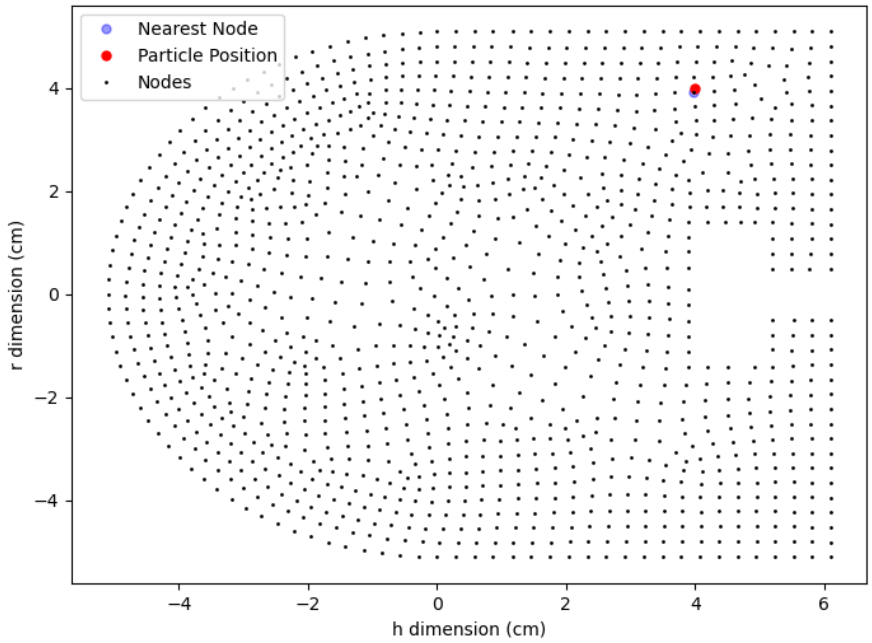

Figure 3.9 Example of the nearest electric field node calculation from current particle position.

Figure 3.10 shows examples of ^{218}Po ion tracking. The black track corresponds to a successful collection, where the ^{218}Po lands on the PIPS detector's active surface. The red track is an example of a trajectory landing on the detector case resulting in the loss of the ion. The sequential dots in each track corresponds to an update of ^{218}Po position in simulation time step dt.

One way ^{218}Po ion's trajectory will be affected during transport is due to collisions with carrier gas particles. The collision causes a small deviation in the ^{218}Po ion's path toward the PIPS detector. The fluctuation in the trajectory is modelled in the simulation using root mean displacement, MSD, given by

$$MSD = 6Ddt, \tag{3.10}$$

where D is the diffusion coefficient of the ^{218}Po ion for a specific carrier gas and dt is the time step. The diffusion coefficient can be calculated from the ion mobility μ, using Equation 3.2. The collision during trajectory is modelled to have a normal distribution, where the current position P(r,h) is the mean and MSD is the deviation during a simulation step dt. By using this distribution, random fluctuation in the position due to collision can be applied to the simulation.

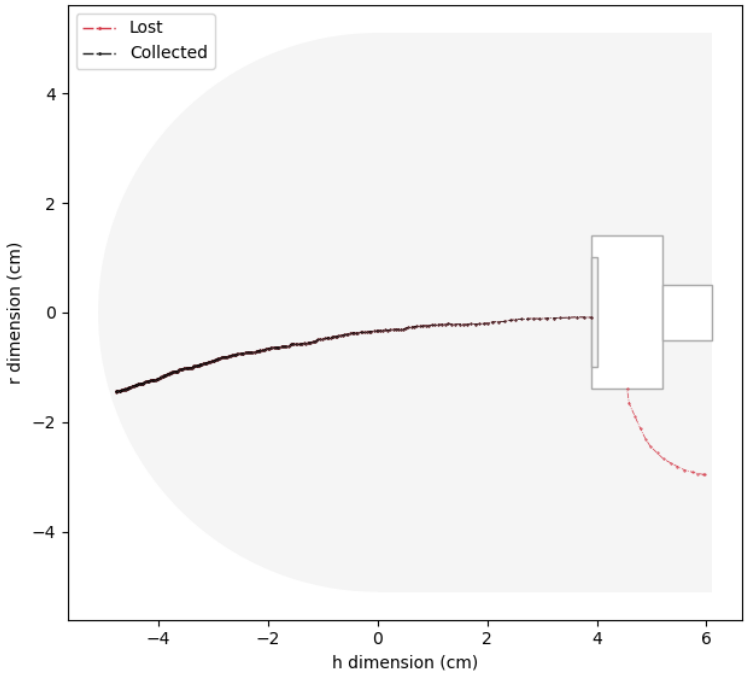

Figure 3.10 Example of particle ^{218}Po ion tracking in the simulation.

Loses due to ^{218}Po decay during flight can be neglected, as the maximum time of flight of ^{218}Po is much smaller than the mean lifetime of ^{218}Po decay. Only ^{218}Po produced in the chamber is collected as the RAD7 uses a filter to stop any radon progeny already present in the gas sample from entering the chamber. Therefore, any ^{218}Po in the chamber will have a mean lifetime of 4.5 minutes. The maximum flight time ^{218}Po in the chamber can be approximated by considering the following: the maximum distance possible between a ^{218}Po and the active surface in the detector is about 10 cm, and the approximate electric field in the chamber is 2500 V/10 cm. Using Equation 3.9, this equates to a maximum flight time of $\sim$ 0.02 seconds in N_2, which is much smaller than the mean lifetime of ^{218}Po.

3.3.4 Simulating chemical neutralisation

The three chemical neutralisation processes commonly considered in the electrostatic collection of radon are: Small Ion Recombination, Electron Scavenging, and Charge Transfer were covered in Section 3.1. These processes are complex and difficult to simulate. However, if the simulation is limited to pure carrier gases i.e. no trace gases are present and in low humidity, neutralisation by Electron Scavenging can be discarded. The same can be done with the Charge Transfer if only carrier gases with ionisation potentials lower than Po atom

are used in the simulation. This leaves Small Ion Recombination as the primary chemical neutralisation process.

According to Gunn, the half-life for neutralisation due to small ion recombination, $t_{1/2}$, of a positively charged ^{218}Po can be estimated using

$$t_{1/2} = \frac{ln(2)\varepsilon_0}{Ne\mu}, \tag{3.11}$$

where N is the number concentration of negative ions (including electrons) in the gas, μ is the mobility of the $^{218}Po^{+}$ in a specific carrier gas, e is the electron charge and ε_0 is the permittivity of free space [150]. The exact relationship between the negative small ion concentration and radon concentration is not known but it is expected to be a function of the energy required to make an ion pair, W-value. Raabe estimated that the half-life for neutralisation due to small ion recombination in an environment with radon concentration of 3700 Bqm^{-3} to be 1.2 seconds [138]. The number of ions, N, that corresponds to this radon concentration can be calculated using Equation 3.11. It was calculated that a radon concentration of 3700 Bqm^{-3} in N_2 carrier gas equates to an ion concentration of 1.3×10^{11} m^{-3}.

Assuming that the negative ions here are produced due to the alpha decay of radon, the number of negative ions, N, can be related to the W-value, W, and radon concentration, C_{rn}, by

$$N = kC_{Rn}\frac{E_\alpha}{W}, \tag{3.12}$$

where E_α is the alpha energy of ^{222}Rn decay (5.49 MeV) and k is a constant related to the complex mechanism of negative ion formation and lifetime at that concentration. Using Raabe's measurement in N_2, a value for k is extrapolated to be 312.5 m^3/Bq.

The small ion recombination process can be applied to the simulation by using Equation 3.11 and Equation 3.12 to estimate the probability of neutralisation during a simulation time dt. Consider a small time step dt where $dt << \tau$, the probability of small ion recombination, p, during time dt is given by

$$p = \frac{dt}{\tau}, \tag{3.13}$$

where τ is the mean life time of ^{218}Po ion given by

$$\tau = \frac{t_{1/2}}{ln(2)}. \tag{3.14}$$

Substituting Equation 3.11 and Equation 3.12, the probability of ^{218}Po ion chemical neutralisation due to small ion recombination for a specific carrier gas and radon concentration is

given by

$$p = \frac{eE_\alpha k}{\varepsilon_0}\frac{C_{Rn}\mu}{W}dt, \tag{3.15}$$

here, e is the elementary charge, E_α is the energy released during alpha decay, k is a calculated constant related to negative ion formation, ε_0 is the permittivity of free space, C_{Rn} is the radon concentration, μ is the ion mobility, W is the energy required to produce an ion pair in the medium, and dt is the time step over which the probability of small ion recombination is calculated. As expected, the probability of neutralisation by small ion recombination is inversely proportional to the W-value, since a higher value indicates that fewer negative ions will be present. Equation 3.15 provides a way to apply small ion recombination chemical neutralisation process in the Monte Carlo simulation.

3.3.5 Simulation results

The input parameters used for the Monte Carlo simulation of radon collection in N_2, SF_6, CF_4 and He carrier gases are shown in Table 3.7. The molar mass, kinetic diameter, and W-value were found in the literature. The electrical mobility and diffusion coefficients were extrapolated from calculations, and recoil ranges were simulated using SRIM.

Carrier Gas	**Molar Mass (g/mol) [141]**	**Kinetic Diameter ($\times 10^{-8}$ cm) [137]**	**Electrical Mobility ($cm^2/(Vs)$)**	**Diffusion Coefficient (cm^2/s)**	**Recoil Range ($\times 10^{-4}$ cm) [136]**	**W Value (eV) [139]**
N_2	28.0	3.64	1.87	0.047	7.3 ± 1.1	36.6
SF_6	146.1	5.5	1.33	0.033	8.6 ± 1.7	34.0
CF_4	88.0	4.7	1.52	0.039	8.0 ± 1.3	34.4
He	4.0	2.6	2.33	0.059	44.5 ± 3.3	42.7

Table 3.7 Simulation input parameters.

A sample simulation of 10,000 radon atoms in carrier gases N_2 is shown in Figure 3.11. The black lines represent $^{218}Po^+$ produced from radon being successfully collected onto the active surface of the PIPS detector, whereas the red lines represent losses due to the geometry of the electrostatic chamber. The yellow line represents the losses due to chemical neutralisation during flight, and the orange dots indicate neutral ^{218}Po species formed from the initial radon decay. Notice that losses due to geometry occur mostly with $^{218}Po^+$ generated near the flat face of the chamber. This is because the path of the $^{218}Po^+$ required to reach the active surface of the detector must be significantly curved, and this curvature is a function of the electric mobility in the carrier gas. The DURRIDGE RAD7 chamber geometry can be

optimised by placing the active area of the detector flush with the flat face of the cylinder or by modifying the chamber geometry so that the electric field funnels into the detector. The Monte Carlo simulation developed provides a method of calculating changes in collection efficiencies due to tweaks in electric fields and chamber geometry. However, this is outside the objectives of this work.

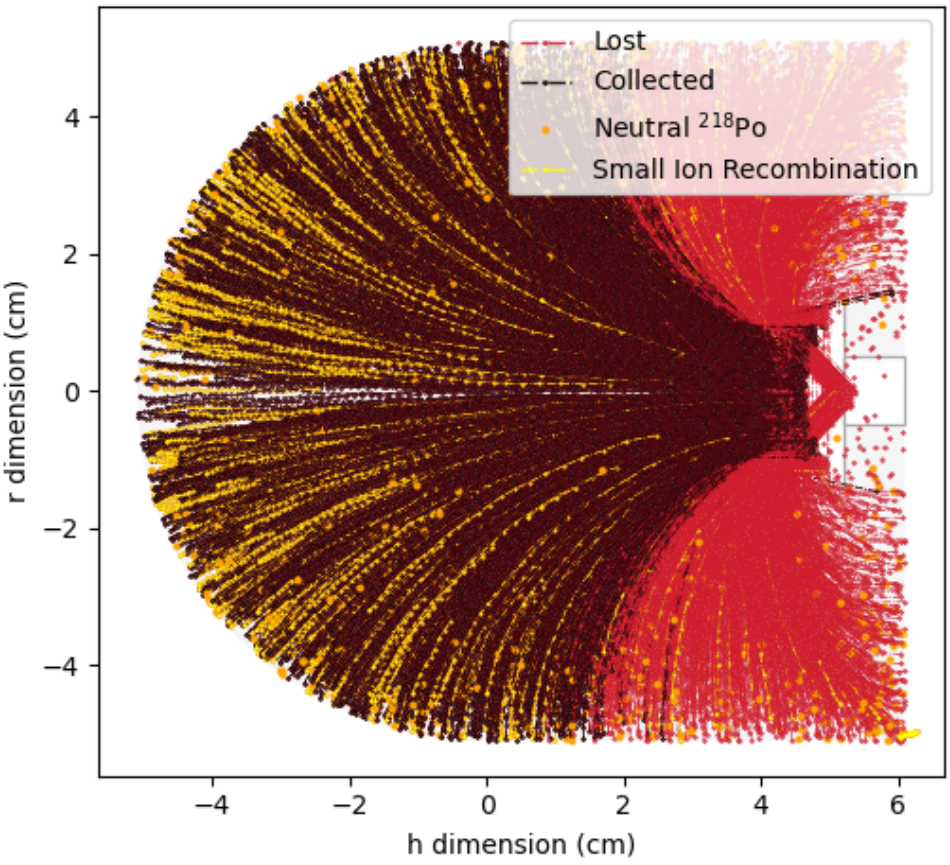

Figure 3.11 Simulation of 10,000 radon nuclei in N_2 carrier gas.

To determine collection efficiencies in different carrier gases, a larger simulation with 100,000 radon atoms was carried out with N_2, SF_6, CF_4 and He. The simulation results for each run are shown in Table 3.8, where time of flight corresponds to the duration that the $^{218}Po^+$ drifts from the time it is generated, the total collected is the number of radon atoms that resulted in $^{218}Po^+$ landing on the active surface of the detector, the total loss is the number of radon atoms not collected due to physical and chemical losses, and collection efficiency is the total collected $^{218}Po^+$ over the total number of radon atoms simulated.

Carrier Gas	Average Time of Flight (ms)	Total Collected	Total Lost	Collection Efficiency
N_2	7.80	42012	57988	0.420
SF_6	10.72	39933	60067	0.399
CF_4	9.38	40580	59420	0.406
He	6.55	44824	55176	0.448

Table 3.8 Summary of simulation results for 100,000 radon atoms.

In Table 3.9, additional information regarding the endpoints of radon atoms lost is provided. Lost to geometry corresponds to radon atoms resulting in $^{218}Po^{+}$ trajectories landing on the chamber walls and non-active part of the PIPS detector. Lost to geometry also includes recoil losses during ^{218}Po generation, but the overall effect of recoil losses were found to be negligible. Lost to neutral ^{218}Po corresponds to neutral species generated from the initial radon decay.

Carrier Gas	Lost to Geometry (%)	Lost to Neutral ^{218}Po (%)	Lost to Small Ion Recombination (%)
N_2	34.2	12.0	11.8
SF_6	35.5	11.8	12.7
CF_4	34.6	12.2	12.6
He	32.3	12.1	10.8

Table 3.9 Details of radon atoms lost. Percentage is of the total number of radon simulated.

3.3.6 Discussion and comparison with experimental results

As can be seen from Table 3.8 He comes out as the most efficient carrier gas, followed by N_2, CF_4, and SF_6. The efficiency of He can be attributed to two factors: the high mobility of $^{218}Po^{+}$ and He high W-value compared to the other carrier gases considered. Due to the high mobility, ions drifts more easily in the electric field, resulting in the least radon loss to geometry. Additionally, the increased mobility led to the shortest average time of flight. The short flight time coupled with the limited amount of negative ions, as a result of He large W_{Value}, means that the chances of small ion recombination neutralising $^{218}Po^{+}$ during flight are reduced. This is highlighted by He simulation result having the smallest percentage lost to small ion recombination. The same argument can be made but for the least efficient carrier gas. The simulation with carrier gas SF_6 resulted in the highest percentage lost to geometry

and small ion recombination, which can be attributed to $^{218}Po^{+}$ low mobility and SF_6 low W-value compared to the other carrier gases considered. Similar characteristics of CF_4 led to a collection efficiency comparable to that of SF_6. The collection efficiency of N_2 falls between that of He and SF_6. The radon lost due to neutral ^{218}Po species for all carrier gases was $\sim 12\%$ as expected.

To provide a fair comparison the experimental and simulation collection efficiency results are given relative to N_2, as shown in Table 3.10. Both the experiment and simulation agree that He is the most efficient carrier gas, followed by N_2. In addition, both methods agree that SF_6 and CF_4 collection efficiencies are very similar, 1.3% and 1.8% of one another, for the experimental and simulated efficiencies respectively. However, comparing the absolute collection efficiencies of the two methods for each carrier gas reveals a significant disparity. For example, assuming that the experimentally determined efficiencies are the true values, the percentage difference of the simulated efficiencies for both CF_4 and SF_6 carrier gases are $\sim 210\%$, and the percentage difference for He carrier gas $\sim 10\%$.

Carrier	**Collection Efficiency Relative to N_2**	
Gas	**Experiment**	**Simulation**
N_2	1	1
SF_6	0.311	0.950
CF_4	0.307	0.967
He	1.174	1.067

Table 3.10 Comparison of experimental and simulation results relative to N_2.

As discussed in subsection 3.1.2 above, the chemical process involved in the transport of large slow moving charged nuclei, like ^{218}Po, through gases, particularly complex ones like SF_6, is complex to model. The discrepancy is therefore most likely due to a missing mechanism not accounted for by the simulation. To correct this, the implications of the discrepancy must first be considered. The greater magnitude of this discrepancy in SF_6 and CF_4 suggests that this missing mechanism has a greater impact on these carrier gases compared to He. Moreover, this mechanism requires significantly suppressing the collection efficiency in SF_6 and CF_4, while slightly increasing the collection efficiency in He. Since the provided results are relative to N_2, the slight increase in He collection efficiency required can equally be achieved by a slight decrease in N_2 collection efficiency. Note that the increase in N_2 collection efficiency necessary to account for the relative collection efficiency of SF_6 and CF_4 will require an efficiency greater than one, which is not possible. Therefore, the mechanism required to correct the discrepancy in the simulation must suppress N_2, SF_6, and, CF_4 efficiencies by different factors.

A mechanism capable of achieving this behaviour is already implemented in the simulation, though more precise modelling may be necessary. The small ion recombination is a process that can neutralise $^{218}Po^{+}$ during flight due to negative ions, including electrons, present. The probability that $^{218}Po^{+}$ is neutralised increases as time of flight and negative ion concentration increases. The required factors of suppression to correct for the discrepancy follows the simulated average time of flight for the carrier gases. In the simulation, the negative ion concentration was estimated by

$$N = kC_{Rn}\frac{E_{\alpha}}{W}, \tag{3.16}$$

where E_{α} is the alpha energy of ^{222}Rn decay (5.49 MeV), W is the average energy required to produce an ion pair in a particular carrier gas, and k is a constant related to the complex mechanism of negative ion formation and lifetime at radon concentration, C_{Rn}. The value for k was extrapolated from a measurement by Raabe in N_2 and was approximated to be constant and applicable to other carrier gases. However, it is likely that the value for k is not the same for all carrier gases. A value of k that accounts for the formation and lifetime of negative ions in the carrier gases considered may account for the discrepancy between the simulation and experiment. Further work is required to model the formation of negative ions for specific carrier gases, possibly relating it to the electron affinity of the carrier gas, which is the energy required to add an electron to an atom or molecule. Another possible parameter is the lifetime of negative ions and free electrons. Implementing these parameters in the simulation may provide the collection suppression required for carrier gases N_2, SF_6, and CF_4 to agree with the experimental results.

3.4 Conclusions

In this chapter, the physical and chemical mechanisms that affect the collection efficiency of electrostatic radon detectors when measuring with different carrier gases were discussed. A method to experimentally determine the collection efficiency of electrostatic radon detectors in different carrier gases was presented. The collection efficiency for a commercial electrostatic radon detector (DURRIDGE RAD7) in SF_6, CF_4, and He carrier gases were determined. It was found that when measuring with a standard calibrated RAD7, a correctional multiplication factor must be applied to the RAD7 data output: $\times$ 3.33 for SF_6, $\times$ 3.26 for CF_4 and $\times$ 0.85 for He. Consequently, this correction factor will be applied to R&D efforts involving RAD7 measurements with carrier SF_6 in Chapter 4, Chapter 5, and Chapter 7.

This chapter also detailed first work on development of a new Monte Carlo simulation of the complex chemical and physical processes around radon detection in an electrostatic type device. This was applied for the first time to the electrostatic chamber inside the RAD7. The simulation included models of physical and chemical mechanisms in order to predict variations in collection efficiencies due to measurements in different carrier gases. The work successfully demonstrated the feasibility of such a Monte Carlo and produced promising initial predictions for He and the similarities experimentally observed in SF_6 and CF_4. However, it is clear that further work is required to model chemical neutralisation, particularly small ion recombination.

An alternative use for the Monte Carlo simulation developed is to calculate changes in collection efficiencies due to tweaks in electric fields and chamber geometry. It was found that the DURRIDGE RAD7 chamber geometry can be optimised by placing the active area of the detector flush with the flat face of the cylinder or by modifying the chamber geometry so that the electric field funnels into the detector.

Chapter 4

Demonstration of radon removal from SF_6 gas using molecular sieves

This chapter is a reproduction of the publication *Demonstration of radon removal from SF_6 using molecular sieves* in the *Journal of Instrumentation* [151]. The author's contributions are detailed in Author's Contribution. Since each publication will have self-contained components there may be overlaps with other chapters. Additional information to the publication is provided at the end of the chapter.

As described in Chapter 2 the gas SF_6 has become of interest as a negative ion drift gas for use in directional dark matter searches. However, as for other targets in such searches, it is important that radon contamination can be removed as this provides a source of unwanted background events. Details of these backgrounds were covered in Chapter 2. The filtration of radon from SF_6 gas using molecular sieves is reported in this chapter. Four types of sieves from Sigma-Aldrich were investigated, namely 3Å , 4Å , 5Å and 13X. First, the molecular sieves that do not adsorb SF_6 gas are described in Section 4.4. Then the molecular sieves types' ability to reduce the radon concentration in contaminated SF_6 gas, was reported in Section 4.5. Finally, in a bid to optimisation adsorption, the molecular sieve was cooled down with a cold trap containing dry ice, discussed in Section 4.6.

4.1 Introduction

Radon contamination is a problem in ultra-sensitive gas rare-event physics experiments such as DRIFT (Directional Recoil Identification From Tracks) [152] because the decay of radon gas inside the detector can be a source of events able to mimic genuine signals. Therefore,

minimising radon concentration in these experiments is important. In DRIFT and other detectors, this is achieved in part by continuous flow and disposal of the target gas.

SF_6 is a candidate to replace current target gas in directional rare-event search experiments due to its novel properties [75]. However, SF_6 is a potent greenhouse gas; for the same mass of gas, SF_6 traps heat nearly 24,000 times more than CO_2 [153]. This makes disposing of SF_6 problematic. One alternative is to introduce continuous recirculation and reuse of the SF_6 gas with active removal of radon using an appropriate filtration process. This is to reduce the radon contamination level of the target SF_6 gas to the required $\sim \mu$Bq l^{-1} range. The source of this radon is the alpha decay of radium-226 in the decay chain of natural Uranium isotopes in the gas and materials of the gas cylinder.

Reported herein is the filtration of radon from SF_6 gas by using molecular sieves. Initially, this was done by determining the types of molecular sieves that do not absorb SF_6. This was followed by an investigation on the ability of the molecular sieve types to reduce the radon concentration in the contaminated SF_6 gas. Finally optimisation of the adsorption by cooling down the molecular sieve in a cold dry ice trap was explored.

4.2 Molecular sieves

Molecular sieves are crystalline metal aluminosilicates structures with specific pore sizes [154]. These pores allow molecules with the critical diameter equal or below the pore size to diffuse and be adsorbed on to the structure; but it allows molecules with diameters larger than the critical diameters to pass between the bead gaps. This process is illustrated in Figure 4.1.

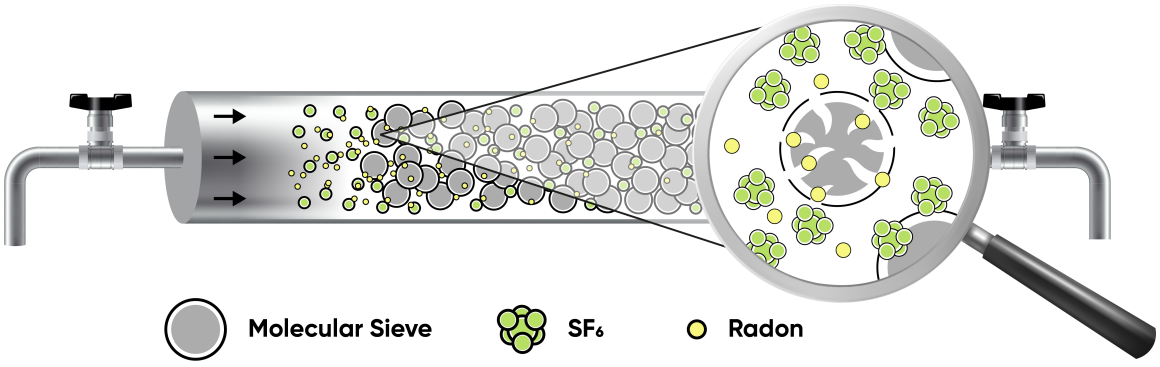

Figure 4.1 Illustration of the separation of smaller radon atom from larger SF_6 molecule using molecular sieves. The arrow represents the flow of the gas inside the molecular sieve vessel.

The range of the diameter of radon is 2.5Å - 4.9Å [155–158] depending on how the diameter is defined. For example, it can be defined as the van de Waal, covalent or Ionic radii. Due to the different definitions, this range of diameter of radon does not necessarily equal the critical diameter appropriate for any of the molecular sieves. Thus, for this work all appropriate available types of molecular sieves were considered; 3Å , 4Å , 5Å and 13X. The number before the Å in the first three named sieves corresponds to the sieve pore size in Å, whereas for the 13X type the pore size is 10 Å.

4.3 Experimental setup

To determine the molecular sieve with the appropriate critical diameter for adsorption of radon from SF_6, the experimental setup shown in Figure 4.2 was used. This comprises a loop of stainless steel pipes allowing SF_6 gas to be circulated through an emanation chamber and the molecular sieve filter. The emanation chamber was used to enhance radon-SF_6 equilibrium. This chamber was attached to a digital and analogue pressure gauge for complementary pressure measurements. Swagelok union tees and quarter turn valves fittings were used to create junctions before and after the molecular sieve filter so it could be engaged and disengage when required. In addition, various inlet and outlet valves were connected throughout the loop.

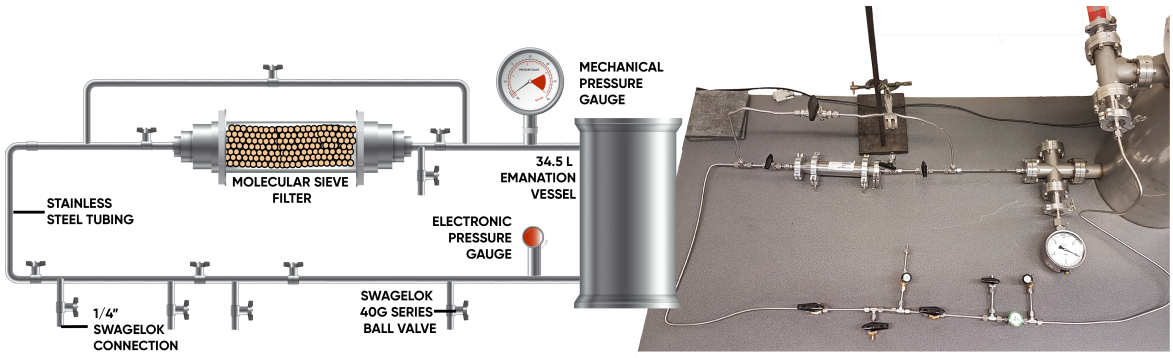

Figure 4.2 A schematic of the constructed system used for calibration of the molecular sieves (left panel). In the right panel is a picture of the constructed calibration setup.

The molecular sieve beads were contained inside a KF-25-FN vessel using KF-25 centering O-ring meshes as shown in Figure 4.3. The vessel holds up to 100g of each type of the molecular sieve beads. Details of the Sigma-Aldrich molecular sieves examined are shown in Table 4.1. The pore size shown corresponds to the size of the cavities in the molecular sieve

structure. An atom or molecule with critical diameter lower than the pore size is trapped within the cavity. The molecular formula arises from the process of synthesising the metal aluminosilicate structure, which heavily depends on the species substituted to create the cavity.

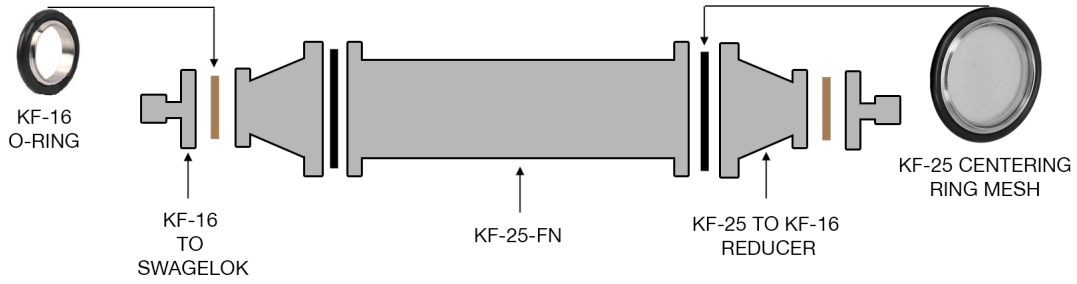

Figure 4.3 Diagram of the molecular sieve filter used with detailed components.

Molecular Sieve	Molecular Formula	Pore Size (Angstroms)	Approx. Bead Size (mm)
3Å	$0.6K_2O \cdot 0.4Na_2O \cdot Al_2O_3$	3	2
4Å	$Na_2O \cdot Al_2O_3 \cdot 2.0SiO_2$	4	2
5Å	$0.80CaO \cdot 0.20Na_2O \cdot Al_2O_3 \cdot SiO_2$	5	4
13X	$Na_2O \cdot Al_2O_3 \cdot 2.8SiO_2$	10	4

Table 4.1 Properties and specifications of the molecular sieves that were examined.

4.4 SF_6 absorption test

Before testing the radon filtration capabilities of the molecular sieves, it was important to verify whether they absorb SF_6 molecules or allow the gas to pass through easily.

4.4.1 Method for testing SF_6 absorption

To test the absorption of SF_6 gas, several components were attached to the constructed testing setup shown in Figure 4.2. As shown in Figure 4.4, these include: a vacuum scroll pump; used for gas circulation and evacuation, a *Drierite* desiccant connected between the gas canister and the setup; used to remove any moisture from the incoming SF_6 gas. The minimum purity of SF_6 gas used in these measurements was 99.9%.

To test whether the molecular sieves absorb SF_6, each of the sieve filters were added to the setup and evacuated with the vacuum scroll pump for an hour. It was then filled

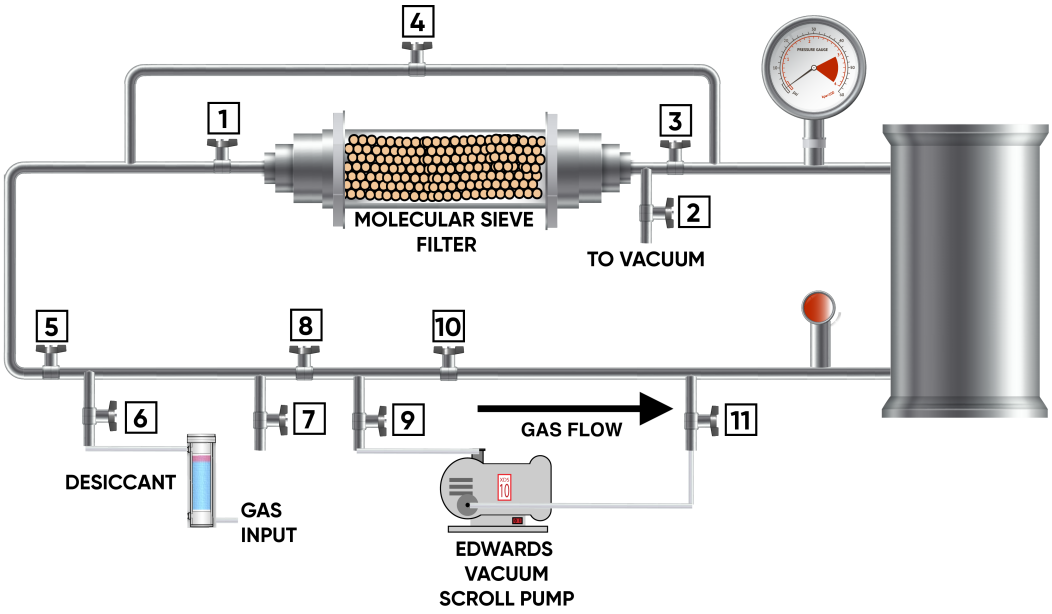

Figure 4.4 Schematic of the position of components required for testing the absorption of SF_6. The valves are labelled with numbers corresponding to those in Table 4.2.

Step	Closed Valves										
	1	2	3	4	5	6	7	8	9	10	11
Evacuation of System						•	•		•		•
Input of Gas	•	•					•		•		•
Initial Equilibrium Pressure Measurement	•	•	•			•	•			•	
Engagement of Filter		•		•		•	•			•	
Pressure Measurement Against Time		•		•		•	•			•	
Changing of Filter	•		•			•	•		•		•

Table 4.2 Steps of the SF_6 absorption test operation and state of the valves. Closed valves are marked with solid black dots, unmarked valves were open in each of the operations. The numbers correspond to the valves in Figure 4.4.

with SF_6 gas via the desiccant up to approximately 40 Torr (typical operational pressure in some directional rare event search experiments). To prevent the absorption of SF_6 before the measurement, one of the filter valves was closed during the filling process, as shown in Table 4.2. Once the gas was filled to the desired pressure, the filter valves were closed and the vacuum scroll pump was used to create a gas current. When a constant pressure was reached, the molecular sieve filter was engaged and the measurement of the setup's pressure against time using the digital pressure gauge was recorded.

To avoid wasting the gas, the same gas was reused for all the other sizes of sieves tested. Sieve replacement was done by closing the appropriate valves and detaching the filter from the system. Before the new filter was reattached and reintroduced to the system, it was evacuated with the vacuum scroll pump to avoid contamination of the gas.

4.4.2 SF_6 absorption results and discussion

The pressure change of the system as a function of time for the 13X, 3Å, 4Å and 5Å molecular sieves are shown in Figure 4.5. For the 13X molecular sieve, it can be seen that the pressure of the system decreased significantly once the filter was engaged. Pressure measurements were recorded until the sieves were saturated. It was found that after 35 minutes there was a total pressure decrease of 6.92 $\pm$ 0.02 Torr. Conversely, no significant pressure variation was observed when the 3Å , 4Å and 5Å molecular sieve types were used.

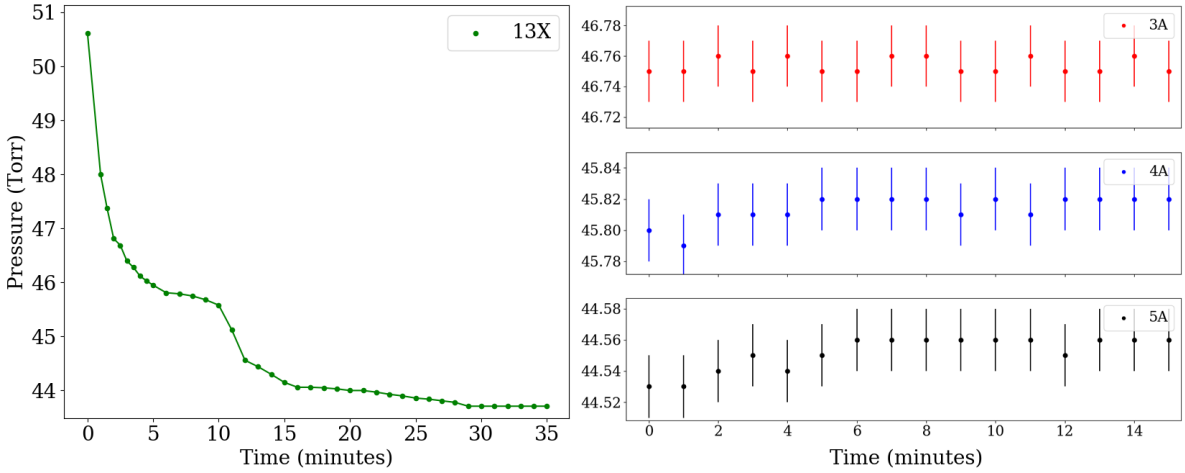

Figure 4.5 The pressure of the system as a function of time for 13X, 3A, 4A and 5A molecular sieves filters. The filters were engaged at time zero for each individual measurement. The errors for the pressure measurement is $\pm$ 0.02 Torr; too small to be seen in the 13X graph scale.

The significant pressure decrease in the 13X molecular sieve filter test indicates that the sieve absorbs SF_6 gas. Therefore, this sieve was not used for further radon filtration tests. This result was expected as the technical information provided by Sigma-Aldrich suggest that the major application of 13X type sieves are with long chain hydrocarbons [154], whereas SF_6 is an unchained simple molecule.

The absence of a significant pressure change in the 3Å, 4Å and 5Å molecular sieves indicates that the SF_6 gas is not significantly absorbed. This implies that the critical diameter

of SF_6 is bigger than 5Å pore size, hence bigger than the pore sizes for 4Å and 3Å types. Therefore, the radon filtration capabilities of the 3Å, 4Å and 5Å molecular sieves can be tested with confidence that the SF_6 gas will pass through the molecular sieve filter. Additionally, from these tests, limits to the SF_6 critical diameter has been determined to be between 5 - 10 Å.

4.5 Radon filtration test

Having established that the 3Å, 4Å and 5Å sieves do not absorb the background gas SF_6, the capabilities of each of the sieves to filter radon from the gas were investigated.

4.5.1 Method for testing filtration of radon

To test the ability of molecular sieves to filter radon from SF_6 gas samples, a passive 5.361 kBq radon gas source from Pylon electronics Inc and a RAD7 radon detector [98] was added to the setup as shown in Figure 4.6. The source contains a radioactive dry ^{226}Ra, which decays into radon gas in an aluminium canister. Using this radon gas, each of the SF_6 samples was contaminated for 1 hour by passive diffusion. The RAD7 detector has an internal pump (of rate 1 litre per minute), which was used to create both the required gas current and to measure the radon concentration in the gas over time.

The radon filtration tests were done as follows; the setup was first evacuated using a vacuum scroll pump for an hour and then filled with SF_6 gas via the desiccant to 1.1 bar, the operational pressure of the RAD7 detector. With the valves connecting the system to the filter closed, the internal air pump in the RAD7 was switched on to create the required gas current through the radon source, so the gas becomes contaminated. The contamination process was done for an hour. After the contamination of the gas, the RAD7 was set to test for a total of 48 hours, with a measurement recorded every hour. The first 24 hours was used to measure the initial concentration of radon. The filter was then engaged for the remaining 24 hours to measure the effect of the filter on the concentration of radon. The corresponding valves to close for each step of the test are shown in Table 4.3. The same set of gas was used throughout the measurements to avoid gas wastage. This led to different initial radon contamination concentration, depending on the amount of decay recorded before the subsequent experiments.

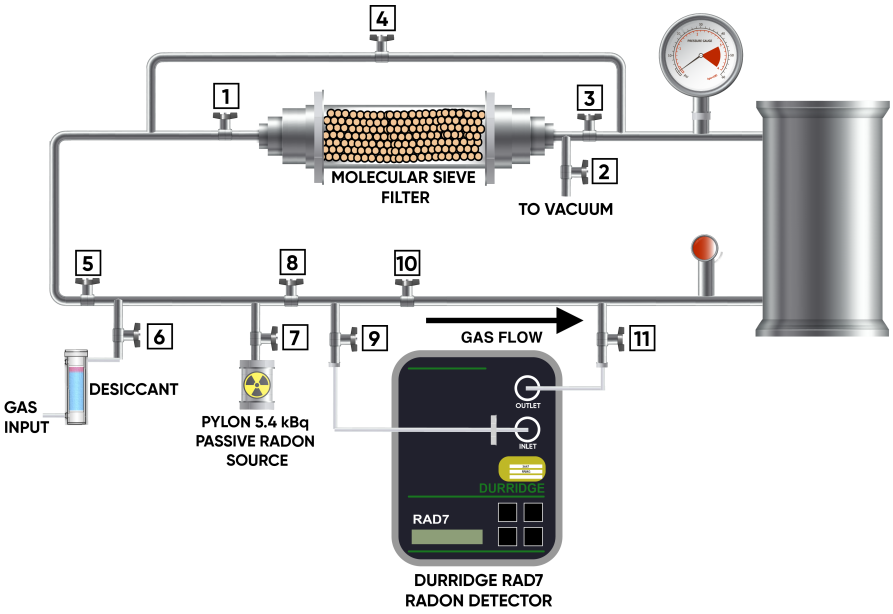

Figure 4.6 Schematic of the components used for the radon filtration from SF_6 tests. The valves are labelled with numbers corresponding to those in Table 4.3.

Step	Closed Valves										
	1	2	3	4	5	6	7	8	9	10	11
Evacuation of System						•	•		•		•
Input of Gas		•					•		•		•
Radon Contamination	•	•	•			•				•	
Initial Concentration Measurement	•	•	•			•	•			•	
Engagement of Filter		•		•		•	•			•	
Filter Concentration Measurement		•		•		•	•			•	
Changing of Filter	•		•			•	•		•		•

Table 4.3 Steps of the radon filtration test operation and state of the valves. Closed valves are marked with solid black dots, unmarked valves were open in each of the operations. The numbers correspond to the valves in Figure 4.6.

4.5.2 Data analysis

The data recorded by the RAD7 include the number of decays per unit volume over time and relative humidity of the sample. Before the data was analysed, various corrections were required. This includes the use of the decay equation to model the recorded data. To do this,

the initial radon concentration parameter was used to compare the effect of the molecular sieve filters to the absolute radon concentration.

Corrections:

- *Humidity:* The ^{222}Rn atom decays into a positively charged ^{218}Po ion [159]. The RAD7 uses this ^{218}Po ion to measure the radon concentration. This is done in the internal hemisphere sample cell inside the detector, which has an electric field to drive the ^{218}Po ion towards the detector [98]. High humidity can be an issue because the slightly negative oxygen in water can attract the ^{218}Po ion. A build up of water molecules around the ^{218}Po ion can lead to the ion becoming neutralised hence preventing the ion from being detected inside the RAD7. Therefore, Equation 4.1, a correction for high humidity provided by DURRIDGE, was applied [98].

$$C_c = C_m \times \frac{100}{116.67 - 1.1 \times RH}, \tag{4.1}$$

  where C_c is the corrected radon concentration, C_m is the measured radon concentration and RH is the relative humidity percentage for the RAD7 detector. This correction was applied to data points with relative humidity > 15%. Overall, the average humidity for this measurement is 8%. This is mainly due to the remnant humidity and expected minuscule leak of the setup.

- *Radon mixing time:* The radon gas contaminate requires sufficient time to distribute evenly throughout the system. This is because during the contamination process, some parts of the system may be more radon rich than others. This effect was evident in the data set, as there was visible discontinuity between the data points before and after the mix. Therefore, the unmixed data were disregarded accordingly.

Fitting Data to the Decay Equation. The decay relation shown in Equation 4.2 was used to create a non-linear regression fit to the data. [160].

$$N(t) = N_0 e^{-\lambda t}, \tag{4.2}$$

where $N(t)$ is the radon concentration at time t, N_0 is the initial radon concentration and λ is the radon decay constant; calculated by using ^{222}Rn half life of 3.8229 ± 0.00027 days The data before and after the filter was engaged are considered separately. The sample size for the non-linear regression fit to the *filter on* data is adjusted until the discrepancy between the data and the decay equation is minimised. This is because the fit to the decay equation only

applies when the filter is no longer active, for instance, when a new equilibrium is reached or the filter is saturated. The initial radon concentration was extrapolated from the best fit for both *filter on* and *filter off* data and used to compare the effective concentration change of radon caused by the engagement of the molecular sieve filter.

4.5.3 Radon filtration results and discussion

Results for the first radon filtration tests are shown in Figure 4.7, Figure 4.8 and Table 4.4. In these plots, the data points shown in red and green correspond to the measurements recorded in the first and second 24 hours of the test, when the filters were not engaged and engaged, respectively. Furthermore, the best fit to the decay equation are shown with a dotted and a solid line for the *filter off* and *filter on* data, respectively.

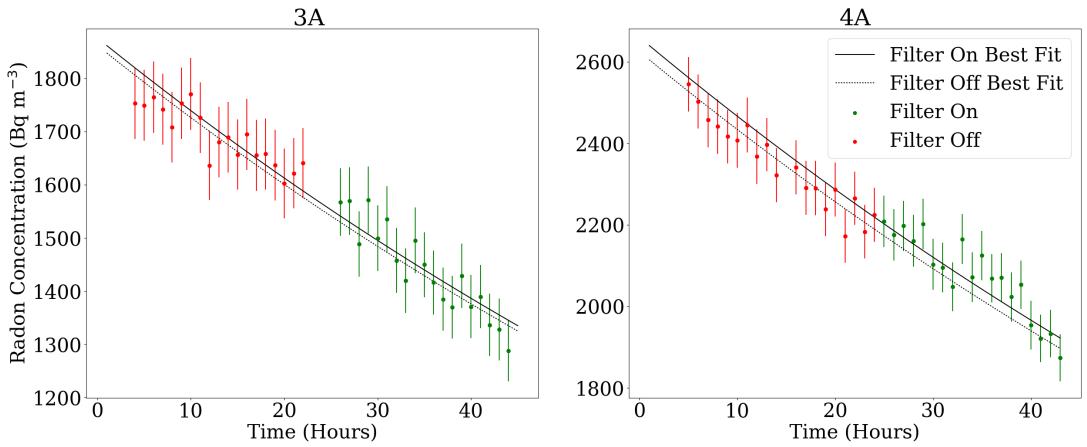

Figure 4.7 Radon concentration against time for the 3Å (left) and 4Å (right) molecular sieve filter tests, where the filter was engaged at 24 hours.

Molecular Sieve	**Extrapolated N_0 (Bqm^{-3})**		
	Filter Off Data	**Filter On Data**	**On and Off Data**
3A	1863.2 ± 9.1	1875.6 ± 9.1	1868.4 ± 6.9
4A	2625.0 ± 11.1	2657.2 ± 11.0	2638.7 ± 11.1

Table 4.4 Results from the extrapolated initial radon concentration parameter. The *filter on*, *filter off* and the combined *On and Off* data corresponds to the data points used when extrapolating the initial radon concentration.

For the 3Å molecular sieve test, it can be seen in Figure 4.7 that the radon concentration decay rate appears not to change when the 3A filter was engaged. This is also true for the 4Å molecular sieve test, as shown in Figure 4.7.The absolute change in concentration of radon caused by introducing the filter is determined by using the extrapolated initial radon concentration N_0. In Table 4.4, for both the 3Å and 4Å filters, the extrapolated initial radon concentration N_0 for the *filter on* and *filter off* data are statistically consistent with theoretical predictions for the considered time window. This shows that the initial decay equation was obeyed even when the filter was engaged, making it evident that the engagement of the 3Å or 4Å filter has no overall effect on the concentration of radon.

The inability of the 3Å and 4Å molecular sieves in removing radon from SF_6 can be explained by the expected critical diameter of noble gases. For instance, the critical diameter of helium (argon) is 2Å (3.8Å) [154]. The location of these noble gases in the periodic table are in the first and the third row, respectively. Whereas, radon is in the sixth row of the noble gas group. By considering the trend of atomic radii down a group, it is expected that the radon radii should be bigger than that of argon. Hence, it is expected that the critical diameter of radon is greater than the pores in the 3Å and 4Å molecular sieve filters.

Results for the 5Å filter are shown in figure 4.8. Here the decay rate is seen to significantly decrease after 24 hours. This time corresponds to when the gas was redirected through the 5Å molecular sieve filter. This shows that the filter absorbs radon from SF_6. A period of time after the significant drop in concentration, it appears that the rate of decay returns to obeying the decay rate equation.

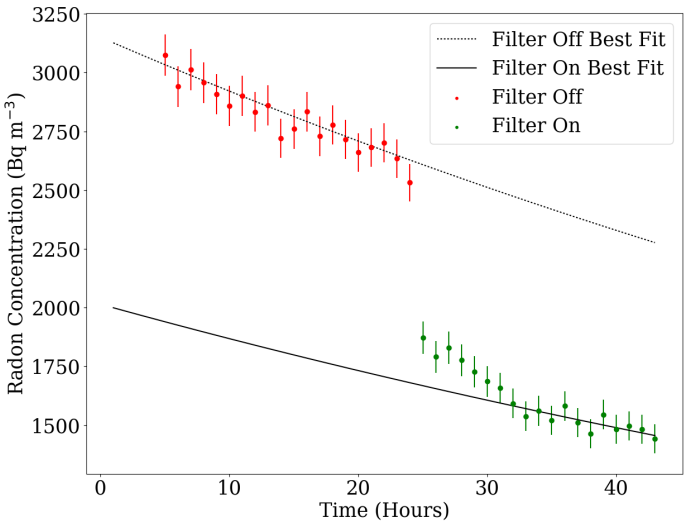

Figure 4.8 Radon concentration against time for the 5A molecular sieve filter. The filter was engaged at 24 hours.

To provide the best fit to the *filter on* data the first 8 hours of data after the filter was engaged were not included to the decay equation fit. The extrapolated initial radon concentration for the *filter off* and *filter on* data is 3150 $\pm$ 28 Bq m^{-3} and 2014 $\pm$ 11 Bq m^{-3}, respectively. This results in a total initial radon concentration reduction of 36%. The results show that it takes approximately 4 hours for the sieve to reach equilibrium with radon. It is expected that the rate of radon absorption in the molecular sieve can be affected by the operational pressure and flow rate of the gas [161], so these are not upper limit results.

4.6 Absorption optimisation by using a cold trap

The behaviour of the absorption plot for the 5Å molecular sieve seen in Figure 4.8 indicates that the filter saturates with time. The number of radon atoms absorbed can easily be shown to be far smaller than the available number of pore holes. So a more likely possibility is that an equilibrium situation is reached in which as many radon atoms are released as are absorbed. A possible means to confirm this, and potentially increase the absorption, is to cool the radon sieve filter in an attempt to reduce the release of radon.

4.6.1 Application of cold trap

The setup for testing the effect of cooling on the radon reduction capabilities of the 5Å molecular sieve follows from the setup and procedure in Section 4.5. A small modification to the setup was made as shown in Figure 4.9; the stainless steel pipes between the molecular sieve and valve of the filter were extended to allow the filter to be placed inside a cold trap. Dry ice was used in the cold trap instead of liquid nitrogen as there was a concern about the O-ring's ability to operate at such low temperature. In this mode, the internal pump of the RAD7 radon detector was arranged such that the cold SF_6 flowed through the large emanation chamber before the radon concentration measurements. This was to ensure that the gas was within the RAD7 operating temperature.

The total RAD7 testing time was extended to 50 hours. The first 20 hours was used to measure the initial radon concentration. After this, the molecular sieve filter was engaged and for the following 24 hours it was allowed to establish an equilibrium between adsorption and desorption of radon. For the remaining 6 hours the dry ice was added to the cold trap.

4.6.2 Cold trap results and discussion

Results from the cooling test are shown in Figure 4.10. The analysis of the radon filtration data was performed using the same corrections and process to fit the decay as discussed in

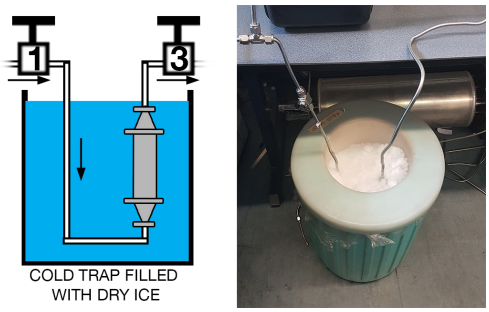

Figure 4.9 Schematic of the radon filtration setup in a cold trap and a photograph of the cold trap during a test.

Section 4.5. In the radon concentration plot in Figure 4.10, there are 3 sets of data points shown in red, green and blue. These data points correspond to when the filter was off, on and when the cold trap was engaged, respectively. There are also 3 radon decay equation fits; the *filter off* best fit and *filter on* best fit were computed using a non-linear regression model for the corresponding data. Whereas, the decay fit for the *lowest data point* only used one data point to extrapolate the lowest initial radon concentration achieved by the 5Å molecular sieve with the cold trap.

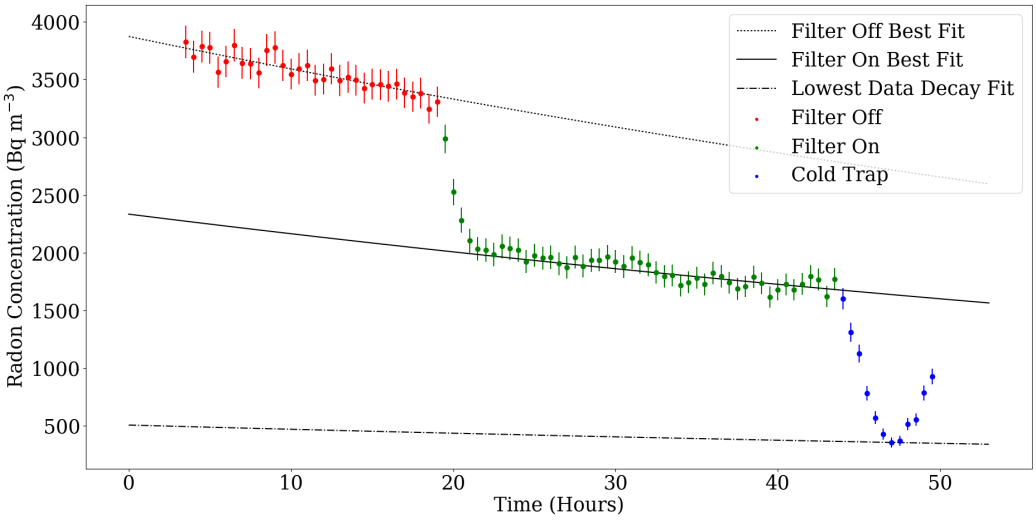

Figure 4.10 Radon concentration in SF_6 shown over time for the 5Å molecular sieve filter. The filter was engaged after 20 hours and the cold trap was engaged after 44 hours. The decay fit on the blue data set was determined using only one data point to extrapolate the lowest possible radon concentration achieved.

As shown in Figure 4.10, the initial radon concentration was reduced by the 5Å filter and a new radon concentration equilibrium was reached as expected. Once the cold trap was introduced there was a further reduction in the concentration. This can be seen in the deviation of the cold trap data from the *filter on* best fit. The lowest radon concentration was reached after 4 hours of introducing the cold trap. The increase in the radon concentration after this point is due to a gradual rise in temperature as the dry ice started to evaporate.

The extrapolated initial radon concentration for the decay fits are shown in Table 4.5. This allows for comparison of the effective radon reduction of the 5Å molecular sieve filter and the 5Å molecular sieve filter with the cold trap. Results show that the application of the 5Å molecular sieve with the cold trap reduced the initial radon concentration by a total of 87%.

Data	**Extrapolated N_0 (Bq m^{-3})**	**Total Radon Concentration Reduction**
Filter Off	3874.8 ± 13.1	-
Filter On	2356.9 ± 10.0	40%
Cold Trap Lowest	504.6	87%

Table 4.5 A table of the extrapolated initial radon concentration parameter. The total radon concentration reduction is the percentage reduction with respect to the initial radon contamination concentration.

4.7 Conclusions

In this work four types of molecular sieves, 3Å, 4Å, 5Å and 13X from Sigma-Aldrich, were used to investigate the radon absorption capabilities from SF_6 gas. It was found that the 13X type absorbed SF_6 molecules, whereas the 3Å, 4Å and 5Å types did not. The 5Å molecular sieve was the only molecular sieve type that successfully reduced the radon concentration. This achieved a reduction in radon concentration from 3150 ± 28 Bq m^{-3} to 2014 ± 11 Bq m^{-3} which is approximately 36.1% of the initial radon concentration in the contaminated SF_6. It was found that the molecular sieves were not saturated by the radon atoms, and so the 5Å radon reduction capabilities were further optimised by applying a cold trap containing dry ice. The combination of the 5Å molecular sieve and a cold trap resulted in reduction of the radon concentration to approximately 87.0% of the initial radon concentration.

The ability of the 5Å molecular sieve filter with a cold trap to significantly reduce radon concentration from SF_6 provides a promising foundation for the construction of a radon filtration set up for future ultra-sensitive SF_6 gas rare-event physics experiments. The set-up

used is not optimised and there is expected to be large scope to improve the factor reduction, for instance by increasing the operational pressure, the flow rate of the gas, and optimising macroscopic properties of the molecular sieve. It should also be noted that depending on the purity of the starting materials and method of synthesis used by the manufacturer, the 5Å molecular sieve structure could potentially be a source of low-level radon radioactivity. In commercial production, the screening of raw materials for radioactive content is not necessary. Therefore, the intrinsic radon emanation of the Sigma-Aldrich molecular sieves are investigated in Chapter 5 and low radioactive molecular sieves candidates are explored.

4.8 Additional information

This section supplements the published article with additional information, and does not contradict the original publication. An update on radon measurements conducted in this chapter, using the SF_6 calibration factor determined in Chapter 3 is provided in subsection 4.8.1. Although the absolute values change, there is no overall effect on the outcome of the results since the same factor is applied to all measurements. The removal of common pollutants from SF_6 is discussed in subsection 4.8.2, which is important for the work conducted in Chapter 7.

4.8.1 RAD7 calibration for SF_6

The DURRIDGE RAD7 is not calibrated to measure in carrier gas SF_6. As described in Chapter 3, a calibration factor for the RAD7 was determined to account for changes in the collection efficiency due to the carrier gas SF_6. For a DURRIDGE calibrated RAD7, it was determined that the output must be multiplied by 3.33 to account for the carrier gas SF_6. This calibration factor is applied to the radon reduction results for 3Å and 4Å shown in Table 4.6, and 5Å shown in Table 4.7. Since the same calibration factor is applied to all the measurements there is no overall effect on the outcome of the results. 3Å and 4Å do not remove radon, and 5Å removed radon from SF_6 by up to 87% of the initial radon concentration.

Molecular Sieve	**Extrapolated** N_0 ($\mathrm{Bqm^{-3}}$)		
	Filter Off Data	**Filter On Data**	**On and Off Data**
3A	6204 ± 30	6246 ± 30	6222 ± 23
4A	8741 ± 37	8848 ± 37	8787 ± 37

Table 4.6 3Å and 4Å results from Table 4.4 with RAD7 SF_6 calibration factor applied.

Data	Extrapolated N_0 (Bq m^{-3})	Total Radon Concentration Reduction
Filter Off	12903 ± 44	-
Filter On	7848 ± 33	40%
Cold Trap Lowest	1680	87%

Table 4.7 5Å results from Table 4.5 with RAD7 SF_6 calibration factor applied.

4.8.2 Note on removal of common pollutants

The effects of common pollutants in gas TPC detectors were described in Section 2.3. Common pollutants such as O_2, H_2O and N_2 are introduced by material outgassing and mini-leaks. The presence of such pollutants influences the detector's gas amplification performance. The removal of these common pollutants with molecular sieves has been demonstrated to restore gas amplification performance in target mixtures using Ar, CO_2 and CF_4 [162].

The molecular sieves types 3Å and 4Å are known to capture O_2, H_2O and N_2. The demonstration of molecular sieve types 3Å and 4Å not to absorb SF_6, shows that removal of common pollutants from SF_6 without absorbing the target gas is possible. Therefore, a gas system employing molecular sieves types 3Å, 4Å and, 5Å that can remove both common pollutants and radon simultaneously is feasible. Development of this gas system is the subject of Chapter 6 and Chapter 7.

Chapter 5

Low radioactive molecular sieves

This chapter is a reproduction of the publication *Testing low radioactive molecular sieves for radon removal from SF_6* in the *Journal of Instrumentation* [163]. The author's contributions are detailed in Author's Contribution. Since each publication will have self-contained components there may be overlaps with other chapters. A new low radioactive MS candidate (NU MS-V2) has been developed since the publication of the paper, and the results are provided at the end of the chapter.

The demonstration of radon removal from SF_6 gas using molecular sieves, detailed in Chapter 4, was a significant advance towards a radon filtration system [151]. Unfortunately, commercial molecular sieves intrinsically emanate radon at levels unsuitable for ultra-sensitive rare-event physics experiments. A method to produce low radioactive molecular sieves was developed at Nihon University (NU) and may provide a suitable candidate for use in a radon filtration setup for such experiments. This chapter covers work undertaken to investigate the feasibility of a 5Å type NU-developed molecular sieve for application to radon filtration setups. This was done by calculating a parameter indicating the amount of radon intrinsically emanated by the MS per unit radon captured from SF_6 gas, detailed in Section 5.3 and Section 5.4. The examination of the new MS candidate (NU MS-V2) follows the method outlined in this chapter and is reported in subsection 5.8.2.

5.1 Introduction

Minimisation of radon contamination is essential in ultra-sensitive gas rare-event physics experiments including directional dark matter experiments [71, 104]. The decay of radon gas in these experiments can produce unwanted background events, able to mimic genuine signals. Radon contamination comes primarily from detector materials. These materials can contain a trace amount of ^{238}U due to inevitable material contamination. The radon gas is

produced in the ^{238}U decay chain. Radon contamination levels are dependent on the size of the experiment. For instance, the radon contamination in the NEWAGE experiment, a small 23 x 28 x 30 cm^3 direction dark matter detector, was measured to be 0.2 mBq [164]. Whereas, in the larger DRIFT experiment, a 1.5 x 1.5 x 1.5 m^3 gas-based direction dark matter detector, was measured to be 372±66 mBq [152]. The increase in contamination levels is due to the additional amount of material. Therefore for large-scale plans, radon contamination levels will inevitably be higher. The radon background goal for future large-scale experiments, such as CYGNUS-1000 [70], which utilises a 1000 m^3 detector, is less than $\sim$ 1 mBq. Many gas rare-event physics experiments manage radon contamination with continuous flow and disposal of the target gas.

The gas SF_6 has been identified as a target gas for use in future directional dark matter searches [75]. However, SF_6 is the most potent greenhouse gas, making the method of continuous flow and disposal problematic [77]. Furthermore, climate change initiatives, such as the EU F-Gas directive, heavily regulate the use of SF_6 and aim to reduce total use fivefold by 2030, compared with levels in 2014 [165]. This restriction creates a hurdle for ultra-sensitive SF_6-based rare-event physics experiments, particularly for large-scale plans such as CYGNUS-1000. Therefore, an alternative method to minimise radon contamination must be implemented for future SF_6 based experiments, where the gas is reused and recycled.

The demonstration of radon removal from SF_6 gas in Chapter 4 was a significant advance towards a radon filtration system[151]. In principle, the SF_6 gas can be continuously recirculated and reused by filtration with the 5Å type molecular sieve, reducing the total amount of SF_6 used. In the past, activated charcoal have been studied for radon filtration [118, 166]. However, molecular sieves offer superior gas selectivity due to their specific pore sizes [167].

Unfortunately, commercial molecular sieves intrinsically emanate radon at levels unsuitable for ultra-sensitive rare-event physics experiments. Commercially available sieves are primarily used in the petroleum industry, where having low radioactive content is not essential, so the manufacturer does not need to screen materials for radioactive content in production. Therefore, it can be assumed that any commercially manufactured molecular sieves will not meet the required low radioactivity level.

Recently, a method to produce low radioactive molecular sieves was developed in Nihon University. A 5Å type Nihon University developed molecular sieve may provide a suitable candidate for use in a radon filtration setup for ultra-sensitive SF_6 gas based rare-event physics experiments. This chapter covers work undertake to investigate the feasibility of a 5Å type NU-developed molecular sieve for use in a radon filtration setup for ultra-sensitive SF_6 gas based experiments. This was conducted by measuring the radon emanated from the NU-

developed molecular sieve and its radon capture efficiency from SF_6. These measurements were compared with the commercial, Sigma-Aldrich manufactured, molecular sieve used in the original radon filtration demonstration in Chapter 4 [151].

5.2 Intrinsic molecular sieve radioactivity

Molecular Sieves (MS) are chemical structures with specific pore sizes. Molecules with a critical diameter equal or smaller than the pore size will diffuse into the pores and be captured. Whereas, molecules with diameters larger than the pore size will not be captured. Instead, the larger molecules will pass between molecular sieve gaps, as shown in Figure 5.1.

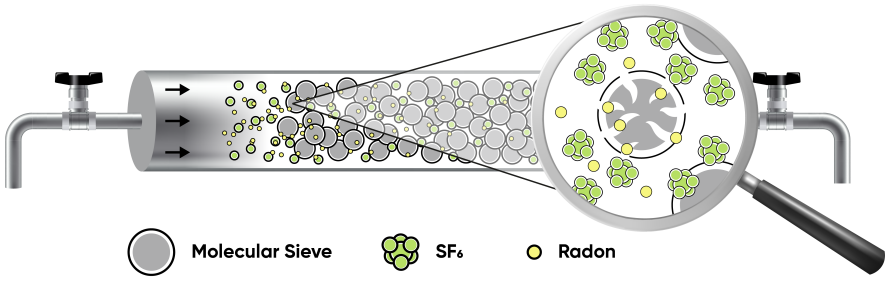

Figure 5.1 Illustration of the separation of smaller radon atom from larger SF_6 molecules using molecular sieves. The arrows represent the direction of flow of the gas inside the molecular sieve vessel. Note that this figure is identical to Figure 4.1 and is included here for convenience and following the reproduction of paper [163].

The sizes of the pores are controlled by using different size cations in the ion exchange processes during production. In the 5Å type molecular sieve, the cation used is calcium. The chemical formula for the 5Å type is shown in Equation 5.1 [154].

$$0.80\,\mathrm{CaO}\cdot 0.20\cdot \mathrm{Na_2O}\cdot \mathrm{Al_2O_3}\cdot 2.0\,\mathrm{SiO_2}\cdot x\,\mathrm{H_2O}. \tag{5.1}$$

The source of radioactive contamination in molecular sieves is from the raw materials used in production, mainly the metallic components. In commercial production, the screening of raw materials for radioactive content is not necessary. H.Ogawa *et al.,* from Nihon University in collaboration with Union showa K.K, has developed a method of producing low radioactive molecular sieves by extensive material selection and screening of raw materials used. The 5Å type NU-developed MS was made by exchanging calcium ions with the low-radioactive 4Å type MS mentioned in [168] [1]. In Figure 5.2, the MS samples used in our comparison are

[1] Low radioactive 3Å type molecular sieves can be synthesised using a similar method [169]

shown. On the left is the 5Å type NU-developed, in the form of white irregular granules with approximate size of 1-2 cm. On the right is the 5Å type MS manufactured by Sigma-Aldrich in uniform beige beads with 8-12 mm diameter.

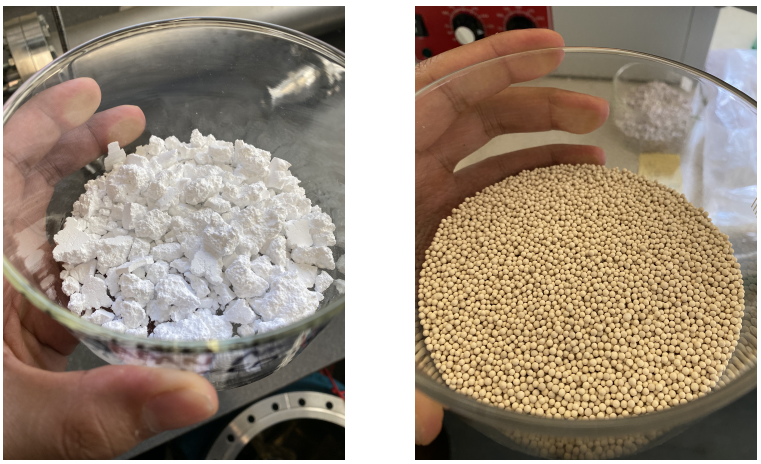

Figure 5.2 Images of the 5Å type molecular sieves tested. The NU-developed MS is on the left and Sigma-Aldrich MS on the right.

When choosing a suitable molecular sieve for a radon filtration system, it is important to understand how radon behaves in a sealed chamber. A gas-based detector is fundamentally a sealed gas chamber with various materials which can emanate radon. Once the chamber is sealed, the radon concentration inside the vessel increases continuously until a steady-state is reached. This is when the production rate of radon is equal to the decay rate of radon, termed secular equilibrium.

The steady-state radon concentration can be considered as the maximum radon activity in the chamber, applying a molecular sieve filter reduces this maximum. The determining mechanism now is the equilibration between the amount of radon captured by the MS and the amount of radon intrinsically emanated by the MS.

To determine the suitability of a MS candidate, both the amount of radon intrinsically emanated from the sieve and its radon capturing efficiency must be measured. The ideal MS has a minimal intrinsic emanation and an optimal capturing efficiency.

5.3 Radon emanation test

Radon is a gaseous element produced in both the ^{238}U and ^{232}Th decay chains. Most materials contain a trace amount of ^{238}U and ^{232}Th due to inevitable material contamination, which is exacerbated by their extremely long half-lives. When radon is produced within a material, due to its gaseous nature, it can escape and emanate into its surroundings. The

radon isotope ^{222}Rn, produced from the ^{238}U decay chain, is the most problematic isotope for contamination because ^{222}Rn has a half-life of 3.8 days, meaning it has the ample time to reach the material surface and travel within the detector before decaying. In contrast, the second most abundant radon isotope, ^{220}Rn, produced from the ^{232}Th decay chain, has a half-life of 55 seconds. Hence, tests reported here focused on measurements from emanation of the ^{222}Rn isotope.

5.3.1 Experimental setup and method

The radon emanation test for the molecular sieves were performed using the experimental setup shown in Figure 5.3. The setup consist of a 3.5L stainless steel emanation chamber in a loop with two DURRIDGE RAD7 radon detectors. The RAD7 collects radon by electrostatic precipitation, measuring alpha decays from radon progeny such as ^{218}Po and ^{214}Po [98]. The loop includes a tee connection where either an EDWARDS vacuum scroll pump or an input of low-humidity low-activity nitrogen gas was connected. The MS of interest was enclosed inside the *Molecular Sieve Container* with meshed O-rings to stop any small fragments escaping from the vessel during evacuation.

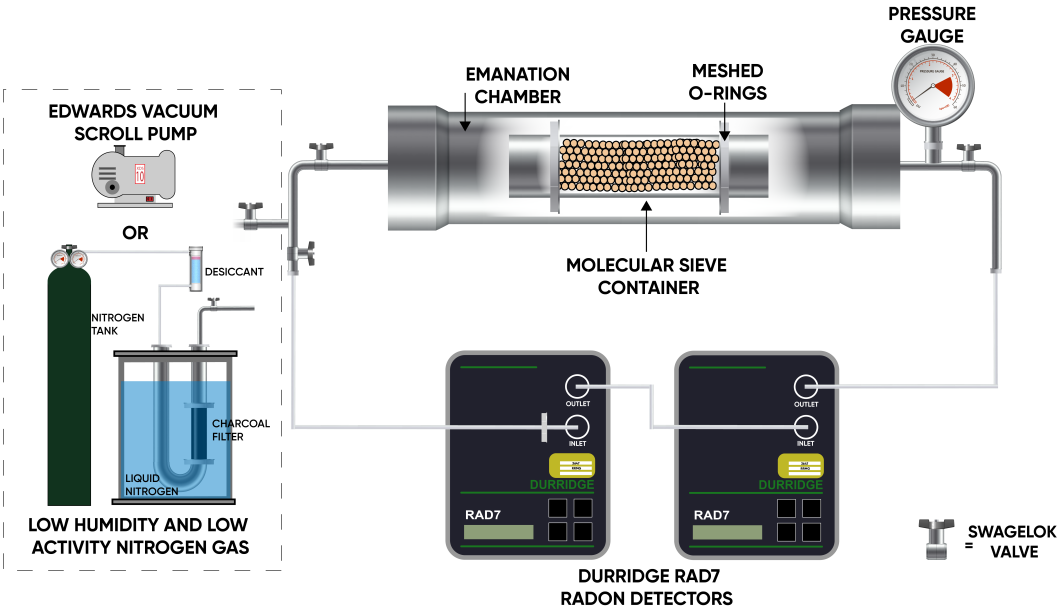

Figure 5.3 Schematic of the setup used for the radon emanation tests.

The emanation testing procedure started with two rounds of 1-hour gas evacuations using the EDWARDS pump. The first evacuation was to get the emanation chamber into sub-torr pressures, inducing outgassing from materials. Since the initial outgassing was expected to be dominated by the emanation chamber, the gas was evacuated again after an outgassing

period of 48 hours. After the second gas evacuation, the MS was left to emanate into the vacuum for seven days.
On completion of the emanation period, the chamber was backfilled with nitrogen gas. It was essential to use low activity-low humidity nitrogen gas to backfill the chamber. Low activity nitrogen gas was required to minimise the introduction of any 'new' radon to the system. Low-humid gas was required because increased humidity can suppress radon counts measured by the RAD7. Low humidity-low activity gas was achieved by flowing the nitrogen through a desiccant, which removes water molecules, and a charcoal filter cold trap, which removes any radon introduced by the nitrogen tank. Once the chamber was backfilled to 760 torr, the RAD7 detectors were purged with nitrogen for 5 minutes to remove any potential residue inside the detector. Finally, the RAD7 with its internal pump on, recorded radon concentration every four hours for a 48-hour measurement period.

5.3.2 Data analysis

The total radon emanating from the molecular sieves and setup is equal to the radon activity at secular equilibrium. For ^{222}Rn to reach secular equilibrium, an emanation time in the order of a month is required. However, in our molecular sieves emanation testing, the samples were only left to emanate for seven days. To compensate for the shorter emanation time, Equation 5.2, which describes the accumulation of radon in a closed system as a function of emanation time was fitted to the measured data.

$$A_m = A_s \times (1 - \exp(-t/\tau)), \tag{5.2}$$

here A_m is the measured radon activity, A_s is the radon activity at secular equilibrium, t is the emanation time and τ is the lifetime of ^{222}Rn. Before the raw concentration data was fitted to Equation 5.2, the radon concentration (Bq/m^3) was converted to radon activity (Bq). This was achieved by multiplying the radon concentration by the total volume in the emanation measurement loop. The total volume is given by Equation 5.3. Where V_{EC} is the volume of the emanation chamber (3.5 L), V_{R7} is the volume of the RAD7 (0.9 L) and V_{MS} is the volume of the molecular sieve container including the volume occupied by the molecular sieve sample (0.15 L).

$$V_T = V_{EC} + 2 \times V_{R7} - V_{MS}. \tag{5.3}$$

A correction to ensure there was ample radon mixing time in the measurement loop for radon to distribute evenly, was also applied. This was done by disregarding the first cycle of the RAD7 data. The nominal flow rate of the RAD7 pump was 1.0 LPM (litres per minute).

Therefore, one measurement cycle corresponds to approximately six full system recirculation for mixing.
The total radon emanating from the molecular sieves was calculated by extrapolating the radon activity at secular equilibrium, A_S, from the Equation 5.2 fit, and subtracting the background radon emanation of the setup.

5.3.3 Emanation results

The radon concentration as a function of time is shown in Figure 5.4 (NU-developed MS on the left and Sigma-Aldrich MS on the right). Equation 5.2 non-linear regression fits are shown as dashed red lines. The extrapolated radon emanation from this fit are shown in Table 5.1. Note that background emanation of the setup with an empty molecular sieve container was measured to be 4.69±1.1 mBq and subsequently subtracted from the results. Note that the relative humidity correction applied in subsection 5.4.2 was not required as the humidity was below 15% throughout.

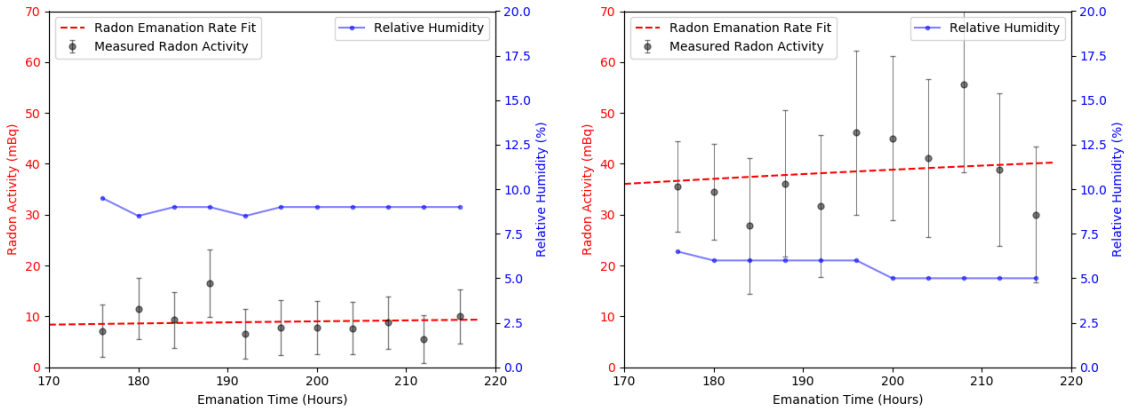

Figure 5.4 Plot of radon concentration as a function of emanation time. NU-developed MS on the left and Sigma-Aldrich MS on the right.

Molecular Sieve	**^{222}Rn Emanated (mBq)**	**Amount of MS Used (g)**	**^{222}Rn Emanated per kg (mBq/kg)**
NU-developed	6.95±1.64	70	99±23
Sigma-Aldrich	45.2±3.2	86	525±37

Table 5.1 Results of the MS intrinsic radon emanation test.

It can be seen from Table 5.1 that the NU-developed MS has significantly lower intrinsic radon emanation per unit mass by about a factor of 5. This result makes a promising case for the NU-developed MS to be used in radon filtration setups for ultra-low background SF_6-based physics experiments. However, to make a complete comparison, the radon capture efficiency of the MS must also be considered, as noted in Section 5.5.

5.4 Radon filtration tests

In Chapter 4, it was found that radon atoms have a critical diameter between 4 and 5Å, while SF_6 molecules have a critical diameter between 5 and 10Å [151]. This makes it possible to remove radon atoms from SF_6 with molecular sieves with 5Å sized pores. In the radon filtration test, the amount of ^{222}Rn captured by the molecular sieves from radon-contaminated SF_6 is measured. The radon filtration tests follow the method in Section 4.5 with a modified setup. A smaller gas reservoir was used to reduce the amount of greenhouse gas used. To account for the change in volume, radon concentration was converted to absolute radon activity in the data analysis, detailed in subsection 5.4.2.

5.4.1 Experimental setup and method

The radon filtration tests were performed using the experimental setup shown in Figure 5.5. The setup consists of the molecular sieve filter in a loop with a RAD7 radon detector and a gas reservoir. Also, included in the loop were connections to a passive PYLON 5.4kBq radon source; an SF_6 gas input; an EDWARDS vacuum pump and an MS filter bypass. The setup used several Swagelok valves to direct the gas flow either via the molecular sieve filter or MS bypass. Note that the RAD7 has a pump inside with a nominal flow of 1.0 LPM.

The filtration testing procedure started with the evacuation of the setup and the introduction of low humidity SF_6 gas to 760 torr. The gas was then contaminated with radon by opening the valve to the PYLON radon source, which was left to diffuse for 15 minutes. The valves were initially configured so that the gas flow direction was through the MS bypass. With the pump on, the RAD7 radon detector measurement started, recording every hour. After about 24 hours, the molecular sieve filter was engaged by opening the valves at both ends of the filter and closing the MS bypass valve. The RAD7 radon detector continued to measure for at least a further 20 hours.

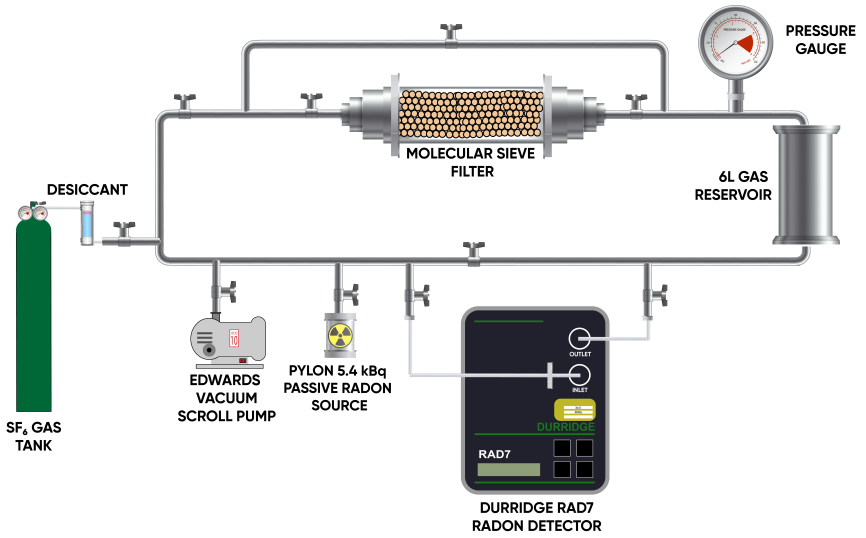

Figure 5.5 Schematic of the setup used for the radon filtration tests. Note that this figure is identical to Figure 4.6 and is included here for convenience and following the reproduction of paper [163]

5.4.2 Data Analysis

To calculate the amount of radon captured by the MS, the data was split into *MS off* and *MS on* data sets, which correspond to the measured data when the gas flow was directed via the MS bypass and MS filter, respectively. Both data sets were converted from radon concentration (Bq/m^3) to radon activity (Bq), by multiplying the radon concentration with the total volume in the radon filtration setup. The total volume was approximated to be the sum of the gas reservoir (6L) and the volume of the RAD7 (0.9L).

Two corrections were applied to the radon activity data before calculating the amount of radon captured. The first correction accounts for relative humidity (RH) in the chamber. A high concentration of water molecules in the chamber can suppress radon counts in the RAD7 detector. To compensate for lost radon counts, at RH higher than 15%, Equation 5.4 provided by DURRIDGE was applied to correct for high humidity. In this equation, A_m is the radon activity measured, A_c is the corrected radon activity and RH is the associated relative humidity with the radon measurement.

$$A_c = A_m \times \frac{100}{116.67 - 1.1 \times RH}. \tag{5.4}$$

The second correction applied ensures there was ample time for the radon from the PYLON source to distribute evenly throughout the system. Therefore, the first 4 hours of the data

were disregarded. Using the corrected data, the radon reduction due to the application of the MS was determined by fitting the *MS off* and *MS on* data sets to decay Equation 5.5. Note that the *MS on* fit was optimised by only including data after a new equilibrium was reached.

$$A(t) = A_0 \exp(-\lambda t). \tag{5.5}$$

$A(t)$ is the radon activity at time t, A_0 is the initial radon activity and λ is the radon decay constant. The initial radon activity, A_0, for both *MS off* and *MS on* data sets were extrapolated, and the effective radon reduction was determined by calculating the difference between the extrapolated A_0 values.

5.4.3 Radon filtration results

The radon activity as a function of time is shown in Figure 5.6 (NU-developed MS on the left and Sigma-Aldrich MS on the right). The *MS off* and *MS on* non-linear regression fits are shown in red and green dashed lines, respectively. The highlighted green area corresponds to when the molecular sieve filter was engaged. The blue points represent the relative humidity in the setup. The implementation of the molecular sieves, resulted in a drop in relative humidity, as expected. In addition, it is clear that the effective radon activity also decreases, results shown in Table 5.2. The NU-developed MS demonstrates the removal of radon from SF_6. However, at a lower radon capture efficiency(35±2 Bq kg^{-1}) compared to the Sigma-Aldrich MS (97±1 Bq kg^{-1}).

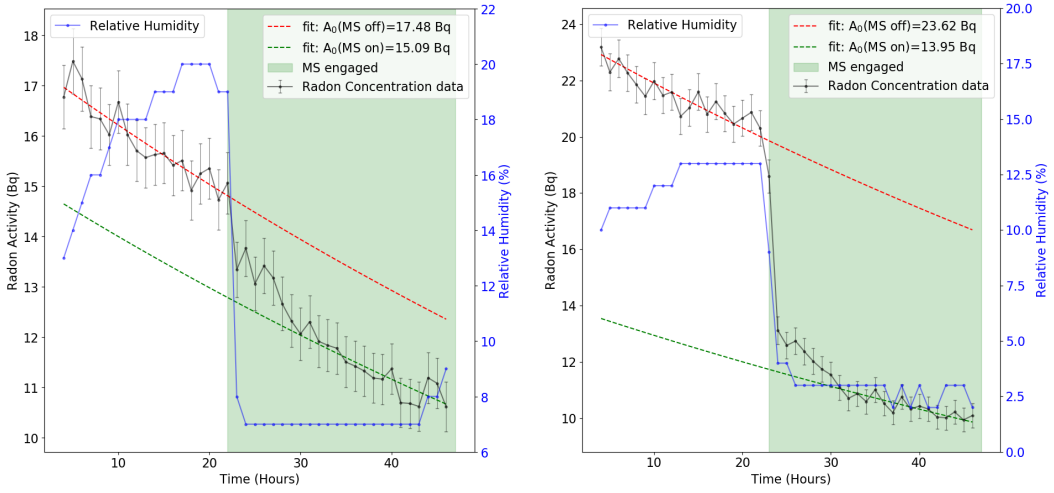

Figure 5.6 Plot of the change in radon concentration observed due to application of molecular sieve. NU-developed MS on the left and Sigma-Aldrich MS on the right.

Molecular Sieve	**Rn Captured (Bq)**	**Amount of MS Used (g)**	**^{222}Rn Captured per kg (Bq kg^{-1})**
NU-developed	2.39±0.10	68	35±2
Sigma-Aldrich	9.67±0.12	100	97±1

Table 5.2 Results of the radon filtration test.

5.5 Molecular sieve comparison

To provide a complete comparison of the molecular sieve candidates, the results from the emanation and filter tests were combined. A parameter indicating the amount of radon emanated by the MS per radon captured is shown in Table 5.3. This parameter was used as the figure of merit for the suitability of the MS for use in radon filtration setups for ultra-low background SF_6-based physics experiments, with a value that needs to be minimised. The NU-developed 5Å MS emanated radon 48±15% less per radon captured, compared to the commercial Sigma-Aldrich MS. This result shows that the NU-developed MS is a better candidate.

Molecular Sieve	**^{222}Rn Emanated per ^{222}Rn captured ($\times 10^{-3}$)**
NU-developed	2.8±0.7
Sigma-Aldrich	5.4±0.4

Table 5.3 Calculated comparison parameter, indicating the amount of radon emanated by the MS per radon captured by the MS from SF_6.

To determine if the NU-developed MS activity levels are acceptable for ultra-low background SF_6 gas-based physics experiments, let us consider a practical example. The DRIFT (Directional Recoil Identification From Tracks) Experiment is a gas-based direction dark matter experiment with chamber dimensions of 1.5 x 1.5 x 1.5 m^3. The radon activity due to material contamination in the experiment was measured to be 372±66 mBq [152].The 1 mBq radon background target, allows for up to 13g of NU-developed MS granules to be used. This amount equates to a capacity of 455±26 mBq, which is sufficient to capture all the radon in the detector (372±66 mBq). However, since radon capture is a probabilistic kinetic process, using a small amount of MS to capture a limited amount of radon atoms in a large volume would make the timescales problematic. Therefore, the filtration rate must be optimised when designing the gas system, maximising the contact time between the MS and the gas. Equally, using more sieves would improve the filtration rate as more pores will be available to capture radon. As larger-scale experiments will have more materials, radon contamination levels will

inevitably be higher. Therefore, efforts must continue towards minimising the emanation per radon captured parameter so that the total amount of MS allowed by the radioactive budget of an experiment is maximised.

5.6 Macroscopic geometry optimisation

The radon reduction result for the NU-developed MS is significantly less than the Sigma-Aldrich MS result, seen in Table 5.2. Optimising the radon filtration for NU-developed MS could possibly improve the radon emanated per radon captured parameter. The filtration discrepancy may be attributed to the difference in their geometries and surface area to volume ratio, seen in Figure 5.2.

In a bid to improve the radon capturing capabilities of the NU-developed MS, its surface area to volume ratio was increased by crushing it from its irregular granular form was into a fine powder with a mortar and pestle, as shown in Figure 5.7. The radon filtration test, discussed in Section 5.4, was repeated with the NU-developed MS in its powder form. It is worth noting that the significant increase in surface area to volume ratio has implications that there will be an increase in the amount of radon emanated from the MS, as the path from inside the material to the surface is reduced. Therefore, the emanation test, discussed in Section 5.3, was also repeated with the powder form.

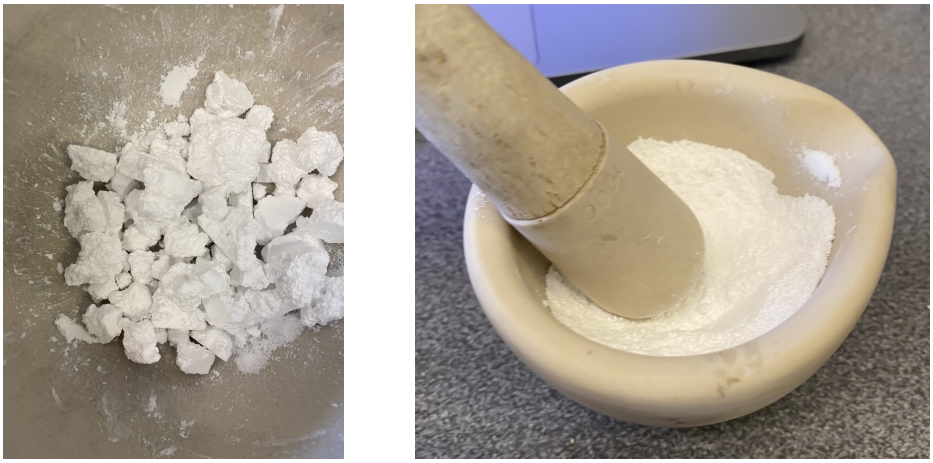

Figure 5.7 Images of the NU-developed MS before and after crushing it into a fine powder.

The results for the powder form of the NU-developed MS test are shown in Table 5.4, with the corresponding filtration and emanation plots in Figure 5.8. The radon reduction efficiency has significantly improved from 35±2 to 330±3 Bq kg^{-1}. As expected, the intrinsic radon emanation has significantly worsen from 99±23 to 680±30 mBq. However, the radon

emanated per radon captured parameter has remained the same within errors. Overall, crushing the MS into powder did not improve is suitability for use in radon filtration setups for ultra-low background as demonstrated by our parameter.

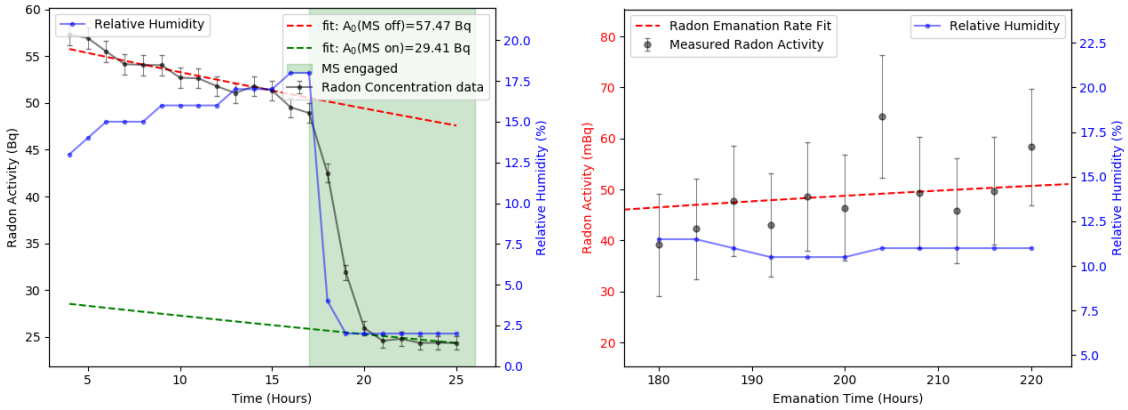

Figure 5.8 Plot of the change in radon concentration observed while using the powdered NU-developed MS (left) and a plot of radon concentration as a function of emanation time (right) in the powdered NU-developed MS emanation test.

NU-developed MS	**^{222}Rn Captured per kg (Bq kg^{-1})**	**^{222}Rn Emanated per kg (mBq kg^{-1})**	**^{222}Rn Emanated per ^{222}Rn Captured ($\times 10^{-3}$)**
Granules	35±2	99±23	2.8±0.7
Powder	330±3	680±30	2.1±0.1

Table 5.4 Radon filtration, intrinsic MS emanation and comparison parameter results for the NU-developed MS in granule and powdered form. Note that 85g of NU-developed MS were used in the powdered tests.

5.7 Conclusions

In this chapter, a method to determine the suitability of a molecular sieve candidate for use in ultra-sensitive SF_6 gas-based rare-event physics experiments was proposed. A parameter indicating the amount of radon intrinsically emanated per unit radon captured by the sieve from SF_6 was experimentally determined. A low radioactive MS candidate developed by Nihon University in collaboration with Union Showa K.K was tested and compared to a commercially manufactured Sigma-Aldrich MS. It was found that the NU-developed MS emanated 48±15% less per radon captured $(2.8\pm0.7)\times10^{-3}$, compared to the commercial Sigma-Aldrich MS $(5.4\pm0.4)\times10^{-3}$. An attempt to improve this result was made by crushing

the MS into a powder, increasing its surface area to volume ratio. The powder form significantly increased the radon capture efficiency. However, the intrinsic radon emanation also worsened. Overall, there was no change in the emanation per radon captured parameter for the NU-developed MS powder $(2.1\pm0.1)\times10^{-3}$. The total reduction in our parameter with the powdered NU-developed MS compared to the Sigma-Aldrich MS was 61±9%, which is within errors of the original granulated NU-developed MS. When constructing a radon filtration setup in practice, it is important to take into account the timescale required to capture radon at low levels. One way to achieve this is by maximising the amount of MS used, which in turn increases the number of available adsorption sites, thereby enhancing the rate of radon capture, which is a probabilistic and kinetic process. The NU-developed MS provides a suitable candidate for use in a radon filtration setup for future ultra-sensitive SF_6 gas-based experiments, maximising the total amount of MS allowed by the radioactive budget of an experiment. Since the publication of this paper, a new version of NU-developed MS (V2) with cleaner calcium was tested, detailed in subsection 5.8.2. The NU-developed MS (V2) parameter upper limit was found to be 1.7×10^{-5}, equating to at least 98.9%less radon emanated per radon captured, compared to the commercial Sigma-Aldrich MS.

The demonstration of radon removal from SF_6, described in Chapter 4, and identification of a low radioactive 5Å type molecular sieve, discussed in this chapter, indicates a radon removal system for ultra-sensitive SF_6-based rare-event physics experiments is feasible. Chapter 6 focuses on the design of a gas system capable of employing molecular sieves with gas-based detectors.

5.8 Additional information

This section supplements the published article with additional information, and does not contradict the original publication. The SF_6 calibration factor determined in Chapter 3 is applied to the radon measurements conducted in this chapter and is presented in subsection 5.8.1. Since the same factor is applied to all measurements, there is no overall effect on the results, despite the fact that the absolute values change. A new version of NU-developed MS has been synthesised, and the examination of this candidate is detailed in subsection 5.8.2.

5.8.1 RAD7 calibration for SF_6

The DURRIDGE RAD7 is not calibrated to measure in carrier gas SF_6, so a calibration factor must be applied to account for changes in the collection efficiency due to the carrier gas SF_6. For a DURRIDGE calibrated RAD7, it was determined that the output must be multiplied by 3.33 to account for the carrier gas SF_6, detailed in Chapter 3.

The emanation results in section Section 5.3 remain the same as the carrier gas used in the measurements was N_2, which is the default carrier gas for the RAD7. However, the filtration tests in Section 5.4 were conducted in carrier gas SF_6, so the calibration factor must be applied to these results. The updated results for the parameter indicating the amount of radon intrinsically emanated per unit radon captured by the sieve from SF_6 is shown in Table 5.5.

Molecular Sieve	**^{222}Rn Captured per kg (Bq kg^{-1})**	**^{222}Rn Emanated per kg (mBq kg^{-1})**	**^{222}Rn Emanated per ^{222}Rn Captured ($\times 10^{-4}$)**
Sigma-Aldrich	323±3	525±37	16±1.2
NU (Granules)	117±7	99±23	8.5±2.0
NU (Powder)	1100±10	680±30	6.2±2.8

Table 5.5 Radon filtration, intrinsic MS emanation and comparison parameterresults with the RAD7 SF_6 calibration factor applied.

The outcome of the chapter has not changed. The NU-developed 5Å MS emanated radon 47±13 % less per radon captured, compared to the commercial Sigma-Aldrich MS, and the parameter for the NU-developed in granule and powder form remain the same within errors.

5.8.2 NU-V2 MS Candidate

Since the publication of the paper [163], a new version of Nihon University MS has been developed. The NU-V2 MS candidate was tested following the method outlined in this chapter. In the original NU-developed MS, the calcium ion used in the synthesis was found to be the driving radon emanator. In a bid to further improve the intrinsic emanation, a cleaner calcium supplier was sought for the second version of the NU molecular sieves. A photo of the NU-developed MS (V2) in irregular powder form is shown in Figure 5.9. The radon filtration test, discussed in Section 5.4, and the emanation test, discussed in Section 5.3, were repeated for NU-developed MS (V2) to provide a complete comparison.

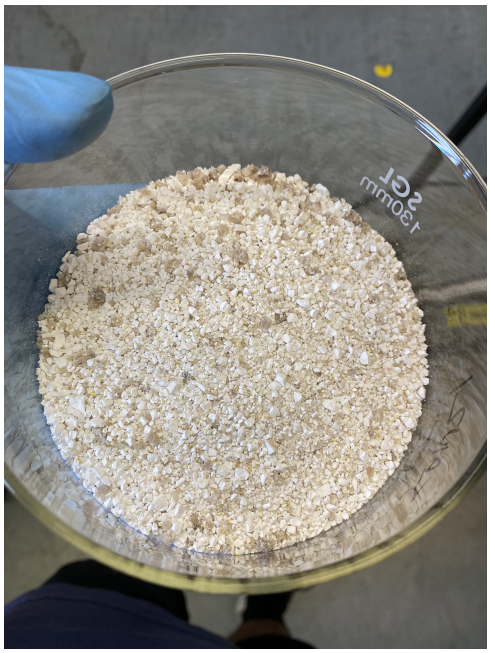

Figure 5.9 Image of the NU-developed MS (V2).

The results for the NU-developed MS (V2) test are shown in Table 5.6, with the corresponding filtration and emanation plots in Figure 5.10. The geometry of NU-developed MS (V2) is similar to the powdered form of NU-developed MS (V1), demonstrated by their comparable radon reduction efficiencies measurements, 846 ± 10 Bq kg^{-1} and 1100±10 Bq kg^{-1}, respectively. The intrinsic radon emanation of NU-developed MS (V2) was measured as 6.6±7.8 mBq kg^{-1}. The large error is expected the experimental setup background limits is reached. Therefore, the upper limit of 14.4 mBq kg^{-1} is used. The upper limit value is significantly less than the powdered form of NU-developed MS (V1) (680±30 mBq kg^{-1}), clearly showing that the new calcium ion supplier has reduced the total emanation of the molecular sieves.

The radon emanated per radon captured parameter upper limit is 1.7×10^{-5}, equating to at least 98.9% less radon emanated per radon captured, compared to the commercial Sigma-Aldrich MS. To the author's knowledge, these are the lowest intrinsically emanating radon-absorbing material per unit mass (activated charcoal or molecular sieves).

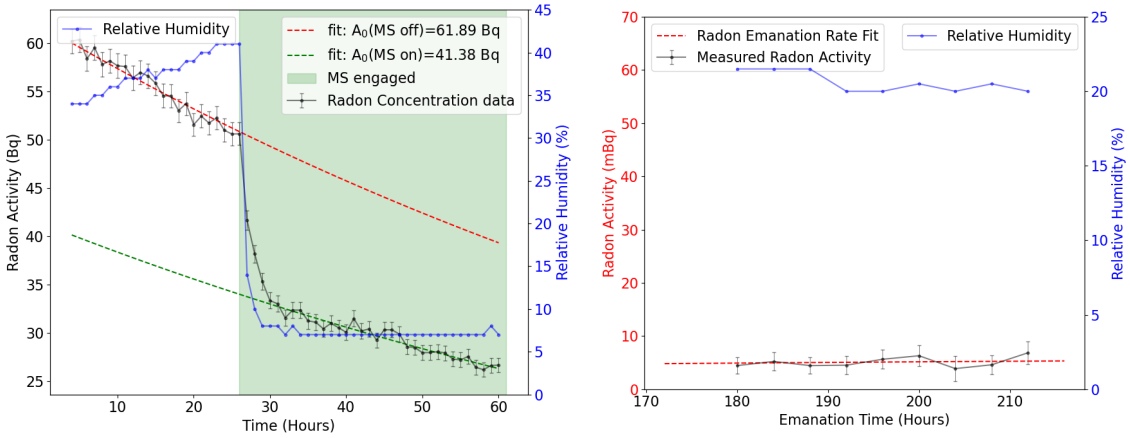

Figure 5.10 Left plot of the change in radon activity observed due to the application of the NU-developed MS V2. Right plot of radon activity as a function of emanation time in the NU-developed MS V2 emanation test. Note the radon activity scales kept consistent with the powdered NU-MS plots in Figure 5.8.

NU-developed MS	**^{222}Rn Captured per kg (Bq kg^{-1})**	**^{222}Rn Emanated per kg (mBq kg^{-1})**	**^{222}Rn Emanated per ^{222}Rn Captured ($\times 10^{-4}$)**
V1 (Granules)	117±7	99±23	8.5±2.0
V1 (Powder)	1100±10	680±30	6.2±2.8
V2 (Powder)	846±10	<14.4	<0.17

Table 5.6 Radon filtration, intrinsic MS emanation and comparison parameter results for the NU-developed MS in granule and powdered form and NU-developed MS V2 with the RAD7 SF_6 calibration factor applied.

Chapter 6

Development of an MS-based Vacuum Swing Adsorption gas recycling system

The importance of removing radon contamination and common pollutants from gas-based directional dark matter detectors was highlighted in Chapter 2. The demonstration of radon removal from SF_6, described in Chapter 4, and identification of a low radioactive 5Å type MS, described in Chapter 5, suggests a radon removal system for ultra-sensitive SF_6-based rare-event physics experiments is feasible. Moreover, in the work described in Chapter 4, it was determined that 3Å and 4Å type MSs do not absorb SF_6. Since these MSs types are known to remove common pollutants [170], employing a gas filtration system utilising 3Å, 4Å, and 5Å MSs has the potential to remove radon contamination and common pollutants simultaneously.

The development towards a gas system allowing continuous use of MSs filters while minimising the loss of SF_6 gas during operation is discussed in this chapter. The gas system design utilises a modified vacuum swing adsorption (VSA) with a gas recovery buffer, detailed in Section 6.1. Construction of a prototype suitable for assessing the gas system concept with a small-scale gas TPC detector is described in Section 6.2. The operation of the prototype with an engineering demonstration is outlined Section 6.3.

6.1 Gas system design

The simplest gas recycling system design would consist of a single MS filter in line with the detector. However, for long-term continuous operation, issues arise when saturation of the filter is approached and no further adsorption takes place, known as breakthrough. Although a larger filter can improve breakthrough time, the larger filter will consequently emanate

more radon into the system. The ideal gas recycling system would use a limited amount of MSs while maintaining full filtration capabilities throughout the long-term continuous operation. A filtration technique that can achieve this is Vacuum Swing Adsorption (VSA).

6.1.1 Introduction to Vacuum Swing Absorption (VSA)

Vacuum swing adsorption (VSA) is a cyclic process that allows the continued use of absorbent material, such as MSs. When absorbent materials reach their capacity, they can be regenerated using a vacuum to desorb the captured gas components. Vacuum is a safer method of regeneration compared to the common practice of baking absorbents at temperatures above 400 C [171]. Figure 6.1 shows an example of vacuum swing absorption with dual absorbent vessels. The left filter is undergoing vacuum regeneration, with the captured contaminants being removed from the MS pores. Simultaneously, the right filter is filtrating contaminants from the desired gas. A four-way solenoid, depicted as the black box in the figure, allows redirection of gas flow from left or right filter.

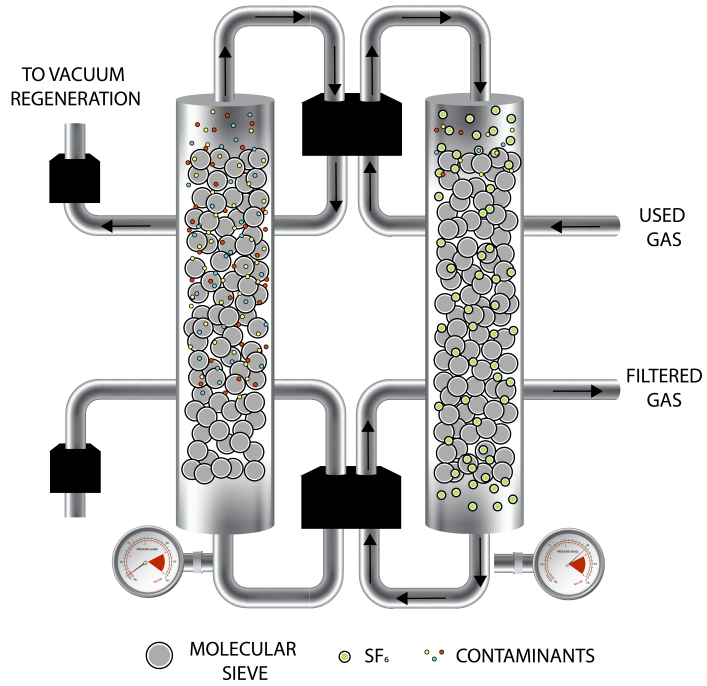

Figure 6.1 Schematic of vacuum swing adsorption technique. The left filter is being regenerated under vacuum, which removes the captured contaminants from the pores of the MS. At the same time, the right filter is removing contaminants from the desired gas. A four-way solenoid, shown as a black box in the figure, can redirect the gas flow from either the left or right filter.

Once an absorbent reaches its capacity, it *swings* to the regenerated absorbent for filtration and starts regenerating the saturated absorbent. The process repeats for the lifetime of the absorbent, with commercial systems claiming up to 40,000 hours of operation [172]. The VSA technique has successfully been applied to activated-charcoal-based gas systems for low radon clean rooms [116, 117, 173], an example of such a system was previously described in Chapter 2. These VSA systems can achieve high flow rates $\mathcal{O}$(1000 LPM), which is required for scaling up gas systems for use with larger experiments.

6.1.2 VSA with gas recovery design

A gas system utilising a Vacuum Swing Adsorption (VSA) technique seems the most appropriate design to effectively implement the MS filters with an SF_6 gas-based experiment. Unfortunately, in VSA systems, a small fraction of SF_6 gas is lost from the absorbent filter when vacuum regenerating. The release of SF_6 gas during vacuum regeneration is a significant issue but can be solved by incorporating a gas recovery buffer. Coupling the VSA technique with a gas recovery buffer allows the collection of the lost SF_6 gas during vacuum regeneration by feeding it back to the gas buffer, maximising the amount of gas recycled. A further advantage of utilising a gas buffer is that fewer components are directly exposed to the detector volume, thereby reducing the number of potential radon sources. An engineering advantage is that the gas buffer allows the gas system to operate at a different pressure from the detector; otherwise, for low-pressure detectors, keeping a complex gas system leak tight is technically challenging. Therefore, a VSA system with a gas buffer will be the basis of the gas recycling system design. An overview of the gas design is shown in Figure 6.2, where the gas system is separated into three modules.

Molecular sieve module The *molecular sieve module* consists of two absorbent filters connected to four-way solenoid valves. The four-way valves allow the redirection of two independent lines. In this case, the two MS filters can be readily switched between lines towards the gas buffer cylinder or vacuum regeneration output. Notice the vacuum regeneration output has a gas recovery line towards the gas buffer cylinder. The desired gas in the MS filter is collected by the gas transfer pump above the critical regeneration pressure. This critical pressure corresponds to the point at which the captured components start to be desorbed by the vacuum.

Gas buffer module The *gas buffer module* consists of a cylinder controlled by a three-way solenoid valve. The gas flow can be directed to the *detector I/O module* or *molecular sieve module*. The gas buffer is used as the intermediate between filtration with the MSs and gas

replacement with the detector. During filtration, the buffer stores the volume of gas being cleaned. During gas replacement, the buffer fills the detector with *clean* gas, effectively diluting the *used* detector gas. The original detector pressure is restored by transferring the additional gas back to the buffer cylinder with a gas transfer pump.

Detector I/O module The *detector I/O module* controls the detector vessel's gas input and output. A proportional solenoid valve precisely controls the flow from the gas buffer cylinder to the detector vessel. The gas flow is driven by the pressure gradient between the high-pressure buffer and the low-pressure detector vessel. Whereas, the output flow from the detector to the gas buffer is driven by a gas transfer pump.

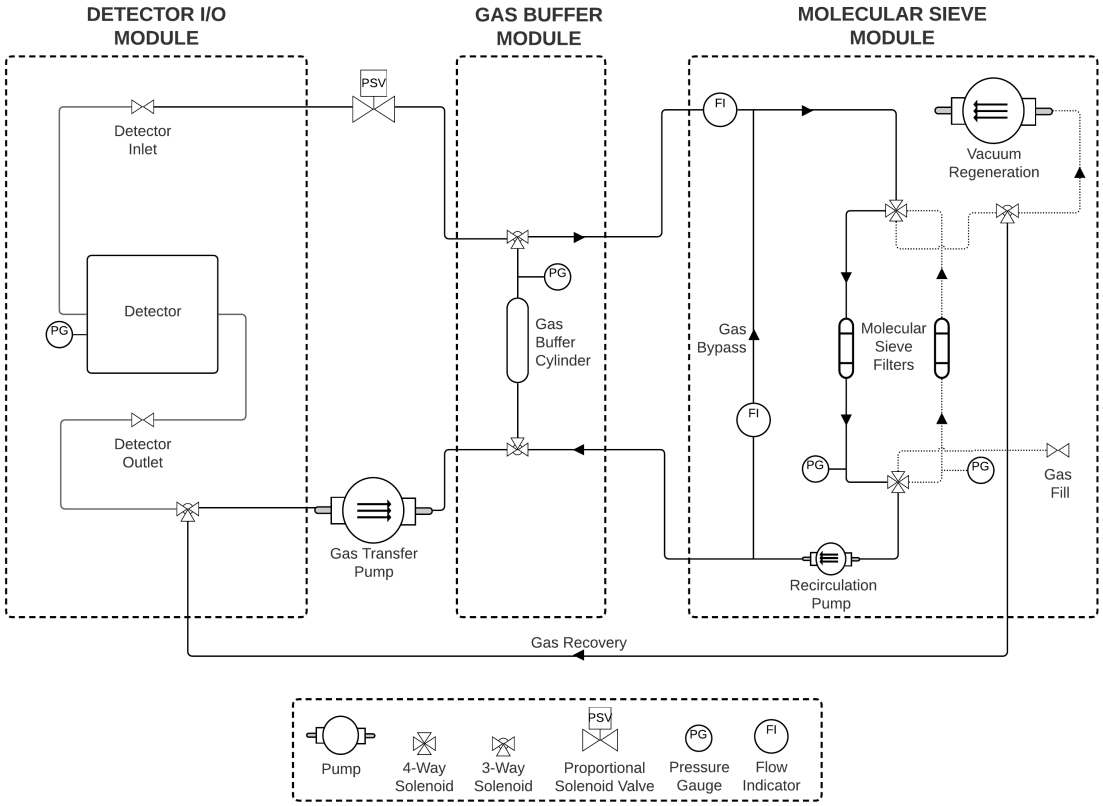

Figure 6.2 A simplified schematic of the gas system, with the *detector I/O*, *gas buffer*, and *molecular sieve* modules highlighted by dashed boxes. The flow direction of the gas is indicated by the arrow, with solid and dotted lines indicating different gas path lines. Further details regarding the gas system components can be found in the key located at the bottom of the figure.

6.1.3 VSA with gas recovery operation

The operation of the gas system can be understood by considering two separate volumes, the gas inside the detector vessel and gas inside the buffer, indicated in Figure 6.3 as yellow and green areas, respectively. While the detector is online, the buffer volume is continuously filtered by the MSs. After a certain period, the detector volume will become contaminated due to mini leaks, outgassing and radon emanation. To combat contamination, the cleaner gas inside the buffer is flowed to the detector vessel, effectively cleaning the detector gas by dilution. The detector pressure is restored to its original configuration by transferring the additional gas to the buffer and resumes filtration. The required frequency for the dilution process depends on the detector's contamination rate.

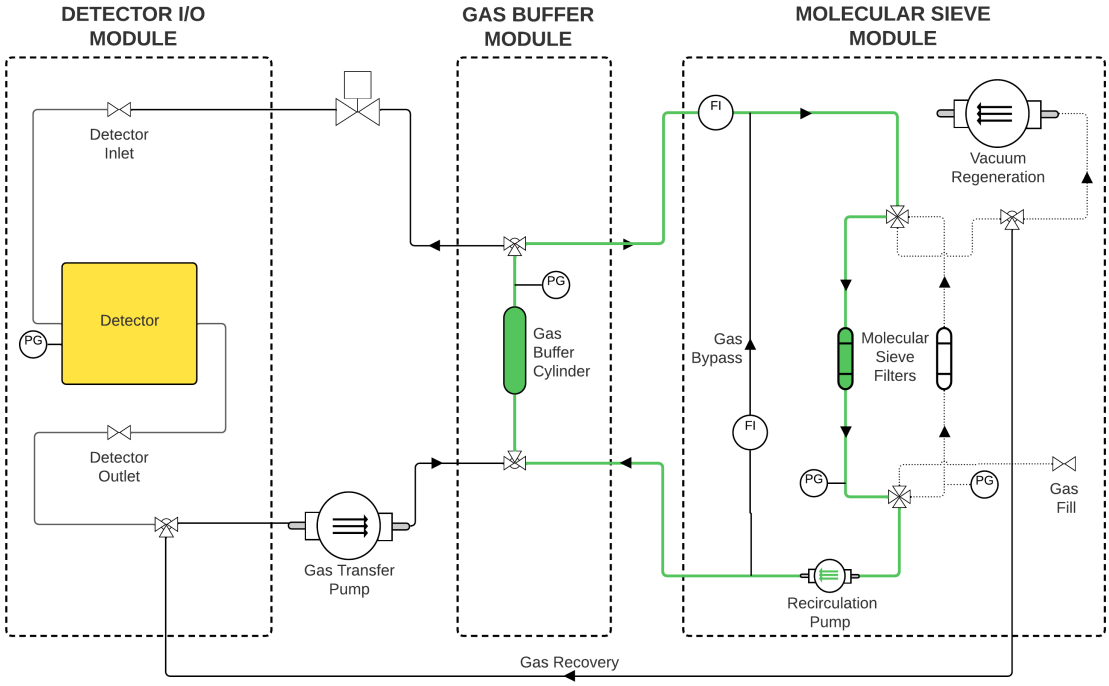

Figure 6.3 Schematic illustrates the two separate volumes within the system: the gas inside the detector (shown in yellow) and the gas inside the buffer (shown in green). The green loop corresponds to filtration using the gas buffer cylinder, while the gas shaded in yellow corresponds to the gas used during detector operation.

The dual column configuration ensures a MS filter is always available by allowing simultaneous filtration and regeneration. The MS filters swing from filtration and regeneration and vice versa before the breakthrough time of the filter. The time for breakthrough is a function of the MS filter's dimensions and flow parameters, which must be calibrated for

operation. Figure 6.4 shows an example of the operation timeline of the dual MS filters and detector. The timescale for detector gas dilution and gas recovery is minutes, whereas detector operation, filtration and regeneration are days.

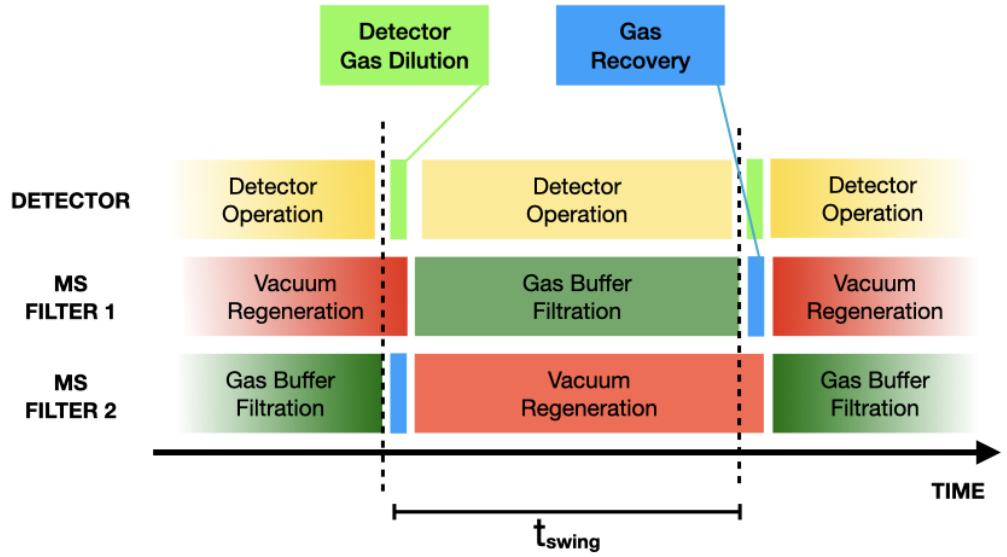

Figure 6.4 Example timeline of VSA operation showing the operation modes for the detector and dual MS filters. Here, t_{swing} is in the order of days, and detector gas dilution and gas recovery are in minutes.

The process of filtration and regeneration is schematically shown in Figure 6.5. The filtration process (green line) is achieved by continuous gas flow through the MSs and gas buffer, driven by a recirculation pump. The regeneration process occurs in two steps, gas recovery and vacuum regeneration. Gas recovery (blue line) corresponds to the collection of the small gas volume in the MS filters, which is lost in conventional VSA during vacuum regeneration. The gas is collected by evacuating the MS filter using the gas transfer pump, with the output redirected to the gas buffer cylinder. The MS filter is evacuated just above the critical regeneration pressure, $\mathcal{O}$(10 torr) [174, 175], ensuring that most of the gas is recovered whilst avoiding the release of captured contaminants. Once the filter gas is recovered, vacuum regeneration (red line) is initiated by applying a sub-torr vacuum.

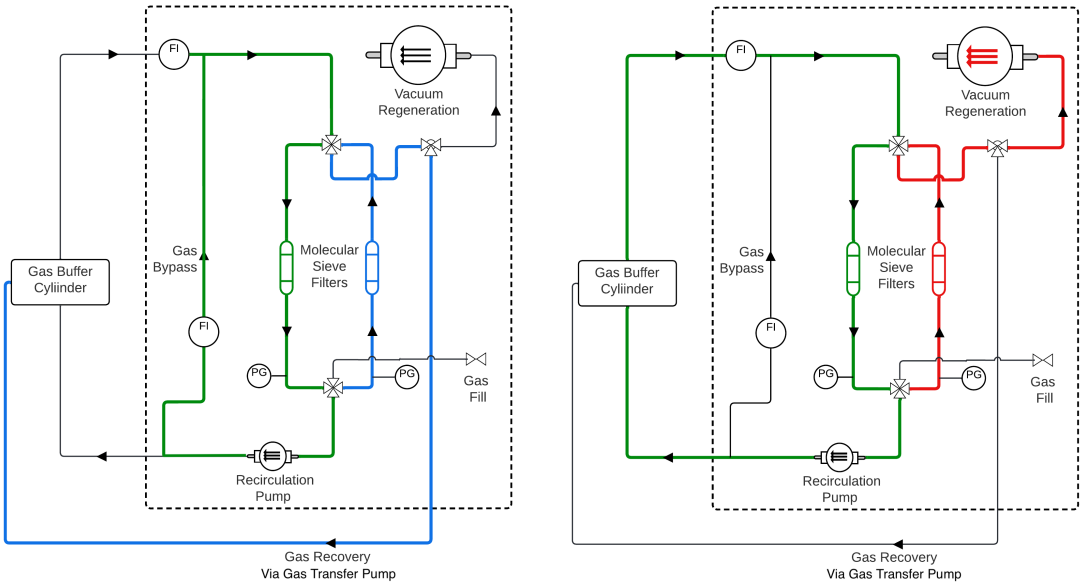

Figure 6.5 Schematic of the molecular sieve module during gas recovery (left) and vacuum regeneration (right).

6.2 Prototype construction

Covered in this section are details of the construction of a prototype set-up based on the design presented Section 6.1. Key to the assessment of the concept will be the operation with a gas TPC detector, to demonstrate the removal of intrinsic radon contamination and the removal of common pollutants. The removal of intrinsic radon contamination will be measured directly, while the removal of common pollutants will be measured by monitoring the detector's gain amplification capabilities, details of these experiments and the detector used are discussed further in Chapter 7.

6.2.1 Components selection

The selection for the buffer cylinder size, MS column size, recirculation pump and gas transfer pump are dependent on the detector's configuration, namely operating pressure, P_{det}, and detector vessel volume, V_{det}. The detector that will be used to assess the concept of the gas system in Chapter 7 has a V_{det}=100 L and P_{det}=50 torr. Therefore, the selection of the gas system components appropriate for this scale is discussed below, with an overview of components used shown in Table 6.1.

Buffer cylinder size Since the buffer cylinder will be required to contain a detector volume of gas during operation, an appropriately pressure-rated cylinder is required. A detector volume of 100L at 50 torr equates to 0.27 moles of gas. A small cylinder can easily contain this amount of gas. However, consideration for the operational pressure of other components must be taken. As a precaution, a buffer cylinder size was chosen so that the a detector volume in the cylinder equated to a pressure $\mathcal{O}$(1 atmosphere). The cylinder selected was a standard double-ended cylinder from Swagelok with a volume of 4.5L.

MS filter size The amount of MS required depends on the contamination rate of the detector and the amount of gas filtered. The radon removal demonstration in Chapter 4 was completed at high levels of radon, $\mathcal{O}(1kBq)$ and required $\sim$ 100 g of MS to remove 87%. As radon removal is a probabilistic kinetic process, the capture rate is expected to decrease with radon concentration. To combat the increased timescales required at lower concentrations, two large MS columns with a capacity $\sim$ 500g each, made by Kurt. J Lesker, were chosen.

Recirculation pump The pressure in the buffer-MS filter loop during gas system operation must be considered when choosing a recirculation pump. It can be assumed that the recirculation pump's operating pressure rating will determine the maximum pressure allowed in the buffer-MS filter loop since the buffer cylinder and MS columns are rated to pressures of 100 atmospheres or higher. A recirculation pump that can continuously operate at suitable flow rates is required to maximise the contact time between the MS and the gas. A dry-diaphragm pump, made by KNF, rated up to 2.5 atmospheres with flow rates up to 8 LPM was chosen. This model has been tried and tested with a similar-sized gas system [176].

Gas transfer pump The pressure of the detector, P_{det}, and the pressure of the buffer cylinder, P_{buf}, must be considered when choosing a gas transfer pump. The pump must be able to pump down to P_{det} pressures and output to P_{buf} pressures. An oil-free dry pump type is preferred to avoid introducing additional contaminants. A dry vacuum scroll pump with a closed gas ballast by Edwards was chosen.

Vacuum regeneration pump The vacuum pump used for regeneration is not dependent on the configuration of the detector. The vacuum pump must evacuate to sub-torr pressures and operate continuously. A dry vacuum scroll pump by Edwards was chosen.

Gas control and monitoring To control the gas flow, three types of solenoid valves made by Humphreys were chosen: proportional, 3-way and 4-way valves. The proportional

solenoid valve precisely controls the flow of gas. The 3-way and 4-way valve operations are shown in Figure 6.6, where the red and the blue arrows correspond to available path for gas flow. The 3-way redirects an inlet into two possible outlets, whereas the 4-way valve redirects two separate pipelines. The solenoid valves are controlled with relay switches connected to a Raspberry Pi microcomputer. A series of manual needle valves and volumetric flow meters by Swagelok was chosen to precisely tweak the gas flow. To monitor the pressure throughout the gas system, absolute piezoelectric pressure gauges by CYNERGY with a 4-20mA output were chosen.

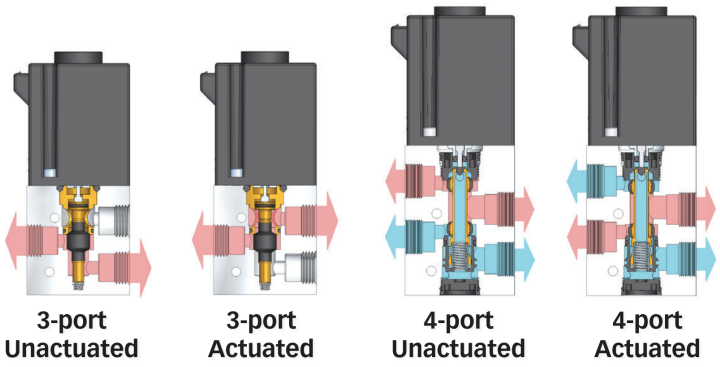

Figure 6.6 Operation of 3-way and 4-way solenoid valves, the application of 24V DC actuates the valves. Image from Humpreys INC.[177].

Module	Component	Description	Manufacturer	Model No.
Molecular Sieve	MS Containters	Meshed, 0.6L	Kurt J Lesker	CUSTOM
	Recirculation Pump	Diaphram	KNF	N96KNDC-B-M
	VacGen Pump	Dry Vacuum Scroll	Edwards	XDS 5/10
Gas Buffer	Gas Cylinder	Double Ended, 4.5L	Swagelok	304L-HDF4-1GAL
	Transfer Pump	Dry Vacuum Scroll	Edwards	XDS 5/10
	Mass flow controller	Proportional Solenoid	Humphreys	10032300
Control	Solenoid Valves	3-way and 4-way	Humphreys	420 VAI 24VDC
	Needle Valves	Manual Precise Valves	Swagelok	SS-1VS8
	Quarter-turn Valves	Manual Valves	Swagelok	SS-4P4T
	Pressure Gauges	Absolute Piezoelectic	CYNERGY	IPSLU-AP015-5
	Flow meter	Volumetric Flow	Swagelok	VAF-G2-12L-1-0
Monitor	Microcomputer	-	Rapberry Pi	RPI4-MODBP-8GB
	Relay switches	-	Pi-Plates	RELAYPlate
	ADC	-	Pi-Plates	DAQC2Plate
	Touch Display	Local Control	Raspberry Pi	LCD 2473872

Table 6.1 Overview of the main components used in the molecular sieve gas system.

6.2.2 Construction

The gas system design was configured into a freestanding unit. A 3D CAD model of the gas design and a photo of the constructed gas system are shown in Figure 6.7 and Figure 6.8, respectively. The front, shown on the left of the figures, contains the *buffer module* and *molecular sieve module*, excluding the two MS filters which are mounted on the rear of the gas system. The front and rear are connected through a feed-through. Stainless steel vacuum pipes with 1/4" Swagelok connections are used to connect all the components. The gas system input and output to the detector vessel are located on the side of the unit. The gas fill and vacuum regeneration connections are on the opposite side. The gas transfer pump is placed next to the unit. The solenoid valves and pressure indicators are connected to the Raspberry Pi microcomputer and powered by a DC power supply. A touch screen LCD, located at the front, interfaces the Raspberry Pi microcomputer.

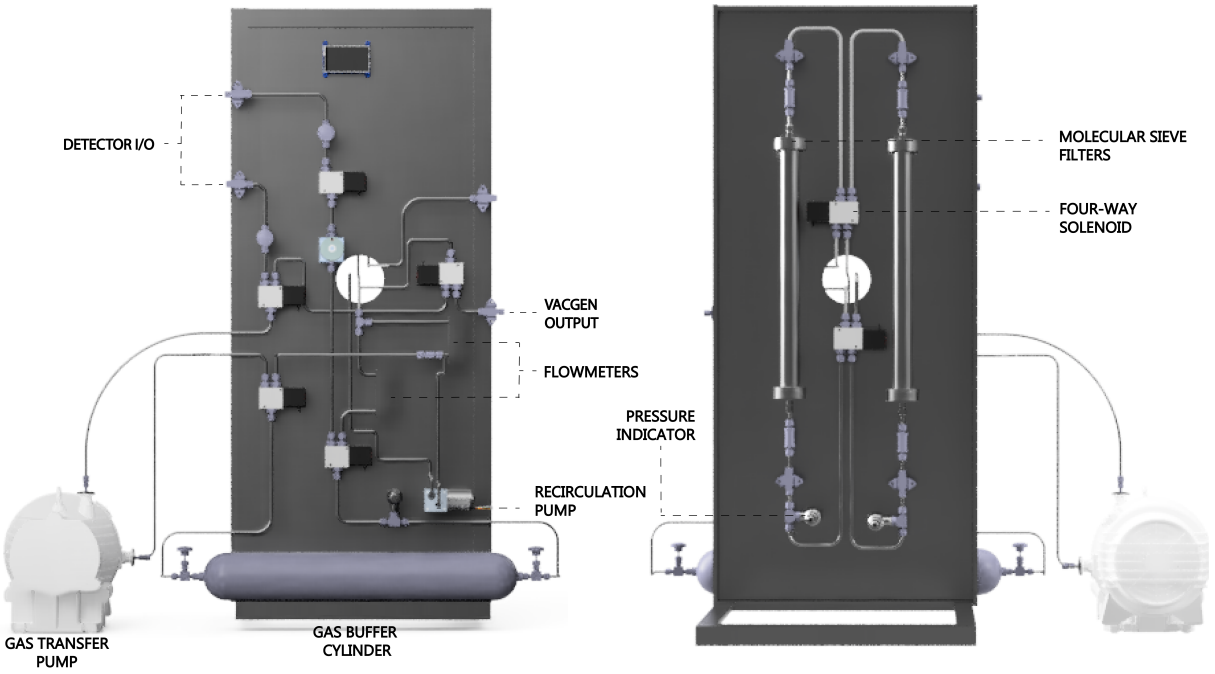

Figure 6.7 3D CAD model of the gas system design configured into a freestanding unit. The front and rear of the gas system are shown on the left and right, respectively.

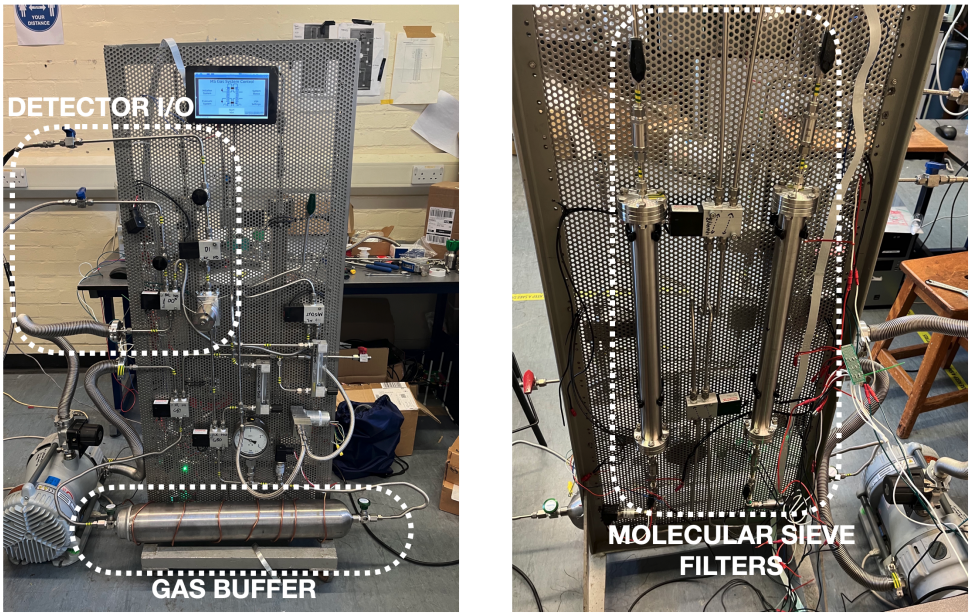

Figure 6.8 Photo of the front and rear view of the constructed MS gas system.

6.3 Prototype operation

Operation with the gas system prototype is described in this section. General step-by-step instructions for a detector configuration with vessel volume V_{det} and operating pressure P_{det} are outlined. Followed by an engineering test in SF_6 with a detector configuration V_{det} =100 L and P_{det} =50 torr. The engineering test aims to demonstrate that the gas system prototype can be applied to a detector operating with this configuration.

6.3.1 Method of operation

Before using the gas system four operating parameters are set: the gas buffer volume, V_{buf}, the detector vessel volume, V_{det}, the desired operating detector pressure, P_{det}, and the desired time between the swing process, t_{swg}. The gas system method of operation can be considered in five steps: initial gas setup, gas dilution, gas recovery, MS filter swing, and termination. The sequence is as follows:

Initial gas setup Setup starts with the detector vessel and gas system at vacuum. The detector vessel is filled with an amount of gas approximately equal to two detector volumes. Since the gas dilution process is driven by a pressure gradient, an additional amount of gas

must be added to the initial fill to ensure equilibration between the gas buffer and detector vessel resulting in two detector volumes inside the detector vessel. This is required to effectively replace the total volume in the detector vessel during dilution. The initial gas fill, P_{fill}, in the detector vessel, is given by

$$P_{fill} = 2P_{det}\left(1 + \frac{V_{buf}}{V_{det}}\right), \tag{6.1}$$

here P_{det} is the desired detector operating pressure, V_{buf} is the gas buffer volume, and V_{det} is the detector vessel volume. Once the detector vessel is filled, the gas is transferred to the buffer cylinder until the detector is at the desired pressure, P_{det}. The buffer cylinder is redirected to the MS filter and starts gas filtration, and the other MS filter starts vacuum regeneration, and then detector operation begins.

Gas dilution After time t_{swg}, the filtered gas in the buffer cylinder is introduced to the detector volume, resulting in the detector pressure to equilibrate at $2\times P_{det}$. The gas is left to mix for a couple of minutes, effectively cleaning the *used* gas by dilution. The gas in the detector volume is transferred back to the buffer cylinder until the detector is at the pre-dilution pressure, P_{det}, and then detector operation resumes.

Gas recovery Gas recovery occurs immediately after a gas dilution and prior to the MS filter swing. The small amount of gas inside the MS filter, previously used for filtration, is collected in the buffer cylinder. In cases where the column is filled with MSs to capacity, this amount is minimised. The gas is collected using the transfer pump until the pressure in the filter is just above the critical regeneration pressure, $\mathcal{O}$(10 torr) [174, 175].

Molecular sieve filter swing Upon completion of gas recovery, the transfer pump is switched to the vacuum pump to initiate vacuum regeneration while the previously regenerated MS filter starts gas buffer filtration. After time t_{swg}, the gas dilution, gas recovery, and MS filter swing cycle is repeated until the end of the detector operation.

Termination When detector operation is terminated, the gas in both MS filters is returned to the buffer cylinder. The gas contained in the detector and buffer cylinder is collected and properly disposed of.

6.3.2 Engineering test at 50 torr in 100L vessel configuration

To assess the concept of the MS-based VSA gas recycling system design, it will be applied to a gas TPC detector operating at a pressure of 50 torr in a 100 L vessel, detailed in Chapter 7. Prior to full detector operation, the gas system will undergo an engineering test to demonstrate the method outlined in the subsection 6.3.1. In gas TPC operation, constant pressure is crucial to ensure stable detector performance. Therefore, this engineering test also aims to demonstrate that P_{det} in the test vessel can remain at 50 torr with the gas system applied.

Figure 6.9 shows the gas system connected to a 100 L test detector vessel which is shown on the left of the photo. The time between swings was set to $t_{swg} = 24$ hours, so approximately one detector volume was replaced per day. The MS filters were packed to capacity with $\sim$ 500g in each column. To help understand each step during the engineering demonstration, a complete schematic of the gas system and 100 L vessel with all valves detailed is shown in Figure 6.10. The corresponding status of all valves for each step is shown in Figure 6.11.

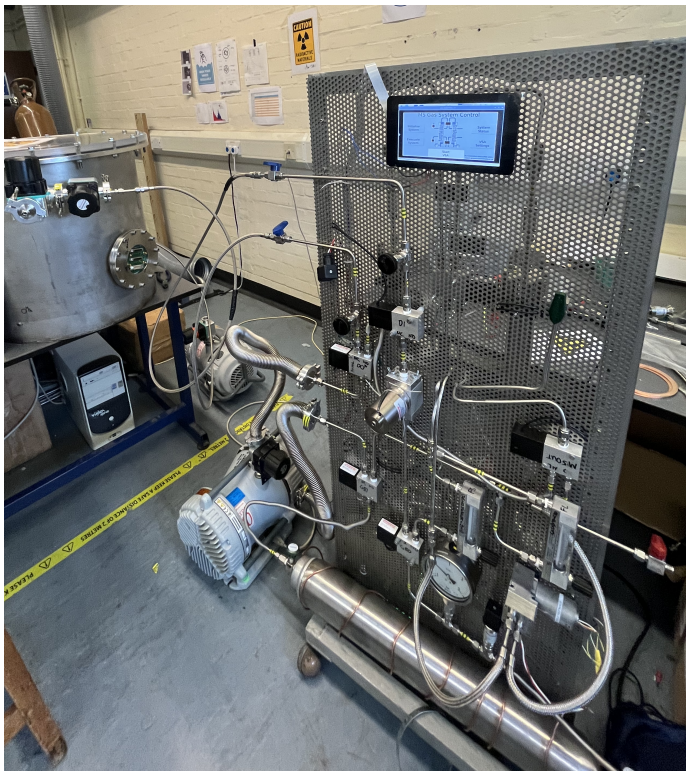

Figure 6.9 Photo of gas system prototype connected to a 100L test vessel.

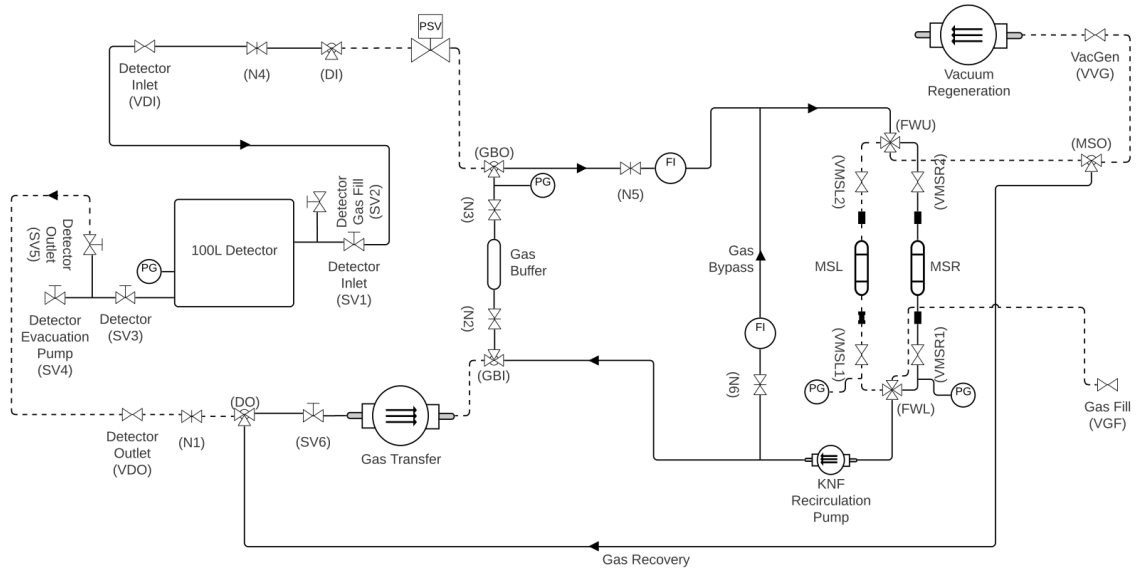

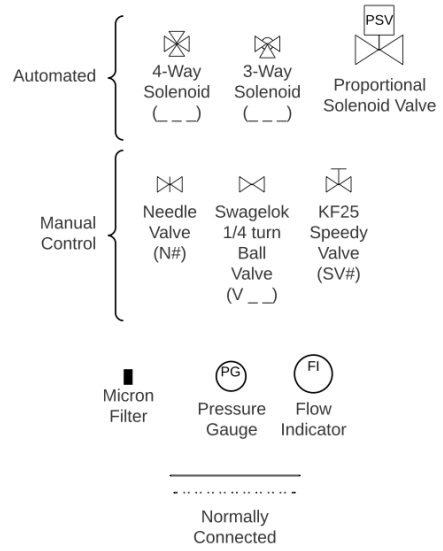

ID	Module	Type	Control
DI	Gas Buffer	Three-way solenoid	Automated
DO	Gas Buffer	Three-way solenoid	Automated
GBI	Gas Buffer	Three-way solenoid	Automated
GBO	Gas Buffer	Three-way solenoid	Automated
MSO	Molecular Sieve	Three-way solenoid	Automated
PSV	Detector I/O	Proportional solenoid	Automated
FWU	Molecular Sieve	Four-way solenoid	Automated
FWL	Molecular Sieve	Four-way solenoid	Automated
SV1	Detector I/O	KF25 Speedy Valve	Manual
SV2	Detector I/O	KF25 Speedy Valve	Manual
SV3	Detector I/O	KF25 Speedy Valve	Manual
SV4	Detector I/O	KF25 Speedy Valve	Manual
SV5	Detector I/O	KF25 Speedy Valve	Manual
SV6	Detector I/O	KF25 Speedy Valve	Manual
VDI	Molecular Sieve	Swagelok 1/4 turn	Manual
VDO	Molecular Sieve	Swagelok 1/4 turn	Manual
VGF	Molecular Sieve	Swagelok 1/4 turn	Manual
VVG	Molecular Sieve	Swagelok 1/4 turn	Manual
VMSL1	Molecular Sieve	Swagelok 1/4 turn	Manual
VMSL2	Molecular Sieve	Swagelok 1/4 turn	Manual
VMSR1	Molecular Sieve	Swagelok 1/4 turn	Manual
VMSR2	Molecular Sieve	Swagelok 1/4 turn	Manual
N1	Gas Buffer	Needle	Manual
N2	Gas Buffer	Needle	Manual
N3	Gas Buffer	Needle	Manual
N4	Gas Buffer	Needle	Manual
N5	Molecular Sieve	Needle	Manual
N6	Molecular Sieve	Needle	Manual

Figure 6.10 Detailed schematic with key of the gas system and 100 L detector vessel.

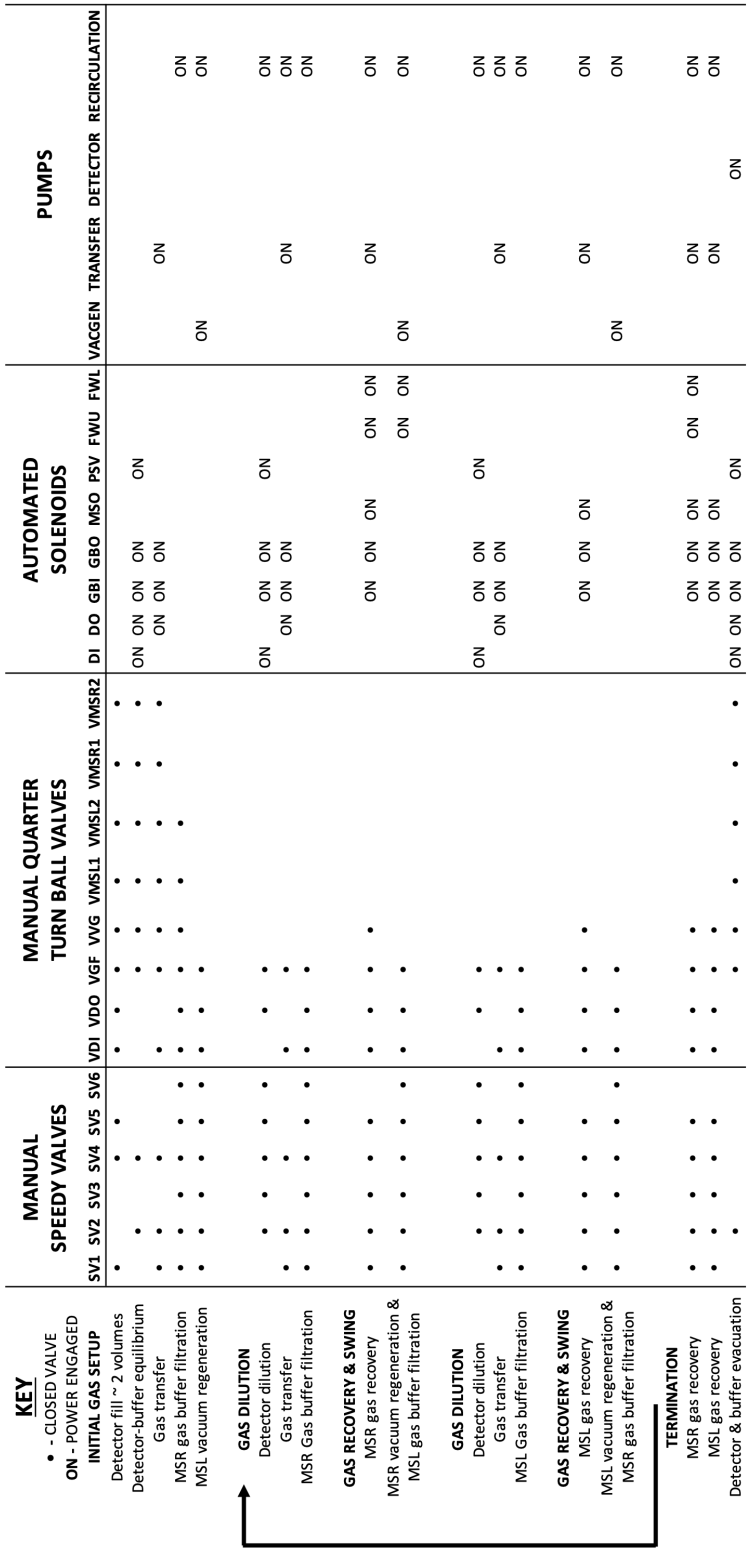

Figure 6.11 Step by step method of has system operation with the status of valves detailed. The arrow corresponds to the cyclic path during continuous operation. (Key: • = closed valve, ON = power engaged).

The initial setup started with the gas system and vacuum vessel evacuated down to pressures of 0.6 and 0.3 torr, respectively. The evacuation was done for 48 hours to ensure the bulk of material outgassing was complete. The test detector vessel was filled with 105.2 torr of SF_6 gas, calculated using Equation 6.1. The gas in the detector volume was transferred to the buffer cylinder until the P_{det} was reached. The detector pressure achieved was 50.2 torr, resulting in 1.17×10^3 torr (1.6 atmospheres) in the buffer cylinder. The MS filter-right was connected to the buffer cylinder with the recirculation pump flowing at a rate of 5 LPM. The MS filter-left was connected to the vacuum regeneration pump and continuously maintained a vacuum of less than 5 torr.

After 24 hours, the gas in the test detector vessel was diluted with the cleaner filtered buffer gas and was left for 5 minutes to mix. The gas in the vacuum vessel was transferred back to the buffer cylinder until the test detector vessel pressure returned to pre-dilution pressure, 49.9 torr. Before the MS filter swing, the gas inside the MS filter-right was recovered and fed to the gas buffer. The critical regeneration pressure of the MS is in $\mathcal{O}$(10 torr). Therefore, the MS filter-right was only evacuated to a pressure $\sim$ 100 torr. There was a minimal amount to recover since the MS filters were packed to capacity, with the evacuation completed in seconds. The swing was completed by connecting the MS filter-right to the vacuum regeneration pump and the MS filter-left to the gas buffer.

The gas dilution, gas recovery, and MS filter swing cycle was repeated for a total of 4 cycles, with the observed pressures shown in Table 6.2. Note that fluctuations in the detector vessel and buffer cylinder pressure can be attributed to changes in environmental conditions. Once the gas system operation was completed, the gas inside the MS filters was recovered to the buffer cylinder. The gas in the vacuum vessel and buffer cylinder was evacuated and disposed of appropriately.

	Pressure after swing (torr)			
	Vacuum Vessel	**Buffer Cylinder** $\times10^3$	**MS Right**	**MS Left**
INITIAL	50.2	1.17	1.17×10^3	<5
SWING-I	49.9	1.17	<5	1.17×10^3
SWING-II	50.6	1.17	1.17×10^3	<5
SWING-III	50.4	1.18	<5	1.18×10^3
SWING-IV	50.7	1.18	1.18×10^3	<5

Table 6.2 Observed pressures immediately after swing (Demo run II, March 2022). The vacuum vessel used a CERAVAC capacitance manometer gauge with an error of ±0.05 torr. Whereas the buffer and MS used a 4-20mA piezoelectric gauge with an error of ±5 Torr.

The engineering test has successfully demonstrated the method of operation outlined in subsection 6.3.1, with 50 torr of SF_6 in a test vessel of 100 L. Four total cycles of the gas dilution, gas recovery, and MS filter swing processes were completed. Although it was observed that P_{det} was fluctuating between swings, it's assumed that the amount of gas inside the test vessel did not change, and the pressure fluctuations were due to changes in environmental conditions. Since the gas system can control P_{det} after each swing, the amount of gas in the detector can be kept constant by returning the test vessel pressure to the observed pre-dilution pressure. Therefore, it can be assumed that stable operation with a gas TPC detector is possible.

The swing process required roughly 15 minutes, in practice, this would correspond to the detector being offline for 1% of the total operation time. However, since the gas system operation was performed manually, automation of the system could significantly reduce this. A solution that would lead to the test vessel never going offline is calibrating the flow between the gas buffer and the test vessel so that the operating detector pressure is regulated. However, this presents additional engineering challenges and can reduce the time available for gas filtration. Nonetheless, the engineering test demonstrated that the MS-based VSA gas recycling system can be applied to a gas TPC detector for full operation testing.

6.4 Conclusions

In this chapter, a gas system designed to effectively implement the MS filters with SF_6 gas-based directional dark matter detectors, was discussed. The gas system utilises a Vacuum Swing Adsorption (VSA) technique with a gas recovery buffer. The VSA technique allows the continued use of the MS filters by regenerating them on-site. The gas buffer allows the collection of the small gas volume in the MS filters, which is lost in conventional VSA during vacuum regeneration. A further benefit of employing a gas buffer is that fewer components are directly exposed to the detector volume, thereby reducing the number of potential radon sources.

A gas system prototype suitable for operation with a 100 L gas TPC detector at 50 torr was constructed. This detector configuration was chosen because the concept of the gas system design will be tested using such a detector, which is the subject of Chapter 7. Before the gas system is applied to a fully operational detector, an engineering test was conducted to demonstrate the VSA method and operation at the desired detector configuration. The VSA method was successfully demonstrated for four complete cycles with a 100 L test detector vessel containing 50 torr of SF_6.

Chapter 7

Application of an MS-based gas recycling system to a ThGEM-based TPC detector

This chapter describes the implementation of the gas system prototype to a ThGEM-based TPC detector aimed to demonstrate (i) the reduction of intrinsic radon contamination in the detector setup and (ii) the preservation of the detector's gain amplification capabilities due to the removal of common pollutants.

In order to assess the performance of the gas system tests were performed using ThGEM-based TPC detector both with and without the recirculation system in place. Details of the ThGEM-based TPC detector and the gas system prototype are discussed in Section 7.1. Testing of intrinsic radon contamination reduction is described in Section 7.2, and testing the conservation of the detector's gain amplification capabilities is described in Section 7.3.

7.1 ThGEM-based TPC detector with gas system setup

The detector used in the performance test is a ThGEM-based gas TPC, based on previous work by A. Scarff [178], and the gas system prototype used is described in Chapter 6. Details about the detector, gas system and method of operation are discussed here.

7.1.1 Description of the apparatus

Figure 7.1 shows the experimental setup used to assess the performance of the gas system. There are three main components of the setup, the ThGEM-based gas TPC detector, electronics & DAQ, and the gas system prototype. The detector used in the setup is a gas time projection chamber with Thick Gas Electron Multiplier (ThGEM) readout. The operating principle of gas TPCs and different readout types, were discussed in Chapter 1. A ThGEM

readout was employed because it has been utilised in a large number of gain studies in the past [76, 77, 179]. *Gain* is a measure of the detector's amplification capabilities, and is the parameter tested in Section 7.3, to demonstrate the gas system is removing gain-harming common pollutants.

For the performance tests, continuous long-term detector operation is required, so the ThGEM and TPC configuration chosen was based on previous work which has demonstrated stable operation [58, 178]. The ThGEM used was 10 x 10 cm with a thickness of 0.4 mm, a hole pitch of 0.4 mm and a hole diameter of 0.4 mm, as shown at the top of Figure 7.1. The ThGEM detector was mounted 2 cm from a square cathode to create a time projection chamber. To achieve the electric field required to drift and amplify electrons, high-voltage power supplies were connected to the cathode and top of the ThGEM, and the bottom of the ThGEM was grounded, as shown by the dashed lines in Figure 7.1. The high voltage power supplies used were Bertran model 377P for the positive supply and Bertran model 377N for the negative supply. The signal was read out from the top of the ThGEM via Ortec 142 IH preamplifier, which was placed inside the vessel to reduce the distance from the ThGEM in a bid to limit signal noise. The output of the preamplifier was connected to an Ortec 572 shaping amplifier and signals were recorded with an Ortec 926 ADCAM MCB in the form of a pulse height spectrum on a computer. The parameter *gain* is calculated from the pulse height spectrum, detailed later in Section 7.3. To provide a standard source of ionisation in the TPC, an ^{55}Fe source producing 5.89 keV x-rays was mounted on a magnet and directed at the sensitive detector volume, as shown right of the 100 L vessel. The magnet allowed the source to be redirected for source-off measurements.

Although the sensitive detector volume is only 0.2 L, the detector used was enclosed in a 100 L vessel in order to demonstrate that the gas system is capable of operating with large volumes. With the exception of the DRIFT directional dark matter detector, the majority of directional dark matter gas TPCs are less than 50 L. The gas system prototype, shown on the right of Figure 7.1, consists of a 4.5 L gas buffer and two MS filter columns with a capacity of up to 500 g and was connected to opposing arms of the vacuum vessel to optimise gas flow. The gas system utilises a modified Vacuum Swing Adsorption (VSA) technique with a gas recovery buffer, full details of the prototype are in Section 6.2.

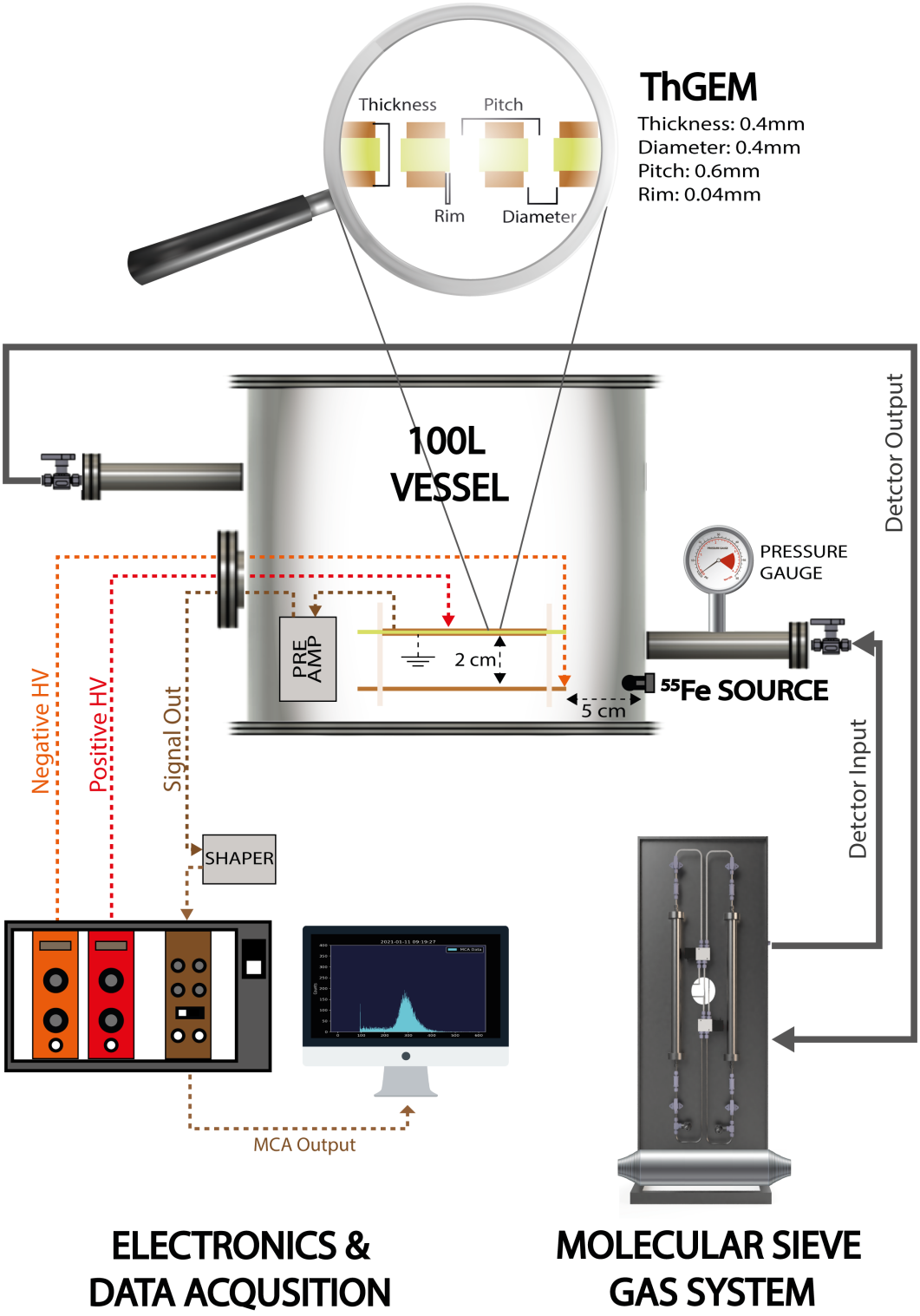

Figure 7.1 Schematic of the experimental setup used in the gas system performance testing with a ThGEM-based TPC detector.

7.1.2 Gas system and TPC operation

To understand how the gas system operates with the ThGEM-based TPC detector, it is important to recognise that there are two separate volumes during operation. Figure 7.2 depicts these two volumes, where the volume within the gas system and the TPC are represented by the green and orange shaded areas, respectively. Here the TPC volume does not refer to the sensitive volume but the total volume of the vessel. The volume inside the TPC is used for detector operation, while the volume inside the gas system is filtered by the MS filter on the right. Note that the MS filter on the left is simultaneously undergoing regeneration by vacuum.

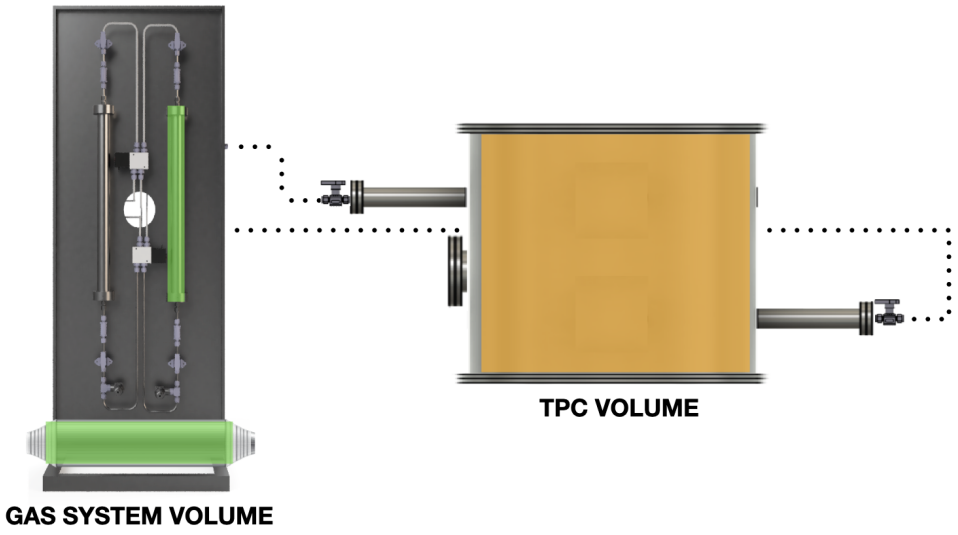

Figure 7.2 Simplified graphic of the gas system prototype connected to a detector vessel, highlighting two separate volumes during operation. Gas system volume in green and TPC volume in orange.

Most of the time, operation of the gas system with the TPC detector is the state described in Figure 7.2. However, after a certain period, intrinsic detector contamination will introduce radon and common pollutants into the TPC volume. To combat this, the filtered gas from the gas system is introduced into the TPC, effectively diluting and purifying the detector gas. As the TPC detector operates at high voltages, it is preferable to go over the detector pressure during gas replacement to prevent electric discharges. Therefore, the process of gas replacement involves dilution of the TPC volume to two times the operating detector pressure. After a mixing period, the operating detector pressure is restored by transferring the additional gas back to the buffer. Following gas dilution, the MS filters swing from filtration

mode to vacuum regeneration mode and vice versa. For detailed information on gas system operation, including gas recovery refer to subsection 6.1.3

Figure 7.3 shows a simplified gas operation timeline. The TPC detector is operational the majority of the time while one MS filter continuously filters the gas buffer and the other MS filter undergoes vacuum regeneration. The gas dilution and swing process is set to repeat every t_{swg}, with the required frequency depending on the contamination rate of the TPC. In the engineering test described in Section 6.3, t_{swg} was set to 24 hours to allow for an effective daily replacement of the detector volume. The gas dilution and swing procedure lasted approximately 15 minutes.

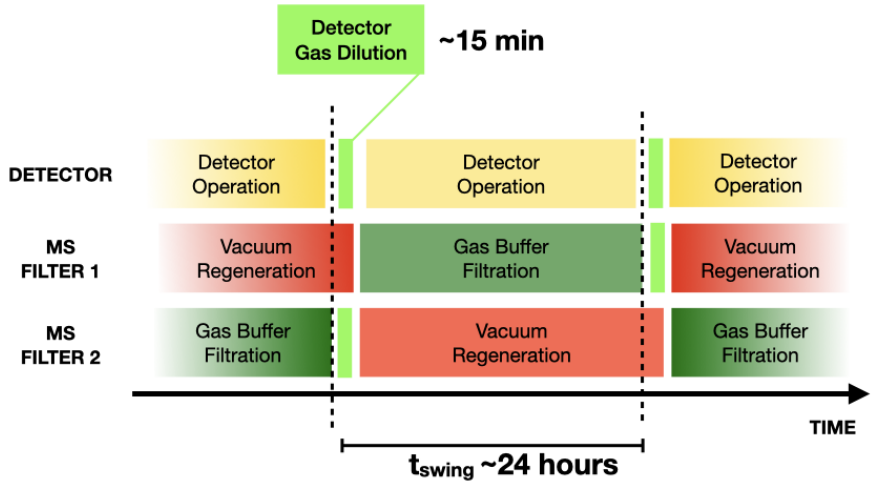

Figure 7.3 A simplified timeline for the gas system operation with TPC detector. The value of t_{swing} was set to 24 hours to allow for an effective daily replacement of the detector volume. The gas dilution and swing procedure lasted approximately 15 minutes, during which the detector was offline. A more detailed timeline can be seen in Figure 6.4.

7.2 Radon activity reduction test

Intrinsic radon emanation from detector materials can provide a source of unwanted backgrounds, as described in Section 2.2. This section covers the work undertaken to assess the performance of the gas system prototype in reducing the intrinsic radon background of the gas TPC detector setup. The assessment was conducted by measuring the intrinsic radon background of the gas TPC detector setup with and without the gas system operating. The MS used was the low radioactive candidate 5Å type NU-MS V2, examination of this MS is detailed Chapter 5. A model of radon dynamics between the gas system and gas TPC detector setup was considered to determine the effective radon reduction during long-term detector operation.

7.2.1 Radon dynamics during gas system operation

To evaluate the effective radon reduction due to the application of the gas system, it is important to understand the radon dynamics between the gas system and the gas TPC detector. The radon activity in the experimental set up is determined by the balance between emanation of radon from materials and radon absorption in the MS filter. This is best qualified by first considering the two volumes involved, the volume in the ThGEM-based TPC detector, detonated by V_{TPC} and the gas system volume, denoted by V_{GS}. The two volumes can be considered separate until the gas dilution and swing process is triggred.

The radon activity from material emanation in these volumes increases until a steady state between the rate of radon emanation and radon decay is achieved, termed secular equilibrium activity. The growth of the radon activity due to materials in the ThGEM-based TPC detector volume and gas system is shown in Equation 7.1 and Equation 7.2, respectively.

$$A^{ema}_{TPC}(t_{ema}) = A^{sec}_{TPC} - (A^{sec}_{TPC} - A_{TPC}(t_{ema} = 0)exp(-\lambda_{Rn}t_{ema}), \tag{7.1}$$

$$A^{ema}_{GS}(t_{ema}) = A^{sec}_{GS} - (A^{sec}_{GS} - A_{GS}(t_{ema} = 0))exp(-\lambda_{Rn}t_{ema}), \tag{7.2}$$

here A^{ema} is the radon activity due to emanation, t_{ema} is the emanation time, $A^{ema}(t_{ema} = 0)$ is the initial radon activity at zero emanation time, and λ_{Rn} is radon's decay constant. The subscripts TPC and GS correspond to the origin of radon emanation, for instance, A^{ema}_{GS} is the radon activity from material emanation in the gas system volume.

The kinematics of radon adsorption during MS filtration is expected to be a product of incident molecular flux of adsorbent species and sticking probability [180]. The number of

radon captured by MSs, N_{MS}, in filtration time t_{filt} is given by

$$N_{MS} = FSt_{filt}, \tag{7.3}$$

where F is the incident molecular flux, and S is the sticking probability. The incident molecular flux is defined by the Hertz-Knudsen equation [181],

$$F = \frac{P}{\sqrt{2\pi mkT}}, \tag{7.4}$$

where P is the gas pressure, T is temperature, m is the mass of one molecule, and k is the Boltzmann constant. This equation, however, assumes that all gas molecules are adsorbent species. In the case of radon adsorption only, if it is assumed that the temperature and flow rate in the gas system are constant, the incident flux can be approximated to be proportional to the total number or radon atoms present,

$$F \propto N_{tot}, \tag{7.5}$$

where N_{tot} is the total number of radon atoms present in the gas system. The sticking probably is given by

$$S = f(\theta)exp(-E_a/RT), \tag{7.6}$$

here $f(\theta)$ is a function related to the surface coverage of adsorbed species on the MSs, E_a is the activation energy barrier for adsorption, and R is the gas constant. Since the MSs are regularly vacuum regenerated it can be assumed that there are always vacant sites, also if the same MS geometry is used the number of available sites stay the same. Therefore, a reasonable first approximation is that the radon sticking probability, S is constant when operating with the gas system as $f(\theta)$ is expected to remain relatively unchanged. Using the assumptions discussed above, Equation 7.3 can be estimated to be given by

$$N_{MS} \approx N_{tot}k_{ms}t_{filt}, \tag{7.7}$$

where k_{ms} is a constant associated with the sticking probability for a fixed MS geometry and parameters related with the incident molecular flux, such as pressure, flow rate, and temperature, which are assumed to remain constant during gas system operation. The number of radon atoms captured can be converted to activity by using $N = A/\lambda_{Rn}$, where λ_{Rn} is the radon decay constant, resulting in

$$A_{MS} \approx A_{tot}k_{ms}t_{filt}, \tag{7.8}$$

here A_{MS} is the activity reduction due to radon captured and A_{tot} is the radon total activity in the gas system. Recall that the parameter t_{swg} is the time set between the gas dilution and swing process. Therefore, for every swing cycle, the gas system volume and TPC volume remain separate for a duration of t_{swg}. During this time, the radon activity in the TPC volume, A_{TPC}, and gas system volume A_{GS} can be described by Equation 7.9 and Equation 7.10, respectively.

$$A_{TPC} = A_{TPC}^{ema}(t_{swg}), \tag{7.9}$$

$$A_{GS} = A_{TPC}^{ema}(t_{swg}) - A_{MS}(N_{tot}, t_{swg}). \tag{7.10}$$

The radon activity in the TPC volume is expected to increase due to material emanation from the detector setup, while the radon activity in the gas system is expected to decrease assuming that the rate of radon filtration is greater than the rate of material emanation from the gas system.

After time t_{swg}, the dilution and swing process is initiated, the gas system and TPC volumes are mixed. Despite the different sizes of the two volumes, there are approximately equal amounts of gas in each volume due to the pressure differences. Consequently, the resulting activity after the swing process for both volumes is approximately half of the combined activity from the gas system and TPC. Since gas system operation will involve many swings, the radon activity in the ThGEM-based TPC volume after n cycles is given by

$$A_{V_{TPC}}(n) = \frac{1}{2}\sum_{n}\left(A_{TPC}^{ema}(t_{swg}) + A_{GS}^{ema}(t_{swg}) - A_{MS}(N_{tot}, t_{swg})\right). \tag{7.11}$$

A model of the radon dynamics in the TPC with MS filtration and without MS filtration is plotted in Figure 7.4, the model uses Equation 7.11, where secular activity parameters were set to unity, and the time between the swing process, t_{swg}, was set to 24 hours. This value was selected for t_{swg} because it corresponds to a daily replacement of one detector volume. For the case with MS filtration, the filtration constant k_{ms} was extrapolated from the radon filtration measurements described in Chapter 5. It was found that the extrapolated k_{ms} for the examined MSs were $\sim 2 \times 10^{-5}\mathrm{s}^{-1}$, except for the MS with large granule geometry which was $0.5 \times 10^{-5}\mathrm{s}^{-1}$. This can be explained by the poor surface to volume ratio of the large granule, resulting in fewer vacant sites available and a smaller sticking probability. For the model with MS filtration a value of k_{ms} of $2 \times 10^{-5}\mathrm{s}^{-1}$ was used. For the case without MS filtration, k_{ms} was set to zero. In both cases, it was assumed that the initial radon activity in the TPC and gas system was zero, as the operation begins with an extended evacuation of the setup.

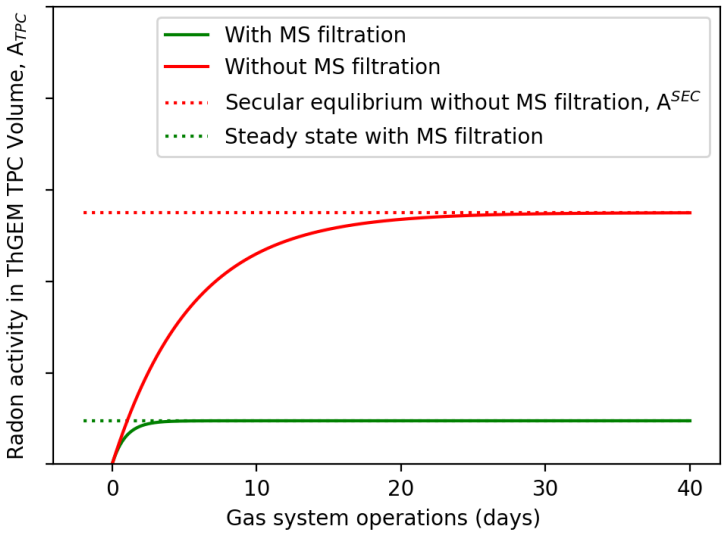

Figure 7.4 Model of radon dynamics in the TPC volume over 40 days operation, with and without MS filtration. Derived using Equation 7.11.

The radon activity behaviour in the TPC volume with MS filtration is described as follows: initially, the radon activity in the TPC increases due to material emanation. As the radon concentration grows, the increased radon flux in the MS filter will result in more radon captured. The rate of material emanation slows down as it approaches secular equilibrium. A steady state is reached when the radon filtration rate is equal to the radon emanation rate. The model suggests that steady-state activity is reached within days. For comparison, the radon activity without MS filtration grows to the secular equilibrium activity with a timescale of a month, as expected. To evaluate the effective radon reduction due to the application of the gas system, the two values that must be calculated is the radon at activity secular equilibrium without MS filtration and steady state with MS filtration.

7.2.2 Experimental setup and method

To evaluate the effective radon reduction caused by the application of the gas system, two values must be measured: the radon activity at secular equilibrium without MS filtration and the steady state radon activity with MS filtration, as predicted by the radon dynamics model. The radon activity at secular equilibrium corresponds to the maximum radon activity during detector operation due to intrinsic material emanation, while the radon dynamics model steady state activity provides the suppressed radon activity during detector operation, as a result of gas system filtration.

The experimental method for measuring radon activities consisted of gas system prototype operation with the ThGEM-based TPC detector for four days, followed by a 12 hour radon measurement. Four days of gas system operation were selected because the radon dynamics model predicted that this was sufficient time to achieve steady-state activity between intrinsic material emanation and radon filtration.

The gas system prototype operation with the TPC detector follows the steps outlined in subsection 6.3.1. The TPC detector operated at 50 torr SF_6, and the time between the swing and dilution process, t_{swg}, was set to 24 hours. This value was selected for t_{swg} because it corresponds to a daily replacement of one detector volume. For the radon activity measurement with MS filtration, 40g of low radioactive MS type 5Å (NU MS V2) were used in each filter, and for the run without MS filtration the MS filters were left blank.

After four days of gas system prototype operation, a DURRIDGE RAD7 radon detector was used to measure the radon activity in the TPC detector volume. As the RAD7 is only rated to operate at atmospheric pressure, it was not possible to directly measure the TPC detector volume, which was at a pressure of 50 torr. Instead, the 100L TPC volume's gas was evacuated into a 4.5L sample cylinder and pressurised to atmospheric pressure.

Figure 7.5 shows the experimental setup used to measure radon activity in the sample cylinder. Two RAD7 radon detectors were connected in a loop with the sample cylinder, and pumps inside the RAD7 were used to recirculate the gas during the 12 hour measurements. Note that before the RAD7 were connected in a loop, they were purged with low-humidity SF_6.

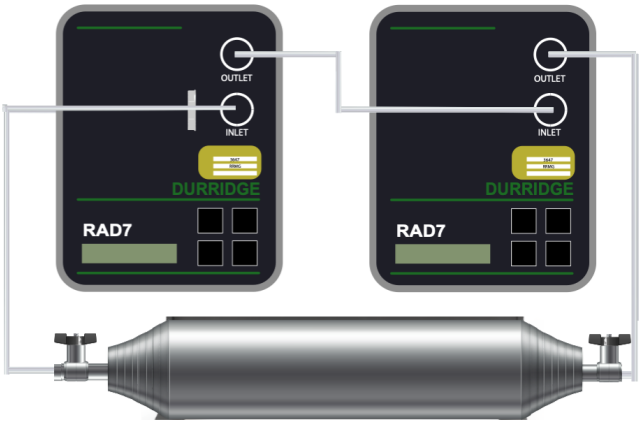

Figure 7.5 Experimental setup used for radon activity measurements by method of sampling.

7.2.3 Data analysis

The DURRIDGE RAD7 is not calibrated to measure in carrier gas SF_6, therefore a calibration factor must be applied to account for changes in the collection efficiency due to the carrier gas SF_6. To account for this, it was determined that the output of a DURRIDGE calibrated RAD7 must be multiplied by 3.33. Details for the determination of calibration factors are in Chapter 3. The RAD7 output is also multiplied by the total volume of the two RAD7s and sampling cylinder (6.4 L) in order to convert radon concentration output (Bq/m^3) to radon activity (Bq).

Since radon measurements were taken using a sampling technique, corrections are required for the radon in the sample that has decayed during measurement and the radon contribution of the sampling apparatus. At the point of sampling, the source of radon is effectively *turned off* and will start to decay. Here the radon source is the intrinsic radon emanation of materials in the gas system and TPC setup. To account for the radon decay during the 12 hour measurement,

$$A(t_{sam}) = A_0 exp(-\lambda_{Rn} t_{sam}), \tag{7.12}$$

is fitted to the RAD7 radon activity data. Here, $A(t_{sam})$ is the radon activity at time since sampling, A_0 is the radon activity at the point of sampling, and λ_{Rn} is radon decay constant. The radon activity at the point of sampling A_0 is extrapolated from the Equation 7.12 fitted to the RAD7 radon activity data.

At the point of sampling, a new radon source is also introduced from the material emanation of the measurement apparatus. In order to account for this, background subtraction is applied to the extrapolated radon activity A_0. The background activity was calculated by conducting a blank 12 hour test using the measurement apparatus in Figure 7.5. The blank SF_6 measurement resulted in an activity contribution of 14.0±5.7 mBq.

A further correction is necessary for measurement without MS filtration because, at the time of sampling, it has not reached secular equilibrium. To compensate for the shorter emanation time,

$$A(t_{ema}) = A^{sec} \times ((1 - exp(-\lambda_{Rn} t_{ema})), \tag{7.13}$$

is applied. Here $A(t_{ema})$ is the activity resulting in an emanation time t_{ema}, and A^{sec} is the activity at secular equilibrium. The emanation time in the measurements conducted is equivalent to the total time of gas system operation with the gas TPC, four days.

7.2.4 Radon activity results and discussion

Table 7.1 shows the extrapolated values for the radon activity at secular equilibrium without MS filtration, and the steady state radon activity with MS filtration predicted by the radon dynamics model. The results show a clear reduction in the intrinsic radon activity in the TPC volume due to the application of the gas system containing low radioactive MS type 5Å (NU MS V2).

Measurement Run	**Extrapolated Steady State Activity (mBq)**
Without MS filtration	43.3±14.3
With MS filtration	0.8±6.4

Table 7.1 Summary of radon activity results.

The result for the measurement run without MS filtration is 43.3±14.4 mBq, which corresponds to the maximum radon activity during detector operation due to intrinsic material emanation from both the 100 L ThGEM-based TPC detector and the gas system prototype. The application of MS filtration with the low radioactive MS in the gas system prototype, resulted in suppressing the radon activity to 0.8±6.4 mBq.

The large error can be attributed to the measurement apparatus's background limits. The MS filtration result before the background subtraction was 14.8±2.8 mBq, which is within errors of the background activity, 14.0±5.7 mBq. The radon activity has been reduced within the measurement apparatus limits. For a conservative calculation of the total activity reduction, the upper limit of the MS filtration result was used. The gas system prototype utilising NU MS V2 has reduced the intrinsic radon activity in the ThGEM-based TPC detector setup to less than 7.2 mBq, which corresponds to a reduction of at least 83%.

7.3 Gas gain conservation test

The presence of O_2, N_2 and H_2O, termed common pollutants, in a gas TPC suppresses the detector's *gain*, as described in Section 2.3. Gain is the parameter used to measure the amplifications capabilities of a gas TPC detector. This section describes the work conducted to evaluate the performance of the gas system prototype in conserving gain in a ThGEM-based TPC detector, as a result of removing common pollutants. The performance of the gas system was tested by first observing the deterioration of gain due to intrinsic contamination from common pollutants, followed by a second identical detector run with the gas system operating. The MSs used were the 3Å, and 4Å types, which are known to capture common pollutants, and were demonstrated not to absorb SF_6, in Chapter 5.

To effectively demonstrate gain deterioration, a large initial gain is desired. Therefore, it was decided that the target gas CF_4 is used as an analogue for SF_6 since this target gas can achieve superior gain compared to SF_6. Although they are different targets, these two gases are chemically identical to 3Å and 4Å type MSs, as both of them are not adsorbed.

7.3.1 Experimental setup and method

To evaluate the performance of the gas system prototype in conserving gain due to the removal of common pollutants, it is necessary to have an experimental setup that monitors gain and is only affected by common pollutants. The signal gain of a detector is dependent on many parameters, namely the purity of the gas, amount of the gas and the avalanche electric field [178, 182]. There are also temporary gain effects, such as charge-up, which alter the effective gain at the start of detector operation [183]. In order to observe the effect of only the common pollutants on gain, it is important to keep all these parameters constant and account for temporary effects.

The experimental setup previously detailed in Section 7.1, is configured so that the ThGEM-based TPC detector's gain can be monitored as a function of common pollutants. During detector operation, the vessel pressure and high voltage supplied to the detector can be continuously logged to ensure that the amount of gas and the avalanche electric field are kept constant, respectively. Since the charge-up effect only occurs during the first few minutes of operation, if gain measurements are performed over the timescale of days, it can be ignored.

To monitor gain in the ThGEM-based TPC detector, a constant source of ionisation is required to provide the signal. An ^{55}Fe calibration source producing 5.89 keV x-rays was used to generate electron-ion pairs in CF_4 in the TPC detector volume. To drift and amplify the electrons, high voltages in the ThGEM-based TPC were configured to settings known

to provide a stable signal gain in 50 torr CF_4 [58, 178]. High voltages of -855 V and 604 V were applied to the cathode and top of the ThGEM, respectively. The bottom of the ThGEM was grounded to the vacuum vessel. The amplified charges were detected and recorded using the electronics and DAQ described in Section 7.1. The recorded signals from the detector are in the form of a pulse height spectrum, which is used to calculate gain.

To assess the performance of the gas system, the ThGEM-based TPC detector was operated for one week without the gas system to demonstrate the gain deterioration due to intrinsic detector contamination from common pollutants. This was followed by an identical detector run but with the gas system operating. For both runs, the gain was monitored by measuring the ^{55}Fe calibration source energy spectrum for a 5 minutes exposure every half hour.

For the detector run with the gas system, the method of operation follows the steps outlined in subsection 6.3.1. The time between the gas system's swing and dilution process, t_{swg}, was set to 24 hours. This value was selected for t_{swg} because it corresponds to a daily replacement of one detector volume. Since the rate of contamination from common pollutants is expected to be greater than the rate of radon emanation, the amount of MSs used was maximised. A total of 500g of 3Å and 4Å Sigma-Aldrich MSs in equal ratios were used for each filter.

7.3.2 Data analysis

The output signals from the ThGEM-based TPC detector are recorded using an analogue to digital converter multichannel analyser in the form of a pulse height spectra. The analyser units are in ADC channels which can be calibrated to gain. In gas TPC operation there are signal gain contributions from electronics gain, due to signal amplification from preamplifier and shaper electronics, and gas gain, due to additional charge generated in the detector gas during the electron avalanche process. Since the investigation is concerning gas purity, the output of the analyser must be calibrated to gas gain.

The total signal gain is defined as the ratio of the measured charge from the detector setup, N_{det}, and expected charge from interaction produced ionisation, N_{ion}, given by

$$GAIN = \frac{N_{det}}{N_{ion}}. \tag{7.14}$$

The expected charge from interaction produced ionisation, N_{ion}, is defined by

$$N_{ion} = \frac{E_{Fe}}{W}, \tag{7.15}$$

where E_{Fe} is the energy of the ^{55}Fe calibration source and W is the average energy required to create an electron-ion pair for a given gas. The interaction produced electrons are drifted in the TPC and amplified by the electric field in the ThGEM, the output signal from the ThGEM is solely from gas gain contribution, but further signal amplification is achieved by the detector electronics. The measured charge from the detector setup including the electronics, N_{det}, is defined by

$$N_{det} = \frac{VC}{e}, \tag{7.16}$$

where V is the voltage signal from ThGEM signal output, C is the capacitance of the preamplifier and e is the electron charge.

The detector response can be calibrated to correspond to gas gain by simulating the ThGEM signal output with known test pulses. The corresponding gas gain for a given test pulse, V_{pulse} can be calculate using

$$GAIN = \frac{V_{pulse}C}{e}\frac{W}{E_{Fe}}. \tag{7.17}$$

Test pulses, V_{pulse}, between 200 and 1600 mV were used to calibrate the detector's response, N_{det}, with gas gain. The test pulse voltage height was configured using a Tennelec TC 814 pulser. The detector response was measured using an analogue to digital converter multichannel analyser, Ortec 926 ADCAM.

The gas gain was calculated using Equation 7.17 and the constants in Table 7.2. The calibration results are shown in Table 7.3. A least fit regression between gas gain and the detector's response is plotted in Figure 7.6, resulting in a calibration Equation 7.18.

Constant	**Value**	**Units**
C	1.0	pF
E_{Fe}	5.8	keV
W_{CF_4} [184]	35	eV
e	1.6×10^{-19}	C

Table 7.2 Constants used for gain calibration.

Test Pulse,V_{pulse} (mV)	**Measured Charge, N_{det}, (ADC)**	**Gas Gain ($\times 10^4$)**
200	104	0.72
400	203	1.44
600	303	2.16
800	400	2.89
1000	516	3.61
1200	610	4.33
1400	703	5.05
1600	811	5.77

Table 7.3 Test pulse values used for calibrating detectors gas gain.

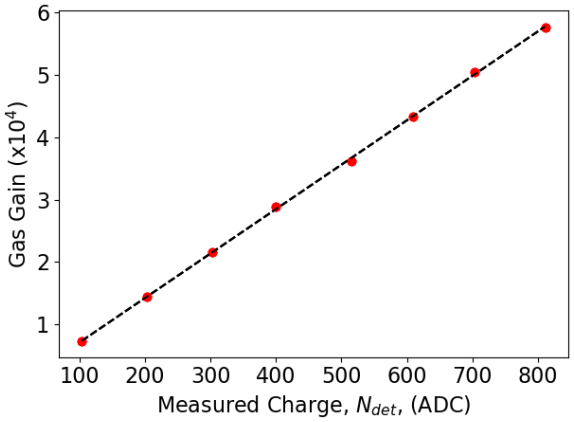

Figure 7.6 Plot of gas gain against ADC detector output.

$$GG = 71.4 \times N_{det} - 105. \tag{7.18}$$

In practice, the pulse height spectrum obtained from the ^{55}Fe calibration source is not as defined as the test pulses in gain calibration. The ThGEM-based TPC detector outputs individual pulses related to the charge generated by ^{55}Fe calibration source interactions with CF_4 gas. Although a mono-energetic source was used, there will be variation in pulse heights due to the inherent response of the detector [185]. A measurement of the ^{55}Fe calibration source is shown in Figure 7.7. The plot shows the number of counts for a given pulse height during a five minute ^{55}Fe calibration source exposure. To calculate the detector response, N_{det}, a Gaussian is fitted to the ^{55}Fe photo peak signal in the pulse height spectra (red line), and the mean is determined, μ (white line). The gas gain is calculated by using Equation 7.18, where the detector response, N_{det}, is equal to the Gaussian mean, μ.

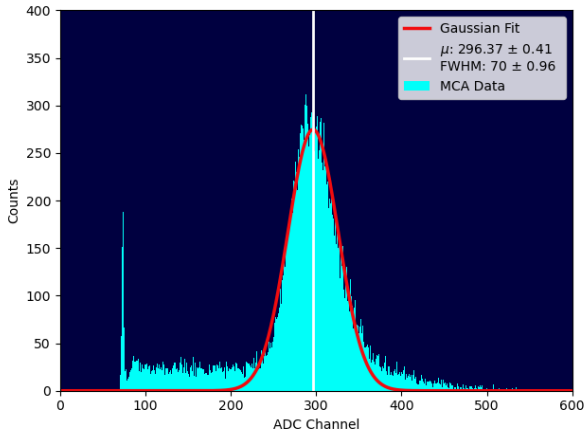

Figure 7.7 Gaussian fit to ^{55}Fe calibration source pulse height spectrum peak.

To determine gas gain over time, the gaussian analysis was applied to each measurement during the week long detector run. Note in the pulse height spectra, a decreasing gas gain corresponds to the ^{55}Fe photo peak signal shifting towards lower ADC channels, an example is shown in Figure 7.8. There is a period the ^{55}Fe photo peak signal starts leaking into the ADC threshold. The Gaussian analysis is no longer applicable from this point and is defined as when the signal is lost to the background.

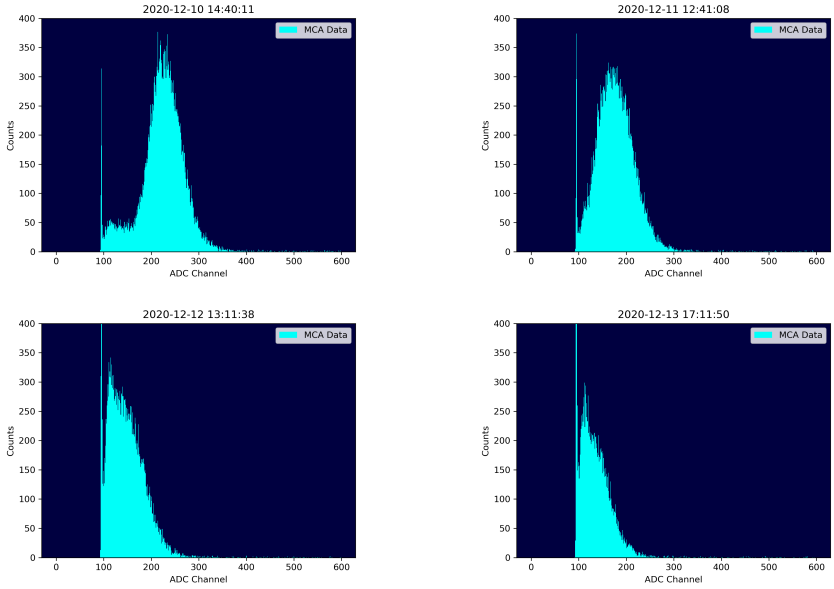

Figure 7.8 Example of ^{55}Fe photopeak shifting towards background over time. Plot sequentially follows top left, top right, bottom left, then bottom right.

7.3.3 Gas gain measurement results

Before analysing the data from the week long measurement runs, it is important to verify that other gain-affecting parameters were constant throughout. Figure 7.9 shows plots of detector pressure and high voltages applied to the ThGEM TPC, for both measurement runs. The average values and 2σ deviation are shown in Table 7.4. Standard deviation in detector pressure and high voltages are within the instrumentation uncertainty of the logger. Consequently, any variations in detector gas gain during measurement runs can be attributed to the presence of common pollutants.

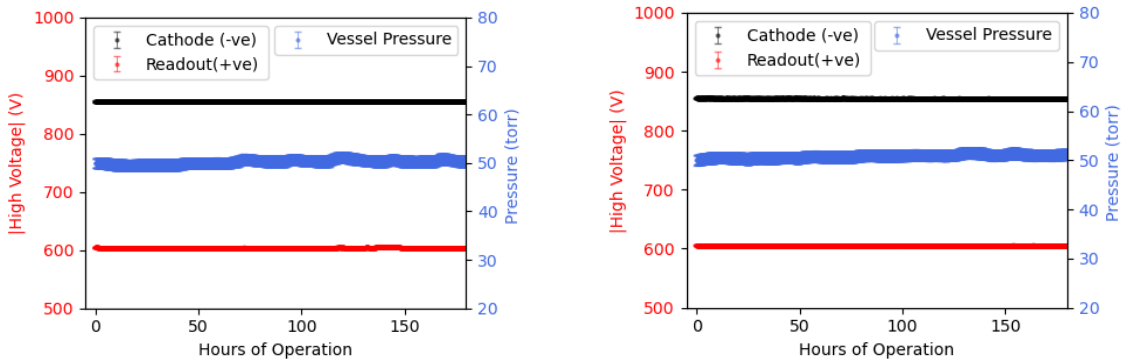

Figure 7.9 Plot of detector pressure and applied high voltages in the ThGEM TPC during measurement runs. No gas replacement run (left) and gas system operation run (right).

Measurement Run	Average Detector Pressure (Torr)	Average ThGEM HV (V)	Average Cathode HV (V)
Without Gas System	50.2 ± 0.8	604 ± 0.8	855 ± 0.3
With Gas System	50.9 ± 0.7	604 ± 0.1	855 ± 0.6

Table 7.4 Average values of detector pressure and applied high voltages over the measurements runs. Errors shown are 2σ deviation.

Gain measurement without the gas system

Figure 7.10 shows the ThGEM-based TPC's gas gain over time without gas replacement. Measurements were made for the full week. However, the gas gain could not be calculated from the pulse height spectrum after 120 hours as the ^{55}Fe photo peak started to leak into the ADC threshold background. Therefore, the signal is defined as lost at 120 hours, as indicated by the grey vertical line. There is a clear deterioration of the gas gain over the week-long measurement, with a quarter of the initial measured gas gain lost after 54 hours since gas

fill. The non-linear decrease in gas gain has been attributed to contaminants capturing both primary and avalanche electrons [182].

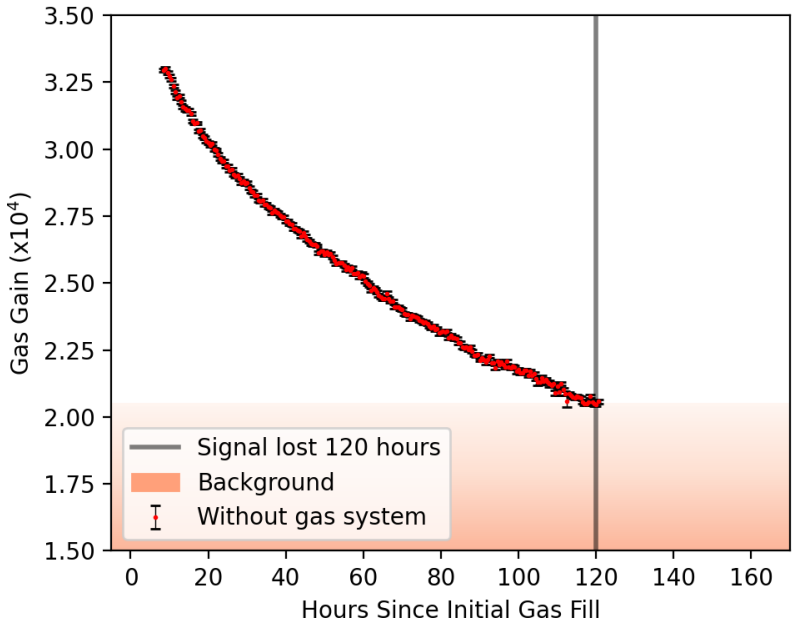

Figure 7.10 Plot of gas gain against time elapsed since initial gas fill for measurement run without gas replacement.

Gain measurement with the gas system

Figure 7.11 shows gain measurements with the gas system prototype operating. The gas gain remained well above the background throughout the week of measurements. In the previous run without the gas system, the signal was lost to the background at 120 hours, as indicated by the grey vertical line. For comparison with the gas system operating, at 120 hours the gas gain was still 87% of the highest measured gas gain.

During gas system operation two separate equal volumes are used, one in the TPC and one in the gas system, previously described in Section 7.1. Before the first gas dilution in the swing cycle, the volume in the TPC has effectively been operating without the gas system, thus the rate of gain deterioration is comparable to that in previous run. At the point of gas dilution, the gas system volume would have been filtering for a t_{swing} duration. If the full TPC volume was replaced, the gas gain is expected to return to the starting level. However, the gas replacement process is achieved by dilution, where the gas system volume is mixed with the TPC volume, suggesting imperfect gas replacement.

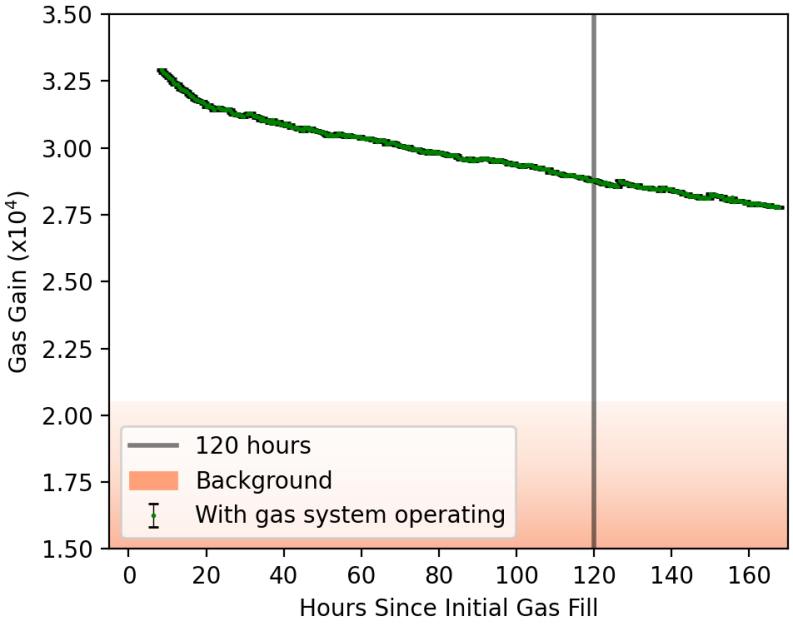

Figure 7.11 Plot of gas gain against time for measurement run with gas system operation. Scales are kept consistent with Figure 7.10

The first dilution, resulted in a significant change in the rate of gain deterioration, demonstrating the gas dilution process has removed gain-harming common pollutants from the TPC volume. Continued gas system operation appears to maintain the slowing of gain deterioration. However, since the gas gain is still deteriorating, the rate of intrinsic contamination is greater than the filtration rate of the gas system. This suggests the absolute amount of common pollutants in the detector volume will continue to increase with the total time elapsed since the initial gas fill, until a critical contamination is reached and the signal is lost.

At the same time, as the concentration of impurities increases, there will be more available species to adsorb, potentially resulting in an improved rate of filtration. This implies that there may be a steady state gas gain where the contamination removed by the gas system is equal to the intrinsic contamination introduced between swing cycles. Similar to the steady state radon activity predicted by the radon dynamic model in Section 7.2 To investigate how the rate of gain deterioration develops with gas system operation, the gain measurement run was extended for another week.

Extended gas system operation

Gain measurements with the gas system operating for another week are shown in Figure 7.12. The gas gain signal remained above the background until detector operation was stopped at

340 hours. The periodic discontinuity in gas gain corresponds to the gas dilution every 24 hours during the swing cycle. The detector pressure and high voltage monitors stayed within the observed deviation during the first week of measurements.

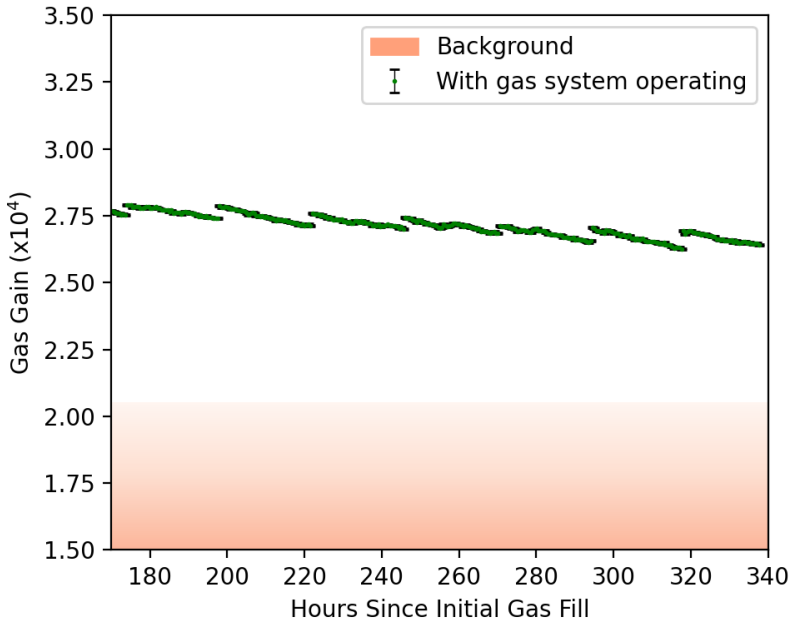

Figure 7.12 Plot of gas gain against time for extended measurement run with gas system operation Scales are kept consistent with Figure 7.10.

To determine if gas system filtration and intrinsic contamination is approaching a steady state, the effective gain change, ΔG, after each swing cycle was calculated. The effective gain change is defined by

$$\Delta G = G_R - G_L, \tag{7.19}$$

where G_R is the gain recovered, calculated from the magnitude of the discontinuity after gas dilution. G_L is gain lost, calculated from the difference between the starting and end gas gain during a swing cycle. A steady state gain is reached when the effective gain change is zero. A plot of the effective gain change against swing cycles is shown in Figure 7.13. The magnitude of effective gain change appears to decrease per cycle. The last cycle results in ΔG within errors of the steady state gain condition, $\Delta G = 0$. This suggests that it may be possible to achieve an equilibrium between the gain recovery by the gas system and the gain lost due to intrinsic contamination. However, more data is needed to conclusively determine whether this equilibrium has been attained. Figure 7.14 shows the last swing cycle gain measurements. Gas gain during this period ranged from 2.69 - 2.63 $\times 10^4$, highlighted by

the green band. In can be seen during the last 48 hours of operation gas gain measurements stayed within this band.

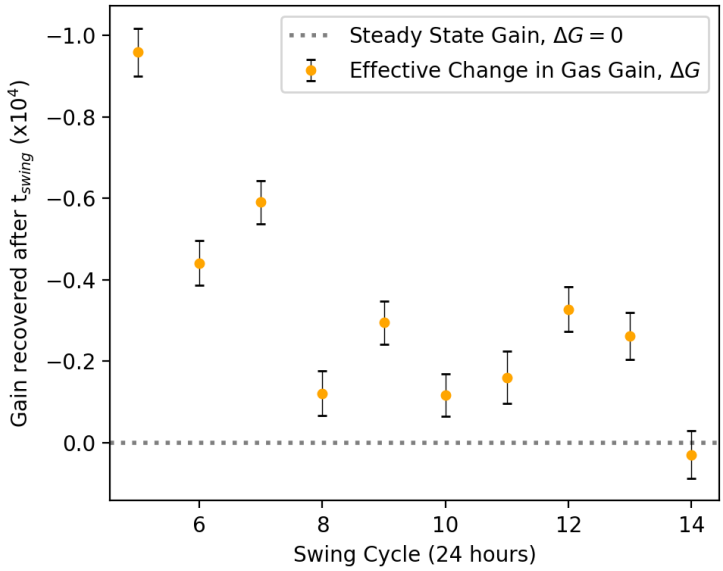

Figure 7.13 Plot of effective gain ΔG, against swing cycle. Note that y-axis is inverted.

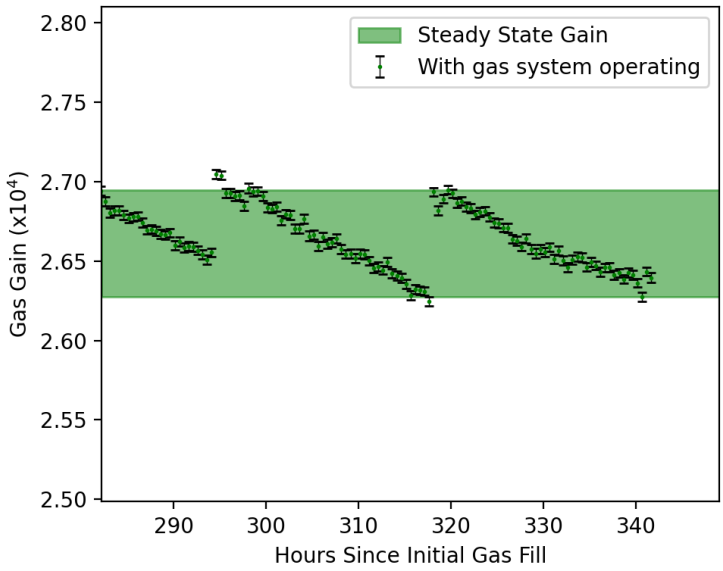

Figure 7.14 Magnified plot of gas gain against time during the last two swing cycles in the measurement run with gas system operation.

7.3.4 Gas gain measurement discussion

To provide a fair comparison between the measurement runs, both the gas gain levels maintained and the amount of gas used must be considered. A summary of the measurement runs results with gas gain levels at notable points is shown in Table 7.5. The gas gain percentage is compared to the highest gain level measured in detector setup, 3.3 $\times 10^4$. Gas used corresponds to the total amount of gas used during operation in units of the TPC volume.

Measurement Run	**Gas Used (TPC vol.)**	**Gas Gain (%)**			**Signal notes**
		50h	**120 h**	**340h**	
Without Gas System	1	80%	62%	-	lost after 120 hours
With Gas System	2	92%	87%	80%	remained until termination

Table 7.5 Summary of the measurement runs results with gas gain levels at notable points.

In the run without gas replacement, the signal was lost to the background after 120 hours, whereas with the gas system operating, the signal remained above the background until detector operation was stopped at 340 hours. The argument can be made that the gas system, requiring two TPC volumes during operation, used double the amount of gas, and if the same amount of gas were used in the measurement without the gas system the run would extend to 240 hours. However, the maintained levels of gas gain must also be taken into account.

In the measurement run with the gas system, the gas gain remained above 2.63 $\times 10^4$, or 80% of the highest gain achieved in the setup, for 340 hours. In comparison, without the gas system, the gas gain only remained above this level for 50 hours. Assuming the same gain deterioration rates, to remain above a gas gain of 80% without the gas system for 340 hours, the detector volume must be replaced seven times. This amount equates to a factor of 3.5 more gas required, compared to gas system operation.

The gas gain remained above the background level until the measurement run was terminated, indicating the possibility of operation past 340 hours. Furthermore, during the last swing cycle, the amount of gain recovered and gain lost were within errors, suggesting a steady state gain is attainable. The last two swing cycle was equivalent to 81±1% of the highest gain measured in achieved in the setup setup.

7.4 Conclusions

This chapter described the tests performed to evaluate the concept of a MS-based vacuum swing adsorption gas system design. A prototype gas system was applied to a ThGEM-based TPC detector to assess the gas system's ability to reduce intrinsic radon contamination from the detector setup and maintain detector gain by removing gain-harming common pollutants. It was shown that the gas system prototype coupled with the low radioactive MS type 5Å (NU MS V2) reduced the intrinsic radon activity in the ThGEM-based TPC detector setup within error of the radon measurement apparatus background (14.0±5.7 mBq). Using the upper limits of radon measurement, it was determined that radon activity had been reduced to less than 7.2 mBq, which corresponds to the removal of at least 83% of the total intrinsic radon activity of the setup. In addition, it was demonstrated that utilising MS types 3Å and 4Å with the gas system significantly reduced the effects of gain deterioration due to common pollutants. In a detector run with the gas system operating, the signal remained until detector operation was terminated after 340 hours. Without the gas system, the TPC detector could only maintain this level of signal amplification for 50 hours. Furthermore, an extended detector run with the gas system suggests that a steady state gain, where the rate of introduction of common pollutants is equal to the rate of filtration, is attainable. However, the implicated steady state gain is only 80% compared to the gain with *fresh gas*. This can be improved in two ways: by increasing the rate of filtration in the gas system or by decreasing the contamination from common pollutants in the detector setup. Similarly, by reducing intrinsic radon contamination and optimising the rate of filtration, the radon activity in the detector setup can be reduced further, but a radon measurement apparatus with a lower background is required first. Although it is evident that MS filtration occurred during gas system operation, it is unknown whether MS breakthrough occurred during t_{swg}. If breakthrough was achieved, decreasing t_{swg} could also improve the rate of filtration.

The results presented in this chapter suggest that a vacuum swing adsorption gas recycling system coupled with suitable MSs can reduce intrinsic radon activity and extend detector operation in an SF_6 gas-based directional dark matter detector. Further work is required to optimise the operation of the gas system. The filtration rate can be improved by operating at lower temperatures, higher pressures, or higher flow rates, while the intrinsic radon contamination can be reduced by constructing the gas system with radio-pure material.

Chapter 8

Conclusions

The evidence presented in Chapter 1 indicates that only $\sim$15% of the mass in the universe is known, with the unknown portion composed of non-baryonic dark matter. The favoured dark matter candidates are the Weakly Interacting Massive Particles (WIMP), and there are many experiments searching for WIMP dark matter by direct detection of rare baryon-WIMP interactions. An ultimate discovery limit for direct detection experiments arises from the solar neutrino background. Directional dark matter detectors provide a method to overcome this background by adding information about the direction of the WIMP-induced recoil events. Most directional detectors reconstruct recoil tracks using low-pressure gas Time Projection Chambers (TPC). SF_6 has become an ideal target gas for gas-based directional dark matter searches, as it enables negative ion drift, target gas fiducialisation and has a high fluorine content for spin-dependant (SD) searches.

In Chapter 2, the effects of radon contamination in dark matter experiments and the impact of common pollutants (O_2, H_2O and N_2) on gas TPCs were explored. Radon contamination is a source of unwanted background that can mimic genuine WIMP-induced signals, whereas the presence of common pollutants can significantly suppress the signal amplification capabilities of a gas TPC detector. Current methods to deal with radon contamination and common pollutants were discussed. A major focus of this thesis was not only to investigate the removal of radon from SF_6, but also the possibility of a system that can simultaneously address the problem of common pollutants.

To study radon in SF_6 gas, an accurately calibrated radon detector was required. In Chapter 3, the effects of different carrier gases in electrostatic radon collection were explored, and the collection efficiency for a commercial electrostatic radon detector (DURRIDGE RAD7) was experimentally determined in SF_6 and other gases relevant to the CYGNUS directional dark matter collaboration (He and CF_4). A new Monte Carlo simulation of the complex chemical and physical processes around radon detection in the RAD7 was developed

in order to predict collection efficiencies in other carrier gases. It was found that modelling the chemical neutralisation of small ion recombination requires further work.

In the work described in Chapter 4, radon removal from SF_6 using four types of commercially available molecular sieves (MSs) was examined. The removal of radon from SF_6 was demonstrated for the first time with a 5Å type MS. Radon concentration from contaminated SF_6 gas was reduced to $\sim$87% of the initial radon concentration using the 5Å type MS with dry ice in a cold trap. The MS types 3Å and 4Å are known to capture common pollutants, and it was shown that they do not absorb SF_6. This suggested a gas system employing MS types 3Å, 4Å and 5Å can possibly remove both common pollutants and radon from SF_6 simultaneously. Unfortunately, commercial MSs intrinsically emanate radon at levels unsuitable for ultra-sensitive rare-event physics experiments.

Chapter 5 covers work undertaken to investigate low radioactive 5Å type MS alternatives by calculating a parameter indicating the amount of radon intrinsically emanated by the MS per unit of radon captured from SF_6 gas. A low radioactive MS candidate developed by Nihon University in collaboration with Union Showa K.K. (NU MS V2) was found to emanate at least 98.9% less radon per radon captured, compared to the commercial MS used in Chapter 4.

A gas system designed to effectively implement the MS filters with SF_6 gas-based directional dark matter detectors, was presented in Chapter 6. The gas system design uses the Vacuum Swing Adsorption (VSA) technique with a gas recovery buffer. The VSA technique allows the continued use of the MS filters by regenerating them on site. The gas buffer allows the collection of the small gas volume in the MS filters, which is lost in conventional VSA during vacuum regeneration. Although the gas system was designed for use with SF_6, it is possible to be used for other target gas mixtures such as CF_4 and He, if appropriate MSs are employed. A gas system prototype was constructed to assess the concept of the MS-based VSA design with a ThGEM-based gas TPC detector in a 100L vacuum vessel operating at a pressure of 50 torr.

Two performance tests were conducted to evaluate the capabilities of the gas system prototype, as described in Chapter 7. The reduction of intrinsic radon contamination in the detector setup as a result of radon removal with a 5Å type MS and conservation of the detector's gain amplification capabilities due to the removal of common pollutants with 3Å and 4Å type MSs was investigated. It was found that with the gas system prototype using low radioactive MS type 5Å (NU MS V2), the intrinsic radon activity in the detector setup was reduced within error of the radon measurement apparatus background (14.0±5.7 mBq). It was also demonstrated that the gas system run with 3Å and 4Å type MSs significantly reduced the effects of gain deterioration due to common pollutants, with the signal gain

remaining until detector operation was terminated after 340 hours. In comparison, the TPC detector could only maintain this level of signal amplification for 50 hours without the gas system. Moreover, an extended detector run with the gas system suggests that a steady-state gain is attainable where the rate of introduction of common pollutants is equal to the rate of filtration.

The results presented in this thesis demonstrate the feasibility of an MS-based VSA gas system that simultaneously removes radon and common pollutants from SF_6-based directional dark matter detectors. Further R&D is required to optimise the MS filtration rate in the gas system, which could be accomplished by operating at lower temperatures, higher pressures or faster flow rates. Gas system operation with larger detector volumes should be investigated by configuring the current prototype's gas buffer and MS filter sizes and selecting an appropriate recirculation pump. During construction, greater emphasis should be placed on the selection of radio-pure components in order to reduce the intrinsic radon contamination of the gas system. To reduce the amount of time the detector is offline during gas system operation, the gas dilution swing cycle should be automated. Alternatively, if the flow from the gas buffer to the detector volume is regulated and replacement is calibrated with a mass flow controller, the detector will remain online at all times. Efforts towards large-scale production of low radioactive Nihon University-developed 3Å, 4Å, and 5Å type MSs are needed, as only $\mathcal{O}$(1 kg) has been synthesised. The study presented in this thesis could be repeated with other target gases to explore the applicability of the MS-based gas system with other gas-based experiments.[1] Another approach to this study is the use of Metal Organic Frameworks (MOFs) instead of MSs. MOFs have the advantage over MSs as they can be synthesised to a wider range of pore sizes, compared to the 4 possible sizes of MSs. A pore size exactly matching radon can provide better selectivity resulting in less absorbent material required in the gas system. Also, the superior selectivity can facilitate radon removal from similar-sized atoms like xenon. Since the starting materials for the synthesis of MOFs are organic, it may be possible to create radon-absorbing materials with even lower radioactivity.

[1]The author was consulted regarding the viability of radon removal from TREX-DM TPC target gas consisting of a Ne-2%isobutane mixture. A test with 5Å type was recommended, and it was found to capture radon [186].

References

[1] F. Zwicky, "The redshift of extragalactic nebulae", Helvetica Physica Acta **6**, 110–127 (1933).

[2] F. Zwicky, "On the masses of nebulae and of clusters of nebulae", The Astrophysical Journal **86**, 217 (1937).

[3] R Fusco-Femiano and J. P. Hughes, "Nonpolytropic model for the coma cluster", The Astrophysical Journal **429**, 545–553 (1994).

[4] R. Carlberg, H. Yee, and E Ellingson, "The average mass and light profiles of galaxy clusters", The Astrophysical Journal **478**, 462 (1997).

[5] V. C. Rubin and W. K. Ford Jr, "Rotation of the andromeda nebula from a spectroscopic survey of emission regions", The Astrophysical Journal **159**, 379 (1970).

[6] M. A. W. Verheijen, "The ursa major cluster of galaxies. v. h i rotation curve shapes and the tully-fisher relations", The Astrophysical Journal **563**, 694–715 (2001).

[7] Y. Sofue, "Rotation curve and mass distribution in the galactic center–from black hole to entire galaxy–", Publications of the Astronomical Society of Japan **65**, 118 (2013).

[8] L. Chemin, C. Carignan, and T. Foster, "H i kinematics and dynamics of messier 31", The Astrophysical Journal **705**, 1395–1415 (2009).

[9] T. Treu, "Strong lensing by galaxies", Annual Review of Astronomy and Astrophysics **48**, 87–125 (2010).

[10] D. M. Wittman et al., "Detection of weak gravitational lensing distortions of distant galaxies by cosmic dark matter at large scales", nature **405**, 143–148 (2000).

[11] D. Clowe, A. Gonzalez, and M. Markevitch, "Weak-lensing mass reconstruction of the interacting cluster 1e 0657–558: direct evidence for the existence of dark matter", The Astrophysical Journal **604**, 596 (2004).

[12] NASA, *Chandra photo album 1e 0657-56*, (2006) https://chandra.harvard.edu/photo/2006/1e0657/ (visited on 11/24/2022).

[13] J. C. Mather et al., "Measurement of the cosmic microwave background spectrum by the cobe firas instrument", The Astrophysical Journal **420**, 439–444 (1994).

[14] N. Aghanim et al., "Planck 2018 results-v. cmb power spectra and likelihoods", Astronomy & Astrophysics **641**, A5 (2020).

[15] N. Aghanim et al., "Planck 2018 results-vi. cosmological parameters", Astronomy & Astrophysics **641**, A6 (2020).

[16] C. Patrignani et al., "Review of particle physics", Physical Review D **86** (2012).

[17] J. Beringer et al., "Review of particle physics", Physical Review D-Particles, Fields, Gravitation and Cosmology **86**, 010001 (2012).

[18] B. D. Fields, "The primordial lithium problem", Annual Review of Nuclear and Particle Science **61**, 47–68 (2011).

[19] S. Dodelson, E. I. Gates, and M. S. Turner, "Cold dark matter", Science **274**, 69–75 (1996).

[20] G. Bertone, *Particle dark matter: observations, models and searches* (Cambridge University Press, 2010).

[21] S. Dodelson and L. M. Widrow, "Sterile neutrinos as dark matter", Physical Review Letters **72**, 17 (1994).

[22] V. Barinov et al., "Results from the baksan experiment on sterile transitions (best)", Physical Review Letters **128**, 232501 (2022).

[23] P Abratenko et al., "First constraints on light sterile neutrino oscillations from combined appearance and disappearance searches with the microboone detector", arXiv preprint arXiv:2210.10216 (2022).

[24] R Acciarri et al., "A proposal for a three detector short-baseline neutrino oscillation program in the fermilab booster neutrino beam", arXiv preprint arXiv:1503.01520 (2015).

[25] R. D. Peccei and H. R. Quinn, "Constraints imposed by cp conservation in the presence of pseudoparticles", Physical Review D **16**, 1791 (1977).

[26] P. Sikivie, "Experimental tests of the" invisible" axion", Physical Review Letters **51**, 1415 (1983).

[27] C Bartram et al., "Search for invisible axion dark matter in the 3.3–4.2 μ ev mass range", Physical review letters **127**, 261803 (2021).

[28] T. Braine, R Cervantes, N Crisosto, N Du, S Kimes, L. Rosenberg, G Rybka, J Yang, D Bowring, A. Chou, et al., "Extended search for the invisible axion with the axion dark matter experiment", Physical review letters **124**, 101303 (2020).

[29] J. L. Feng, "Dark matter candidates from particle physics and methods of detection", Annual Review of Astronomy and Astrophysics **48**, 495–545 (2010).

[30] S. P. Martin, "A supersymmetry primer", in *Perspectives on supersymmetry ii* (World Scientific, 2010), pages 1–153.

[31] D. Murnane, *The table of particles appearing in the minimal supersymmetric*, (2014) https://www.researchgate.net/figure/The-table-of-particles-appearing-in-the-Minimal-Supersymmetric-Standard-Model_fig10_338924428 (visited on 11/25/2022).

[32] T. Appelquist, H.-C. Cheng, and B. A. Dobrescu, "Bounds on universal extra dimensions", Physical Review D **64**, 035002 (2001).

[33] S. Giagu, "Wimp dark matter searches with the atlas detector at the lhc", Frontiers in Physics **7**, 75 (2019).

[34] A. Boveia and C. Doglioni, "Dark matter searches at colliders", arXiv preprint arXiv:1810.12238 (2018).

[35] M. G. Aartsen et al., "Search for dark matter annihilations in the sun with the 79-string icecube detector", Physical review letters **110**, 131302 (2013).

[36] A. Albert, "Indirect searches for dark matter with the fermi large area telescope", Physics Procedia **61**, 6–12 (2015).

[37] M. Schumann, "Direct detection of wimp dark matter: concepts and status", Journal of Physics G: Nuclear and Particle Physics **46**, 103003 (2019).

[38] J Schmaler et al., "Status of the cresst dark matter search", in Aip conference proceedings, Vol. 1185, 1 (American Institute of Physics, 2009), pages 631–634.

[39] S. Scorza, EDELWEISS Collaboration, et al., "Edelweiss-iii experiment: status and first low wimp mass results", in Journal of physics: conference series, Vol. 718, 4 (IOP Publishing, 2016), page 042053.

[40] CDMS II Collaboration, "Dark matter search results from the cdms ii experiment", Science **327**, 1619–1621 (2010).

[41] UCL HEP Group, *Ucl dark matter*, (2020) https://www.hep.ucl.ac.uk/darkMatter/ (visited on 11/21/2022).

[42] R Bernabei et al., "The dark matter: dama/libra and its perspectives", arXiv preprint arXiv:2110.04734 (2021).

[43] W. Thompson et al., "Current status and projected sensitivity of cosine-100", in Journal of physics: conference series, Vol. 1342, 1 (IOP Publishing, 2020), page 012134.

[44] J Amaré et al., "Anais-112 status: two years results on annual modulation", in Journal of physics: conference series, Vol. 1468, 1 (IOP Publishing, 2020), page 012014.

[45] G Adhikari, N Carlin, J. Choi, S Choi, A. Ezeribe, L. Franca, C Ha, I. Hahn, S. Hollick, E. Jeon, et al., "An induced annual modulation signature in cosine-100 data by dama/libra's analysis method", arXiv preprint arXiv:2208.05158 (2022).

[46] M. G. Boulay, Deap Collaboration, et al., "Deap-3600 dark matter search at snolab", in Journal of physics: conference series, Vol. 375, 1 (IOP Publishing, 2012), page 012027.

[47] E. Aprile et al., "First dark matter search results from the xenon1t experiment", Physical review letters **119**, 181301 (2017).

[48] D. Akerib et al., "The lux-zeplin (lz) experiment", NIM A. **953**, 163047 (2020).

[49] X. Zhou, PandaX Collaboration, et al., "Updates from the pandax-ii experiment", in Journal of physics: conference series, Vol. 1468, 1 (IOP Publishing, 2020), page 012056.

[50] J Aalbers et al., "First dark matter search results from the lux-zeplin (lz) experiment", arXiv preprint arXiv:2207.03764 (2022).

[51] P Agnes et al., "Low-mass dark matter search with the darkside-50 experiment", Physical review letters **121**, 081307 (2018).

[52] J Billard et al., "Implication of neutrino backgrounds on the reach of next generation dark matter direct detection experiments", Physical Review D **89**, 023524 (2014).

[53] D. Akimov et al., "Observation of coherent elastic neutrino-nucleus scattering", Science **357**, 1123–1126 (2017).

[54] J. Billard et al., "Direct detection of dark matter– APPEC committee report", Reports on Progress in Physics (2022).

[55] J. Aalbers et al., "DARWIN: towards the ultimate dark matter detector", Journal of Cosmology and Astroparticle Physics **2016**, 017–017 (2016).

[56] S. E. Vahsen, C. A. O'Hare, and D. Loomba, "Directional recoil detection", arXiv preprint arXiv:2102.04596 (2021).

[57] N. F. Bell, M. J. Dolan, and S. Robles, "Dark matter pollution in the diffuse supernova neutrino background", arXiv preprint arXiv:2205.14123 (2022).

[58] C. Eldridge, "New negative ion time projection chamber technology for directional detection of dark matter, neutrinos and fast neutrons", PhD thesis (University of Sheffield, 2021).

[59] B. Morgan, A. M. Green, and N. J. Spooner, "Directional statistics for realistic weakly interacting massive particle direct detection experiments", Physical Review D **71**, 103507 (2005).

[60] A. Golovatiuk, "Directional dark matter search with the newsdm experiment", in Journal of physics: conference series, Vol. 2156, 1 (IOP Publishing, 2021), page 012044.

[61] A Alexandrov et al., "Directionality preservation of nuclear recoils in an emulsion detector for directional dark matter search", Journal of Cosmology and Astroparticle Physics **2021**, 047 (2021).

[62] E Baracchini et al., "Cygno: a gaseous tpc with optical readout for dark matter directional search", Journal of Instrumentation **15**, C07036 (2020).

[63] S. Vahsen et al., "The directional dark matter detector (d3)", EAS Publications Series **53**, 43–50 (2012).

[64] D Santos et al., "Mimac: a micro-tpc matrix for directional detection of dark matter", in Journal of physics: conference series, Vol. 309, 1 (IOP Publishing, 2011), page 012014.

[65] J. Battat et al., "Low threshold results and limits from the drift directional dark matter detector", Astroparticle Physics **91**, 65–74 (2017).

[66] T. Ikeda et al., "Direction-sensitive dark matter search with the low-background gaseous detector newage-0.3 b"", Progress of Theoretical and Experimental Physics **2021**, 063F01 (2021).

[67] J. Battat et al., "DMTPC: a dark matter detector with directional sensitivity", in Aip conference proceedings, Vol. 1182, 1 (American Institute of Physics, 2009), pages 276–279.

[68] F Mayet et al., "The drift directional dark matter experiments", European Astronomical Society Publications Series **53**, 11–18 (2012).

[69] K. Nakamura et al., "Newage-direction-sensitive dark matter search experiment", Physics Procedia **61**, 737–741 (2015).

[70] S. Vahsen et al., "Cygnus: feasibility of a nuclear recoil observatory with directional sensitivity to dark matter and neutrinos", arXiv preprint arXiv:2008.12587 (2020).

[71] K. Miuchi et al., "Cygnus", in Journal of physics: conference series, Vol. 1468, 1 (IOP Publishing, 2020).

[72] E Baracchini, "Directional dark matter searches", Astronomy **20**, 21 (2022).

[73] D. P. Snowden-Ifft, "Discovery of multiple, ionization-created cs2 anions and a new mode of operation for drift chambers", Review of Scientific Instruments **85**, 013303 (2014).

[74] J. B. Battat et al., "First background-free limit from a directional dark matter experiment: results from a fully fiducialised drift detector", Physics of the Dark Universe **9**, 1–7 (2015).

[75] N. Phan et al., "The novel properties of sf_6 for directional dark matter experiments", Journal of Instrumentation **12**, P02012–P02012 (2017).

[76] E Baracchini et al., "Negative ion time projection chamber operation with sf6 at nearly atmospheric pressure", Journal of Instrumentation **13**, P04022 (2018).

[77] A. Ezeribe et al., "Demonstration of thgem-multiwire hybrid charge readout for directional dark matter searches", NIM A. **987**, 164847 (2021).

[78] P. Purohit and L. Höglund-Isaksson, "Global emissions of fluorinated greenhouse gases 2005–2050 with abatement potentials and costs", Atmospheric Chemistry and Physics **17**, 2795–2816 (2017).

[79] N. C. for Biotechnology Information, *Pubchem element summary for atomicnumber 86, radon*, data retrieved from PubChem, https://pubchem.ncbi.nlm.nih.gov/element/Radon, 2022.

[80] D. Bossus, "Emanating power and specific surface area", Radiation Protection Dosimetry **7**, 73–76 (1984).

[81] M Markkanen and H Arvela, "Radon emanation from soils", Radiation Protection Dosimetry **45**, 269–272 (1992).

[82] H. Simgen, "Radon assay and purification techniques", in Aip conference proceedings, Vol. 1549, 1 (American Institute of Physics, 2013), pages 102–107.

[83] J. M. Samet, "Radon and lung cancer", JNCI: Journal of the National Cancer Institute **81**, 745–758 (1989).

[84] U. H. S. Agency, *Ukradon - what is radon?*, (2022) https://www.ukradon.org/information/whatisradon (visited on 11/26/2022).

[85] J. Appleton, "Radon: sources, health risks, and hazard mapping", Ambio, 85–89 (2007).

[86] P. Sahu et al., "A comprehensive review on sources of radon and factors affecting radon concentration in underground uranium mines", Environmental Earth Sciences **75**, 1–19 (2016).

[87] E. Miller et al., "Constraining radon backgrounds in lz", in Aip conference proceedings, Vol. 1921, 1 (AIP Publishing LLC, 2018), page 050003.

[88] P Kotrappa, J. Dempsey, J. Hickey, et al., "An electret passive environmental 222rn monitor based on ionization measurement", Health physics **54**, 47–56 (1988).

[89] L Tommasino, "Radon monitoring by alpha track detection", International Journal of Radiation Applications and Instrumentation. Part D. Nuclear Tracks and Radiation Measurements **17**, 43–48 (1990).

[90] A. C. George, "Passive, integrated measurement of indoor radon using activated carbon.", Health physics **46**, 867–872 (1984).

[91] G Zuzel and H Simgen, "High sensitivity radon emanation measurements", Applied Radiation and Isotopes **67**, 889–893 (2009).

[92] N. Chott and R. Schnee, "Radon emanation techniques and measurements for lz", arXiv preprint arXiv:2211.11857 (2022).

[93] H. F. Lucas, "Improved low-level alpha-scintillation counter for radon", Review of Scientific Instruments **28**, 680–683 (1957).

[94] PYLON, *Industrial radon detectors pylon electronics-radon*, (2022) https://pylonelectronics-radon.com/detectors/ (visited on 11/26/2022).

[95] M Wojcik and W Wlało, "A high-sensitivity scintillation chamber for radon in gas", NIM A. **345**, 351–355 (1994).

[96] K. Eappen, R. Nair, and Y. Mayya, "Simultaneous measurement of radon and thoron using lucas scintillation cell", Radiation Measurements **43**, 91–97 (2008).

[97] AlphaGUARD, *Alphaguard – radon monitor - bertin technologies*, (2022) https://www.bertin-technologies.com/product/radon-professional-monitoring/radon-alphaguard/ (visited on 11/26/2022).

[98] DURRIDGE, *Rad7 radon detector user manual*, 2017.

[99] P Baltzer, K. Görsten, and A Bäcklin, "A pulse-counting ionization chamber for measuring the radon concentration in air", NIM A. **317**, 357–364 (1992).

[100] C Mitsuda et al., "Development of super-high sensitivity radon detector for the super-kamiokande detector", NIM A. **497**, 414–428 (2003).

[101] X. R. Liu, SuperNEMO Collaboration, et al., "Radon mitigation strategy and results for the supernemo experiment", in Journal of physics: conference series, Vol. 888, 1 (IOP Publishing, 2017), page 012085.

[102] P Novella et al., "Measurement of radon-induced backgrounds in the next double beta decay experiment", Journal of High Energy Physics **2018**, 1–27 (2018).

[103] K. D. Chu and P. K. Hopke, "Neutralization kinetics for polonium-218", Environmental science & technology **22**, 711–717 (1988).

[104] J Brack et al., "Long-term study of backgrounds in the drift-ii directional dark matter experiment", Journal of Instrumentation **9**, P07021 (2014).

[105] D. Akerib et al., "Projected wimp sensitivity of the lux-zeplin dark matter experiment", Physical Review D **101**, 052002 (2020).

[106] G. Pronost, "Radon monitoring in the kamioka mine", in Journal of physics: conference series, Vol. 1468, 1 (IOP Publishing, 2020), page 012254.

[107] A. Kamaha, B. Mount, and R. Schnee, "Supporting capabilities for underground facilities", arXiv preprint arXiv:2209.07588 (2022).

[108] A. Ianni, "Science in underground laboratories and dulia-bio", Frontiers in Physics **9**, 612417 (2021).

[109] D. Baxter et al., "Snowmass2021 cosmic frontier white paper: calibrations and backgrounds for dark matter direct detection", arXiv preprint arXiv:2203.07623 (2022).

[110] R. Bunker et al., "Evaluation and mitigation of trace 210pb contamination on copper surfaces", NIM A. **967**, 163870 (2020).

[111] V. Guiseppe et al., "A review and outlook for the removal of radon-generated po-210 surface contamination", in Aip conference proceedings, Vol. 1921, 1 (AIP Publishing LLC, 2018), page 070003.

[112] G. Zuzel, "Experience of gas purification and radon control in borexino", in Aip conference proceedings, Vol. 1921, 1 (AIP Publishing LLC, 2018), page 050001.

[113] ATEKO, *Ateko radon removal systems*, (2019) https://www.ateko.cz/media/cache/file/53/ATEKO_Radon_Removal_Systems_2019.pdf (visited on 11/26/2022).

[114] G Benato et al., "Radon mitigation during the installation of the cuore 0 $\nu\beta\beta$ decay detector", Journal of Instrumentation **13**, P01010 (2018).

[115] Pérez-Pérez et al., "Radon mitigation applications at the laboratorio subterráneo de canfranc (lsc)", Universe **8**, 112 (2022).

[116] J. Street et al., "Radon mitigation for the supercdms snolab dark matter experiment", in Aip conference proceedings, Vol. 1921, 1 (AIP Publishing LLC, 2018), page 050002.

[117] J. Street et al., "Construction and measurements of an improved vacuum-swing-adsorption radon-mitigation system", (2015).

[118] K Pushkin et al., "Study of radon reduction in gases for rare event search experiments", NIM A. **903**, 267–276 (2018).

[119] M. Pipe, "Limits on spin-dependent wimp-proton cross-sections using the drift-iid directional dark matter detector", PhD thesis (University of Sheffield, 2011).

[120] K. Abe et al., "Radon removal from gaseous xenon with activated charcoal", NIM A. **661**, 50–57 (2012).

[121] E. Aprile et al., "Online 222 rn removal by cryogenic distillation in the xenon100 experiment", The European Physical Journal C **77**, 1–8 (2017).

[122] F. Sauli, "Progress with the gas electron multiplier", NIM A. **522**, 93–98 (2004).

[123] F. Sauli, "GEM: a new concept for electron amplification in gas detectors", NIM A. **386**, 531–534 (1997).

[124] LCTPC Collaboration, *Gas electron multipliers*, (2022) https://www.lctpc.org/e8/e46/e47/ (visited on 11/26/2022).

[125] R Guida, B Mandelli, and M Corbetta, "Effects of gas mixture quality on gem detectors operation", in Journal of physics: conference series, Vol. 1498, 1 (IOP Publishing, 2020), page 012036.

[126] M. Corbetta, R. Guida, and B. Mandelli, "Triple-gem detectors operation under gas recirculation in high-rate radiation environment", NIM A. **984**, 164627 (2020).

[127] M. Capeans, R. Guida, and B. Mandelli, "Strategies for reducing the environmental impact of gaseous detector operation at the cern lhc experiments", NIM A. **845**, 253–256 (2017).

[128] M Capeans et al., "Rpc performances and gas quality in a closed loop gas system for the new purifiers configuration at lhc experiments", Journal of Instrumentation **8**, T08003 (2013).

[129] L Benussi et al., "Study of gas purifiers for the cms rpc detector", NIM A. **661**, S241–S244 (2012).

[130] Altenmüller et al., "Purification efficiency and radon emanation of gas purifiers used with pure and binary gas mixtures for gaseous dark matter detectors", in 2021 ieee nuclear science symposium and medical imaging conference (nss/mic) (IEEE, 2021), pages 1–3.

[131] Y. Chen et al., "A study on the radon removal performance of low background activated carbon", Journal of Instrumentation **17**, P02003 (2022).

[132] Aguilar-Arevalo et al., "Characterization of the background spectrum in damic at snolab", Physical Review D **105**, 062003 (2022).

[133] C. H. Ha et al., "Radon concentration variations at the yangyang underground laboratory", Frontiers in Physics, 1148 (2022).

[134] Cvetković et al., "Soil gas measurements of radon, co2 and hydrocarbon concentrations as indicators of subsurface hydrocarbon accumulation and hydrocarbon seepage", Sustainability **13**, 3840 (2021).

[135] NCBI, *Table 4-3, radioactive properties of 222rn and its short-lived progeny - toxicological profile for radon - ncbi bookshelf*, (2012) https://www.ncbi.nlm.nih.gov/books/NBK158787/table/T23/ (visited on 11/27/2022).

[136] F James et al., "Srim, the stopping and range of ions in matter", Nucl. Instruments Methods Phys. Res. B. **268**, 1818–1823 (2008).

[137] D. W. Breck and D. W. Breck, *Zeolite molecular sieves: structure, chemistry, and use* (John Wiley & Sons, 1973).

[138] O. G. Raabe, "Concerning the interactions that occur between radon decay products and aerosols", Health Physics **17**, 177–185 (1969).

[139] J. Valentine and S. Curran, "Average energy expenditure per ion pair in gases and gas mixtures", Reports on progress in physics **21**, 1 (1958).

[140] W. W. Nazaroff and A. V. Nero, "Radon and its decay products in indoor air", (1988).

[141] P. J. Linstrom and W. G. Mallard, "The NIST chemistry webbook: a chemical data resource on the internet", Journal of Chemical & Engineering Data **46**, 1059–1063 (2001).

[142] J Irlinger et al., "Monte carlo simulation of semiconductor detector response to 222rn and 220rn environments", Journal of environmental radioactivity **158**, 64–70 (2016).

[143] M. Kaschner et al., "Monte carlo simulation of polonium ion collection in electrostatic field for the purpose of radon detector development", Radiation Protection Dosimetry **198**, 791–795 (2022).

[144] D. Seymour, "Monte carlo simulations of polonium drift from radon progeny in an electrostatic counter", (2017).

[145] L. Rinaldi et al., "Study of 222- 220rn measurement systems based on electrostatic collection by using geant4+ comsol simulation", Applied Sciences **12**, 507 (2022).

[146] ANSYS.Inc, *Ansys mechanical*, version v16.1, 2022.

[147] G. Van Rossum and F. L. Drake, *Python 3 reference manual* (CreateSpace, Scotts Valley, CA, 2009).

[148] C. R. Harris et al., "Array programming with NumPy", Nature **585**, 357–362 (2020).

[149] P. Virtanen et al., "SciPy 1.0: Fundamental Algorithms for Scientific Computing in Python", Nature Methods **17**, 261–272 (2020).

[150] R. Gunn, "Diffusion charging of atmospheric droplets by ions, and the resulting combination coefficients", Journal of Atmospheric Sciences **11**, 339–347 (1954).

[151] R. M. Gregorio et al., "Demonstration of radon removal from sf_6 using molecular sieves", Journal of Instrumentation **12**, P09025–P09025 (2017).

[152] J. Battat et al., "Radon in the DRIFT-II directional dark matter TPC: emanation, detection and mitigation", Journal of Instrumentation **9**, P11004–P11004 (2014).

[153] Solomon et al., *Climate change 2007-the physical science basis: working group i contribution to the fourth assessment report of the ipcc*, Vol. 4 (Cambridge University Press, 2007).

[154] Sigma-Adrich, *Molecular sieves-technical information bulletin, al-143 mineral adsorbents, filter agents and drying agents*, technical report (Sigma-Adrich, 2017).

[155] M. Rahm, R. Hoffmann, and N. Ashcroft, "Atomic and ionic radii of elements 1–96", Chemistry–A European Journal **22**, 14625–14632 (2016).

[156] C Beatriz et al., "Covalent radii revisited", Dalton Trans **21**, 2832 (2008).

[157] Islam et al., "Spectroscopic evaluation of the atomic size", The Open Spectroscopy Journal **5** (2011).

[158] L. Chen et al., "Separation of rare gases and chiral molecules by selective binding in porous organic cages", Nature materials **13**, 954–960 (2014).

[159] Sutton et al., "Uranium-238 decay chain data", Science of the total environment **130**, 393–401 (1993).

[160] P. Marin, "Measurement of the half-life of radon with a curie-type ionization chamber", British Journal of Applied Physics **7**, 188 (1956).

[161] F. G. Kerry, *Industrial gas handbook: gas separation and purification* (CRC press, 2007).

[162] M. Capeans, R. Guida, and B. Mandelli, "Strategies for reducing the environmental impact of gaseous detector operation at the CERN LHC experiments", NIM A. **845**, 253–256 (2017).

[163] R. M. Gregorio et al., "Test of low radioactive molecular sieves for radon filtration in sf_6 gas-based rare-event physics experiments", Journal of Instrumentation **16**, P06024 (2021).

[164] K. Nakamura, "Direction-sensitive dark matter search with a gaseous micro time projection chamber", (2014).

[165] European-Commission, *EU legislation to control f-gases*, technical report (2016).

[166] K Abe et al., "Radon removal from gaseous xenon with activated charcoal", NIMA A. **661**, 50–57 (2012).

[167] R. Roque-Malherbe, *Adsorption and diffusion in nanoporous materials* (CRC Press, 2018), page 185.

[168] H Ogawa, K Abe, M Matsukura, and H Mimura, "Development of low radioactive molecular sieves for ultra-low background particle physics experiment", Journal of Instrumentation **15**, P01039 (2020).

[169] H. Ogawa, *Re: 3a ms type*, Private communication, 2021.

[170] S. M. Walas, "Adsorption and ion exchange", in *Chemical process equipment: selection and design* (BH, Butterworth-Heinemann, an imprint of Elsevier, 1995), 495–500.

[171] E. Gabruś et al., "Experimental studies on 3a and 4a zeolite molecular sieves regeneration in TSA process: aliphatic alcohols dewatering–water desorption", Chemical Engineering Journal **259**, 232–242 (2015).

[172] Inmatec-Company, *Service life of the molecular sieve - technical information*, technical report (2022).

[173] R. Schnee et al., "Construction and measurements of a vacuum-swing-adsorption radon-mitigation system", in Aip conference proceedings, Vol. 1549, 1 (American Institute of Physics, 2013), pages 116–119.

[174] P. E. Jahromi, S. Fatemi, and A. Vatani, "Effective design of a vacuum pressure swing adsorption process to recover dilute helium from a natural gas source in a methane-rich mixture with nitrogen", Industrial & Engineering Chemistry Research **57**, 12895–12908 (2018).

[175] M. Arthurs et al., "Performance study of charcoal-based radon reduction systems for ultraclean rare event detectors", Journal of Instrumentation **16**, P07047 (2021).

[176] R. Guida and B. Mandelli, "A portable gas recirculation unit for gaseous detectors", Journal of Instrumentation **12**, T10002–T10002 (2017).

[177] H. Inc, *320/420/m420 series solenoid valves*, 2022.

[178] A. Scarff, "Developments towards a scaled-up one-dimensional directional dark matter detector", PhD thesis (University of Sheffield, 2017).

[179] A. Breskin et al., "A concise review on THGEM detectors", NIM A. **598**, 107–111 (2009).

[180] R. Nix, *Physical & theoretical chemistry* (LibreTexts libraries, 2022) Chap. Kinetics of Adsorption.

[181] K. W. Kolasinski, *Surface science: foundations of catalysis and nanoscience* (John Wiley & Sons, 2012).

[182] R Guida, B Mandelli, and M Corbetta, "Effects of gas mixture quality on GEM detectors operation", Journal of Physics: Conference Series **1498**, 012036 (2020).

[183] P. Hauer et al., "Study of charge-up processes in gas electron multipliers", in Journal of physics: conference series, Vol. 1498, 1 (IOP Publishing, 2020), page 012029.

[184] I Lopes, H Hilmert, and W. Schmidt, "Ionisation of gaseous and liquid sulphur hexafluoride by 60co γ-radiation", Journal of Physics D: Applied Physics **19**, L107 (1986).

[185] G. F. Knoll, *Radiation detection and measurement* (John Wiley & Sons, 2010) Chap. 4.

[186] I. Irastoza, *Re: question about molecular sieves*, Private communication, 2021.